論文 / 著書情報
Article / Book Information

題目(和文)	
Title(English)	Study of all-optical remotely controllable silicon thermo-optic switch
著者(和文)	LIANGZhu
Author(English)	Zhu Liang
出典(和文)	学位:博士(学術), 学位授与機関:東京科学大学, 報告番号:甲第22号, 授与年月日:2024年12月31日, 学位の種別:課程博士, 審査員:庄司 雄哉,植之原 裕行,中川 茂,西山 伸彦,雨宮 智宏,北 智洋
Citation(English)	Degree:Doctor (Academic), Conferring organization: Institute of Science Tokyo, Report number:甲第22号, Conferred date:2024/12/31, Degree Type:Course doctor, Examiner:,,,,,
学位種別(和文)	博士論文
Type(English)	Doctoral Thesis

Study of all-optical remotely controllable silicon thermo-optic switch

by

Zhu Liang

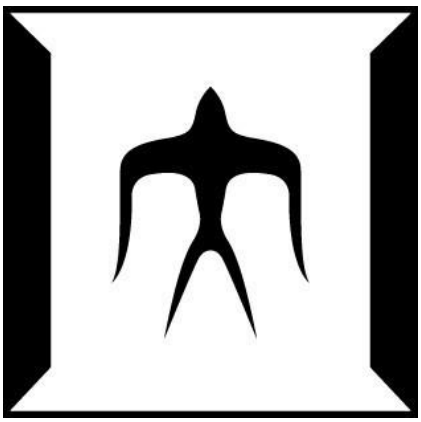

Department of Electrical and Electronic Engineering

School of Engineering

Tokyo Institute of Technology

Doctoral Dissertation

Supervisor: Associate professor Yuya Shoji

December 2024

Contents

CHAPTER 1 ..... **8**

INTRODUCTION **8**

1.1 INTRODUCTION 8

1.2 SILICON PHOTONICS 9

1.2.1 Development of silicon photonics 10

1.2.2 Advantages of silicon photonics integrated optical switches 11

1.3 ALL-OPTICAL THERMO-OPTIC SWITCHES 12

1.3.1 Optical switches 12

1.3.2 All-optical switches 14

1.3.3 Comparison of methods of all-optical thermo-optic switches 15

1.3.3 Application of all-optical thermo-optic switches 18

1.3.3.1 Passive optical network system *18*

1.3.3.2 Remotely controllable passive optical network system *19*

1.3.4 Prospective performance of remotely controllable passive optical network system utilizing all-optical thermo-optic switch 20

1.4 SILICON-BASED INTEGRATED ALL-OPTICAL SWITCHES BASED ON THERMO-OPTIC EFFECT 24

1.4.1 Microring resonators type 24

1.4.2 Mach-Zehnder interferometers type 26

1.5 RESEARCH OBJECTIVE AND DISSERTATION ORGANIZATION 27

1.5.1 Research objective 28

1.5.2 Dissertation organization 28

REFERENCES 30

CHAPTER 2 36

THERMO-OPTIC EFFECT IN SILICON AND LIGHT-TO-HEAT CONVERSION 36

2.1 INTRODUCTION 36

2.2 THERMO-OPTIC EFFECT 36

2.2.1 Thermo-optic effect in silicon 37

2.2.2 Silicon thermo-optic phase shifter and thermo-optic switch 38

2.2.3 Thermo-optic effect with a metal layer compared with non-linear effect 42

2.3 LIGHT-TO-HEAT CONVERSION 46

2.3.1 In the condition of a single waveguide 46

2.3.2 In the condition of two adjacent waveguides 50

2.4 METAL LAYER USED IN THERMO-OPTIC PHASE SHIFTER 54

2.4.1 Thickness and length of titanium layer 54

2.4.2 Distance between titanium layer and silicon waveguide 55

2.4.3 Arrayed patterns of titanium layer 57

2.5 SUMMARY 59

REFERENCES 60

CHAPTER 3 63

REMOTELY CONTROLLABLE MICRORING RESONATOR-BASED THERMO-OPTIC SWITCH 63

3.1 INTRODUCTION 63

3.2 OPERATION PRINCIPLE 64

3.2.1 Microring resonator 64

3.2.2 Microring resonator-based thermo-optic switch 69

3.3 DEVICE DESIGN AND EXPERIMENT 70

3.3.1 Design of microring resonator-based thermo-optic switch 71

3.3.2 Simulation and discussion 76

3.3.3 Fabrication of the designed microring resonator-based thermo-optic switch 77

3.4 PUMP-PROBE MEASUREMENT AND DEVICE CHARACTERIZATION 80

3.4.1 Temporal response measurement 81

3.4.2 Burst switching measurement 83

3.5 SUMMARY 86

REFERENCES 87

CHAPTER 4 89

REMOTELY CONTROLLABLE MACH-ZEHNDER INTERFEROMETER-BASED THERMO-OPTIC SWITCH 89

4.1 INTRODUCTION 89

4.2 OPERATION PRINCIPLE 90

4.2.1 Mach-Zehnder interferometer 90

4.2.2 1×2 Mach-Zehnder interferometer-based all-optical thermo-optic switch .. 93

4.2.3 1×8 Mach-Zehnder interferometer-based all-optical thermo-optic switch .. 94

4.3 DEVICE DESIGN AND EXPERIMENT 97

4.3.1 Design of the 1×2 Mach-Zehnder interferometer-based all-optical thermo-optic switch 97

4.3.1.1 Multimode interferometer couplers *97*

4.3.1.2 Thermo-optic phase shifter (type-A) *101*

4.3.1.3 Thermo-optic phase shifter (type-B) *105*

4.3.2 Design of the 1×8 Mach-Zehnder interferometer-based all-optical thermo-optic switch 112

4.4 EXPERIMENTS AND DEVICE CHARACTERIZATION 113

4.4.1 Fabrication and experimental setup 113

4.4.2 Characterization of the 1×2 Mach-Zehnder interferometer-based all-optical thermo-optic switch 116

4.4.3 Characterization of the 1×8 Mach-Zehnder interferometer-based all-optical thermo-optic switch 120

4.5 DISCUSSION 125
4.6 SUMMARY 127
REFERENCES 128
CHAPTER 5 ..... **130**
CONCLUSION **130**
5.1 CONCLUSION 130
5.2 PERSPECTIVE 132
REFERENCES 137
APPENDIX **139**
A.1 IMPORTANT PARAMETERS IN OPTICAL COMMUNICATION SYSTEMS 139
A.2 DEVICE FABRICATION PROCESS 143
ACKNOWLEDGEMENT **149**
LIST OF PUBLICATION **151**

Chapter 1

Introduction

1.1 Introduction

The invention of the transistor in 1947 by J. Bardeen and W. H. Brattain [1] has been proved to revolutionize the global information age. Replacing vacuum tubes with transistors marked the rapid rise of microelectronics as a crucial pillar in high-tech industries. From the invention of transistors to the emergence of integrated circuits [2] and the fast development of computers, human lives are benefited from these technologies in the past decades. However, as fabrication sizes approach physical limits, it becomes difficult to further increase the integration density and performance of electronic components [3]. Consequently, the trend of "Moore's Law", which has been followed by integrated circuits for decades, is now approaching its limits.

People are seeking ways to solve the above challenge in recent years. Optical communication systems have attracted broad research interests as an effective mean [4]. Traditionally, most information is transmitted using electrons. Electrons have rest mass and are subject to Coulomb interactions, making their motion and electronic signals susceptible to electromagnetic interference. This limitation affects the capacity and speed of electronic communication. In contrast, using photons as information carriers in optical communication systems, has shown advantages in high transmission speed and a large bandwidth [5]. Therefore, photonics integrated circuits (PICs) have been developed rapidly these years and are highly expected for massive future potential in various applications such as communications and even computing.

With the development of PICs, optical switching technology has great potential in

telecommunications networks, data center networks, and interconnect applications for multi-process high-performance computing [6–8]. First, in long-haul telecommunication networks, traditional electronic switches are reaching the bottlenecks with the increase of network throughput and bandwidth while the power consumption of electrical switching is up to 10 K watts which is close to the limit of thermal dissipation [9]. Optical switches have been the prospective components to replace the electronic switches so as to save more energy and reduce delay time. Next, in short-haul data center networks, currently high-speed electrical switches dominate the main applications where frequent network reconfiguration is required based on dynamic workloads. However, these electrical switches using optical/electrical/optical (O/E/O) conversions always require optical converters, which bring additional power consumption to the system. Since all-optical switching does not require O/E/O conversions, it has the potential of lower power consumption and lower cost handling the switching scenarios of long packets or short burst packets. Furthermore, with the appearance of cloud computing, the Internet of Things (IoT), and artificial intelligence (AI), the information switching technology for high-speed and large-capacity data will be widely used in high-performance computers [10]. It has become a challenge for the traditional electrical switches with the limited density of the pin and metal routing while the power consumption also increases dramatically fast. To address these challenges, new microprocessor architectures based on optical switching technologies are expected to significantly improve the bandwidth and latency characteristics of on-chip interconnects [11] Therefore, optical switching technology is a potential solution for signal configuration from long-haul networks to on-chip interconnects.

1.2 Silicon photonics

In recent years, silicon photonics is growing dramatically fast. Benefiting from the compatibility of complementary metal-oxide-semiconductor (CMOS), silicon photonics is leveraging semiconductor manufacturing infrastructure in PICs with complex functionalities [12]. In this section, brief introduction and the development of silicon

photonics over these years will be discussed and then the advantages of silicon photonics integrated optical switches will be described.

1.2.1 Development of silicon photonics

Silicon (Si) has a bandgap energy of 1.12 eV (corresponding to a wavelength of about 1100 nm). Since light with a wavelength larger than this limit cannot be absorbed, silicon is optically transparent in the 1550 nm window of optical communication wavelength. Silicon photonics usually uses Si for the core waveguide and silicon dioxide (SiO_2) for the cladding layers. The refractive index (RI) of Si is ~3.476 and RI of SiO_2 is ~1.444 for the wavelength of 1550 nm at the room temperature. Since the contrast of RI between the core waveguide and cladding layers is very large, a strong light confinement can be achieved. Therefore, compact optical devices with very tight bend radii can be realized using the silicon waveguides.

The first peering work of investigating silicon photonics integrated circuit was reported in 1985 by R. A. Soref et al., who demonstrated epitaxial grown silicon waveguides on doped silicon substrates [13]. In 1987, R. A. Soref et al. reported the free carrier electro-optic effect in silicon by using the undoped-on-doped silicon waveguide structure [14], paving the way for silicon optical modulators, and in 1991, he announced a rib waveguide on silicon-on-insulator (SOI) that enabled single-mode propagation [15]. Later, in 1994, A. G. Rickman demonstrated a low-loss SOI waveguide [16]. Intel Corporation reported a high-speed silicon optical modulator with over 1 GHz modulation frequency based on a metal–oxide–semiconductor (MOS) capacitor on *Nature* in 2004 [17]. S. Manipatruni et al. reported a 40 Gbps modulation rate high speed silicon electro-optic device in 2007 [18]. The more recent reported silicon optical modulator performed beyond 100 Gbps [19].

Today, many optical components such as photodetectors, optical modulators, wavelength division multiplexing, and mode multiplexing devices, etc. have found high-performance integration on silicon platforms [20–23] and the silicon photonics-based transceiver market exhibits a compound annual growth rate (CAGR) of 44.5% from 2018 to 2024 [24], as shown in Fig. 1-1.

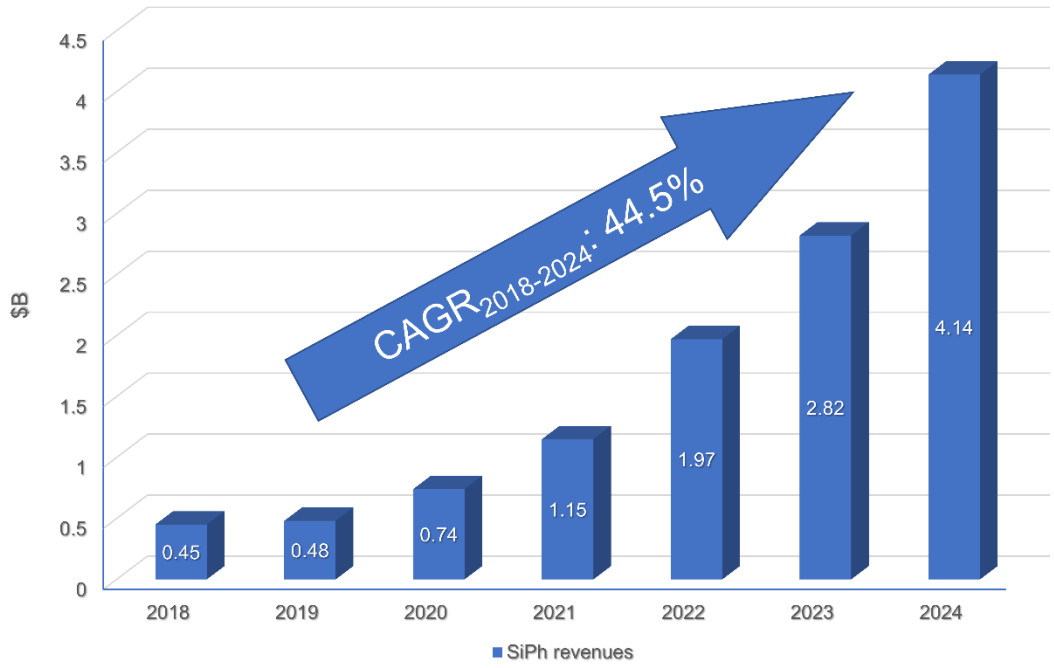

Fig. 1-1 Data of 2018-2024 silicon photonics-based transceiver market forecast [24].

1.2.2 Advantages of silicon photonics integrated optical switches

Silicon photonic integrated optical switches based on the SOI platform have garnered significant attention due to major advantages as follows:

(1) Functional integration: Silicon photonic integrated optical switches can be functionally integrated with active photonic devices and CMOS circuits.

(2) CMOS-compatible fabrication: The fabrication process is compatible with mature CMOS manufacturing technology.

(3) Cost-effective mass production: Mass production using 12-inch SOI wafers significantly reduces costs compared to III-V semiconductors (reducing costs to approximately 1/200).

(4) High density: Silicon photonic integrated optical switches achieve a high device density, with a volume approximately 1/1000 that of silicon dioxide devices.

(5) Low driving power: They exhibit strong thermo-optic and free-carrier plasma dispersion effects, resulting in low power consumption compared to silica-based optical circuits.

These advantages position silicon photonic integrated optical switches as prospective candidates for applications in telecommunication networks, data centers, and high-throughput computing. They offer large bandwidth, low power consumption, and high-level integration.

1.3 All-optical thermo-optic switches

In this section, starting from introducing different typical types of optical switches, the significance of thermo-optic (TO) switches will be analyzed later. Subsequently, the characteristics of all-optical TO switches will be discussed. Then, the comparison of methods of all-optical TO switches will be introduced by reviewing several recent typical devices. Finally, the applications of the proposed all-optical TO switches in this study will be discussed including the prospective performance expected for our proposed device.

1.3.1 Optical switches

Optical switches play importance roles in many applications, including optical cross connection, protection switching, and switch arrays for optical add-drop multiplexing [25]. Nowadays, various kinds of photonics switching technologies are candidates for fiber-optic communication network systems. Here, we introduce several typical types of optical switches as follows.

Electro-optic (EO) switches [26–29] make use of the decrease in reflective index (RI) of materials when a voltage is applied. By injecting charge carriers at the material's interface, the RI can be reduced at one side of the interface, which can cause total internal reflection to take place when light travels from a high to low RI media at the interface. Therefore, the light is reflected rather than transmitted across the interface, enabling the

light to be switched. Changes in RI of one beam path relative to another cause a phase difference between the beams which can lead to constructive or destructive interference when they arrive at the outputs of the two different arms forming the light path. Basically, a typical EO switch [26] offers switching times from 1ns to 1ms, extinction ratio of -10 to -40dB and insertion loss ranging from < 1 to 10dB.

Semiconductor optical amplifier (SOA)-based switches [30–32] are formed of integration of semiconductor optical amplifier and the gating elements which perform to change the wavelength, polarization, phase and amplitude while a light propagates through the optical gain medium as well as the gating function by putting the elements sensitive to the property altered by the amplifier. Such elements, for instance, can be an MZI which can act upon variations in wavelength, polarization and phase.

Magneto-optic (MO) switches [33, 34] are based on the Faraday rotation of polarized light when it passes through magneto-optic material in the direction of an applied field. A transverse MO Kerr effect induces a change in the complex reflectivity of a transverse magnetic (TM)-polarized light dependent on the magnetization direction of the MO material. Therefore, magneto-optic switches can realize the switching by changing the magnetic field dynamically.

Non-linear optical (NLO) switches [35,36] work depending on the light's intensity which induces switching due to optical nonlinearities such as the Kerr effect. Changes in the RI of the optical material take place in response to an applied electric field, which is induced by the light itself, known as the optical Kerr effect. A variation in RI is caused by this which is proportional to the intensity of the light and is responsible for the nonlinear optical effects of self-focusing and self-phase modulation. Consequently, the light experiences a phase shift due to the change in RI that is related to the intensity of its own while propagates in the optical material, which contributes to the switching function of a non-linear optical switch.

Thermo-optic (TO) switches [37–41] make use of the change in RI with temperature. The RI generally increases when the temperature of the material increases. Thus, heating the material changes the RI of the waveguide, imparting a phase difference and altering the selectivity of the output ports. Especially in silicon photonics, benefitting from the

large TO coefficient (1.86×10^{-4} K^{-1} [42]) of the silicon at waveguide of 1.55 μm, silicon TO switches show advantages in terms of high tuning efficiencies and compact footprints, so they have been widely studied for cost-effective and power-efficient optical switching networks.

As mentioned above, TO switches are based on TO effect, which consists of the variation of the RI of a dielectric material, due to a temperature variation of the material itself. The TO effect is present in all materials and is described by the TO coefficient, given by dn/dT, where n is the RI of the material at temperature T. The TO coefficient of silicon in the C-band over the temperature range 300–600 K can be written as [43]

$$\frac{dn}{dT} = 9.45 \times 10^{-5} + 3.47 \times 10^{-7} \times T - 1.49 \times 10^{-10} \times T^2 \ (K^{-1}) \qquad (1.1)$$

Therefore, the RI of a silicon waveguide can be changed through a TO phase shifter which can induce the temperature change by heat. Compared with TO switches, EO switches usually suffer from substantial insertion loss due to free carrier absorption while SOA-based switches and MO switches are hard to fabricate and NLO switches are limited to materials with high nonlinear optical effect. As a result of simple design, easy fabrication, low cost and small footprint, TO switches are widely used for photonics devices and large-scale integrated PICs on the SOI platform [44–46]. The TO switches have response times of microsecond-scale to millisecond-scale, which fit the applications of inter-data center connects and the switching in the telecommunication network nodes.

1.3.2 All-optical switches

All-optical switches are devices using pump light to control the on/off transition of the signal light. In the last few decades, ultra-high speed all-optical switching have been investigated with NLO effects [47, 48]. All-optical packet switching was anticipated, but it has not yet been put to practical use due to the difficulty of synchronization and the need for high pump light intensity. Nowadays, elastic optical networks are expected to be more promising and are being researched. Optical switches are utilized for changing the optical path connection, and so they are required to operate stably even at low speeds. All-optical TO switches in this study enables stable operation like traditional TO

switches due to linear optical absorption of pump light.

Designing the traditional TO switches into all-optical TO switches makes it possible to utilize photons for information processing, avoid optical-electrical-optical (O-E-O) conversion and thus have the potential to achieve low latency, low power consumption and compact footprint in all-optical signal processing. An all-optical TO switching process is achieved by using the TO phase shifter. When the pump light is induced to the switch, the TO effect can be effectively used by the TO phase shifter where heat is generated from the heater's absorption of the pump light. Thus, the modulation of the signal light is tuned by the pump control light and the TO effect is used for the construction of the all-optical TO switch.

Therefore, comparing to traditional TO switches with electrodes, all-optical TO switches show advantages that we can remotely control the switching process using the pump control lights and remotely adjust the temperature for calibration. Moreover, all-optical TO switches do not require any power supply, thermo-electric cooler or digital-to-analog converters at the field around the switch, and consequently, can be installed in small-volume modules in fiber-optic communication systems.

1.3.3 Comparison of methods of all-optical thermo-optic switches

As mentioned in previous section, TO phase shifter can produce phase change in the signal light by the heat-induced change of RI of the all-optical TO switch. Recently, several all-optical TO switches based on different heaters using for the tuning mechanisms of TO phase shifters have been demonstrated [49–56].

Graphene, a two-dimensional (2D) carbon atoms material, is employed as the heater by several groups [49–53] owing to well electrical and optical properties, including its linear absorption in a broad spectral range and the large nonlinearity, a high thermal conductivity and the direct interaction with waveguides with a low optical absorption rate. C. Qiu et al. [49] have proposed a high-performance graphene-on-silicon nitride (Si_3N_4) all-optical switch based on a Mach–Zehnder interferometer (MZI), exhibited an extinction ratio of 11 dB with a switching power of 109 mW and a fast switching time of

571 ns and 1.29 μs for the rising time and the falling time, respectively. This device performed a total insertion loss of around 4 dB. An all-optical switch based on a graphene-on-silicon nanobeam cavity has been demonstrated by T. Guo et al. [52]. It obtained a high extinction ratio of 16 dB with a switching power of 47 mW with the insertion loss of around 1 dB for both the pump and probe light and demonstrated the all-optical control of a single resonance channel. L. Jiang et al. [53] aimed to realize a low power consumption of all-optical switch based on the graphene-buried structure, as shown in Fig. 1-2 (a). They used a sufficiently long graphene length of 5 mm to generate enough heat from a low pump power and their device performed a high extinction ratio of 36 dB with a switching power of only 3.8 mW and an insertion loss of 1.1 dB for the signal light but suffered from slow rising/falling times of 1.0 and 2.7 ms, respectively.

Heavily doped Si waveguide is another heater used for the all-optical TO switch demonstrated by L. Li et al. [54] as shown in Fig. 1-2 (b). Their device used the heavily doped Si waveguide to absorb pump light by free carrier absorption and diffuse the generated heat to the adjacent signal waveguide. Both MZI and MRR structures are used in their experiment. For the MZI structure, insertion loss of the signal light was 0.9 dB due to the coupling loss and it performed a minimum π phase shift power of 18 mW. Switching times were also measured in the MZI structure, which yielded rising/falling times of 14 and 13 μs, respectively. For the MRR structure,

The metal heater has also been investigated to realize the all-optical TO switching by our group [46–47]. The first demonstration of an MRR using the titanium heater was made by T. Murai et al. [55] as shown in Fig. 1-2 (c). The tuning efficiency of the device was 0.075 nm/mW with an absorption loss of 1.65 dB by the metal layer and a switching time less than 1 μs. Y. Kondo et al. [56] has demonstrated an all-optical TO switch, as shown in Fig. 1-2 (d), which was based on the metal heater realizing a burst switching with a switching ratio of 5.7 dB and 2.4 dB for the drop port and through port, respectively. The peak pump power of the burst switching was around 20 mW for this device while the absorption loss by the metal was measured to be 1.2 dB and the switching time was around 1 μs.

Here, we have summarized the related researches of all-optical TO switches using

different methods for the heating process as shown in Table 1-1.

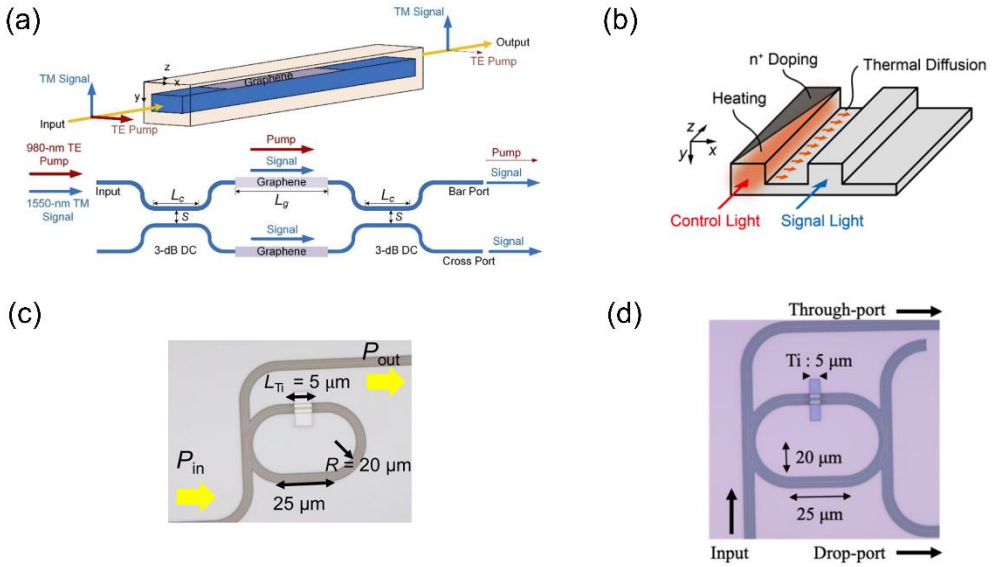

Fig. 1-2 (a) Schematic structure of reported graphene-based all-optical TO switches. (b) 3-D structure of n^+ doping waveguide heater. (c–d) Micrographs of all-optical switches based on metal heaters [53–56].

Table 1-1. Comparison of recent reported all-optical TO switches.

Structure	**Heater materials**	**Switching power**	**Switching time (rise/fall)**	**Extinction ratio**	**Insertion loss**	**Reference**
MZI	Graphene	109 mW	0.57/1.29 μs	11 dB	~4 dB	[49]
MRR	Graphene	0.0079 nm/mW	0.25/1.95 μs	10 dB	>0.5 dB	[50]
MRR	Graphene	0.216 nm/mW	0.2/1.5 μs	17 dB	0.7 dB	[51]
Nanobeam cavity	Graphene	0.0346 nm/mW	3.2/5.5 μs	16 dB	~1 dB	[52]
MZI	Graphene	3.8 mW	1.0/2.7 ms	36 dB	1.1 dB	[53]
MZI	Heavily doped Si	18 mW	14/13 μs	~18 dB	0.9 dB	[54]
MRR	Heavily doped Si	0.18 nm/mW	N/A	~9 dB	>0.9 dB	[54]
MRR	Metal (Ti)	0.075 nm/mW	<1 μs	~22 dB	>1.65 dB	[55]

MRR	Metal (Ti)	~20 mW	~1 μs	11 dB	>1.2 dB	[56]

1.3.3 Application of all-optical thermo-optic switches

In order to introduce the applications of the all-optical TO switches proposed in this study, passive optical network (PON) systems will be introduced firstly as the background. A conventional time division multiplexing (TDM)-PON will be discussed and the applications of the proposed all-optical TO switches will be discussed next.

1.3.3.1 Passive optical network system

A PON system consists of a central office node, called an optical line terminal (OLT), one or more user nodes, called optical network units (ONUs) or optical network terminals (ONTs), and optical distribution network (ODN), comprised of the fibers and splitters between OLT and ONUs. An OLT provides the interface between the PON and the backbone network. An ONU is a device that terminates the PON and presents customer service interfaces to the user. Some ONUs can implement a separate subscriber unit to provide services such as telephony, Ethernet data, or video. Based on the data multiplexing scheme, PON has three main types and a currently deployed PON technology is TDM-PON, where traffic to multiple ONUs is TDM-multiplexed on the downstream signal. Wavelength division multiplexing (WDM)-PON and orthogonal frequency division multiplexing (OFDM)-PON are two other PON technologies. WDM-PON uses multiple wavelengths to assign traffic to ONUs, while OFDM-PON uses multiple orthogonal subcarriers to transmit traffic to ONUs. The capacity of global PON systems has growth from 1Gbps to 40 Gbps these years [57].

For a conventional TDM-PON, as shown in Fig. 1-3, the signals from the OLT are broadcasted to all users and the time slots are shared. Splitters are used in the TDM-PON to select the signals transmitted to ONUs. Consequently, due to the facts that ONUs share bandwidth, this system has limited scalability. In addition, TDM-PON is not very secure due to the shared infrastructure which opens the possibility of eavesdropping and other

attacks [58].

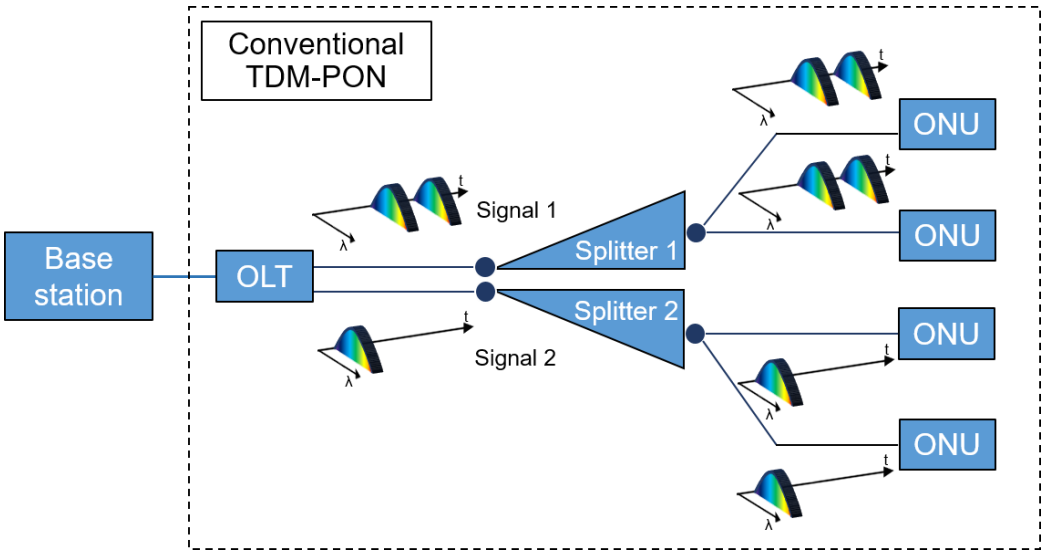

Fig. 1-3 Architecture of a conventional TDM-PON system. (TDM-PON: time division multiplexing-passive optical network, OLT: optical line termination, ONU: optical network unit)

1.3.3.2 Remotely controllable passive optical network system

As shown in Fig. 1-4, we propose an upgrade from conventional TDM-PON to remotely controllable TDM-PON based on the all-optical TO switches demonstrated in this study. The proposed system consists of an OLT, a wavelength division multiplexing (WDM) coupler, an arrayed waveguide grating (AWG), the proposed all-optical TO switch and ONUs. By using the WDM coupler, data or the signal lights sending from the base station together with the pump control lights can be separated by different waveguide ranges. Here, we assume that the pump control lights are in the L-band wavelength range (λ = 1565–1625 nm) while the signal lights are among C-band wavelength range (λ = 1530–1565 nm). Then, using the AWG filter, pump control lights with different wavelengths are divided into different input ports of the all-optical TO switch while the signal lights are also inputted into the all-optical TO switch simultaneously. In this way, the signal light can be switched to certain output port of the all-optical TO switch by inducing the pump control lights remotely, which means only

the signal needed by certain user will be transferred to the selected ONU.

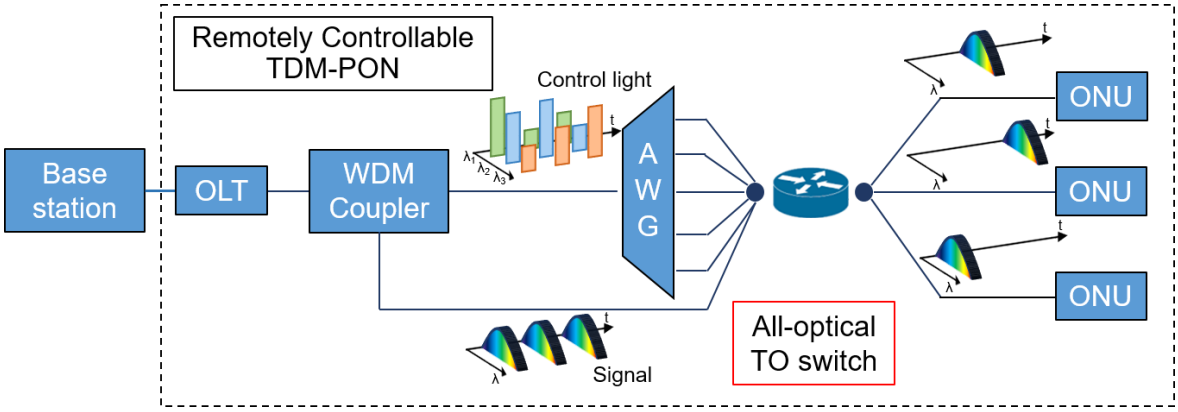

Fig. 1-4 Architecture of a remotely controllable TDM-PON system. (WDM: wavelength division multiplexing, AWG: arrayed waveguide grating)

In a conventional TDM-PON system, the time slot for users is shared, but only selected at each node from the signal equally divided by a passive optical splitter. However, as demonstrated in this remotely controllable TDM-PON system, efficient burst switching can be realized by applying the proposed all-optical TO switch in this study. Therefore, this dynamic switching system can increase the efficiency in the time domain, whereas an optical switch must be installed in a field with external disturbances as well as less volume and power supply. The proposed all-optical TO switch enables path switching and thermal tuning from a base station. It does not require any power supply or digital-to-analog converters at the field around the switch, and therefore, can be installed in a small-volume module.

1.3.4 Prospective performance of remotely controllable passive optical network system utilizing all-optical thermo-optic switch

For the application in next-generation fiber-optic communication system, prospective performance of remotely controllable TDM-PON systems utilizing our proposed all-optical thermo-optic switch in this research will be discussed in the following.

As introduced in Section 1.3.3.1, users share the broadcasted signals from the OTL through a splitter in a conventional TDM-PON system. Typically, 32 ONU (or user) slots

were used in the conventional PON system with a bit rate up to 10 Gbps [57] and thus, the split ratio was 1:32, which is supposed to be theoretically 1:1 by using the idea of our remotely controllable TDM-PON system with a 1×32 switch. Since this is a great advantage by using our proposed system compared to conventional one, we use power budget to describe this beneficial effect owing to the increased transmitted power, as shown in Fig. 1-5. Total power budget for the downstream signals is assumed to be 29 dB excluding a transmitter and dispersion penalty (TDP) of 1.5 dB based on a 10G Ethernet PON (10G-EPON) system [59]. Within the total power budget, ideally, the average transmitted power is 32 times (~ 15.05 dB) larger in our proposed system without any loss compared to conventional system using the proposed all-optical TO switch instead of splitter, which indicates a power budget of around 15.05 dB. With the same energy, according to Eq. (1.2), where P_b, E_b and R_b refer to signal average power per bit, average energy per bit and bit rate, respectively, bit rate of our proposed system can be expected to be 32 times faster with this power budget, which should be slower by considering the loss inside the system.

$$P_b = E_b \cdot R_b \,. \tag{1.2}$$

Here, we set the target of our proposed system performance as a bit rate up to 100 Gbps (10 times faster compared to conventional system), i.e., a 10-dB extra power budget should be earned in our proposed system, revealing that the loss should be lower than 5 dB (= 15 – 10 dB) in the system. It will be a large upgrade even if it costs extra power utilizing the switch instead of splitter. The loss is mainly due to the coupling loss between lensed fibers and chip (~ 0.5×2 dB for input and output) as well as the insertion loss of the 1×32 switch, which is cascaded by five-stages of 1×2 switch. Consequently, the target insertion loss of a single 1×2 switch should be lower than 0.8 dB in order to realize a 100 Gbps bit rate of our proposed remotely controllable TDM-PON system.

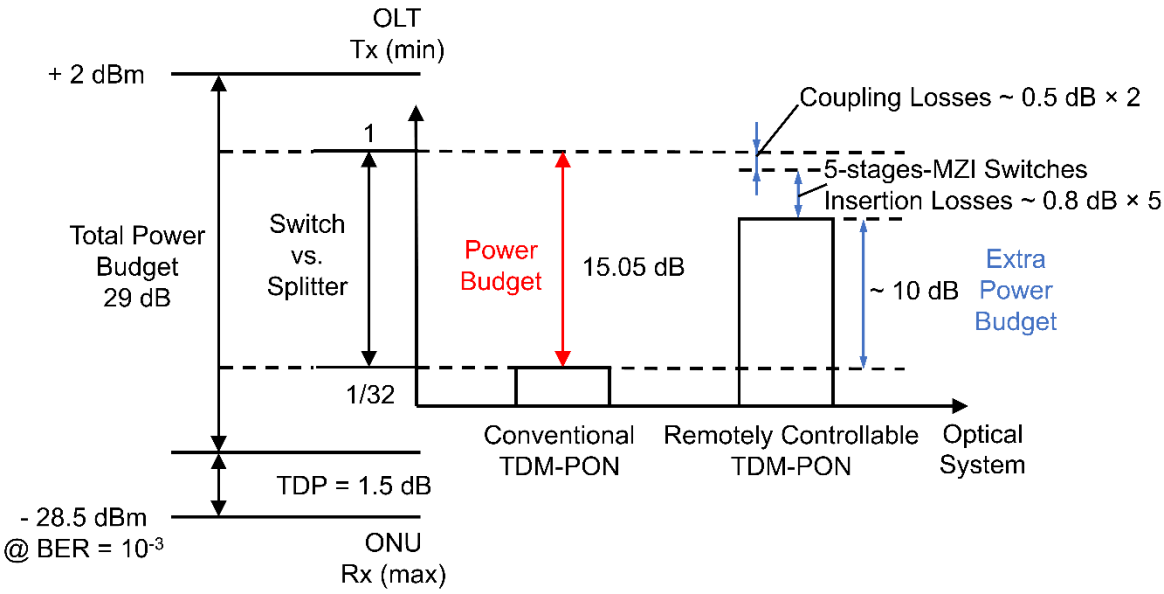

Fig. 1-5 Calculated power budget for remotely controllable TDM-PON system compared to conventional TDM-PON system. (Tx: transmitter, Rx: receiver, BER: bit error rate, TDP: transmitter and dispersion penalty)

On the other hand, according to the demonstration of a 10G-EPON system [59,60], bit error rate (BER) of 10^{-3} was required for 10G downstream PR(X)30 standard. A BER of lower than 10^{-3} for our proposed switch is required and forward error correction (FEC) should be adopted to our proposed PON system. Considering the on-off keying modulation of our proposed switch, relation of BER and signal to noise ratio (SNR) can be expressed as (see Appendix A1 for detailed explanation of important parameters related to optical communication systems)

$$BER = \frac{1}{2}\, erfc\left(\sqrt{\frac{SNR}{2}}\right). \tag{1.3}$$

Hence, BER = 10^{-3} corresponds to a SNR of approximately 9.8 dB, as shown in Fig.1-6. Therefore, the target extinction ratio of our proposed switch should be larger than 10 dB in order to realize a practical PON system.

Last but not least, switching time is an important characteristic for the PON system. According to the standard of next generation passive optical network 2 (NG-PON2) [61,

62], tuning time should be less than 10 μs for Class 1 devices which were characterized by the shortest tuning time. Therefore, the target switching time of our proposed switch should be less than 10 μs.

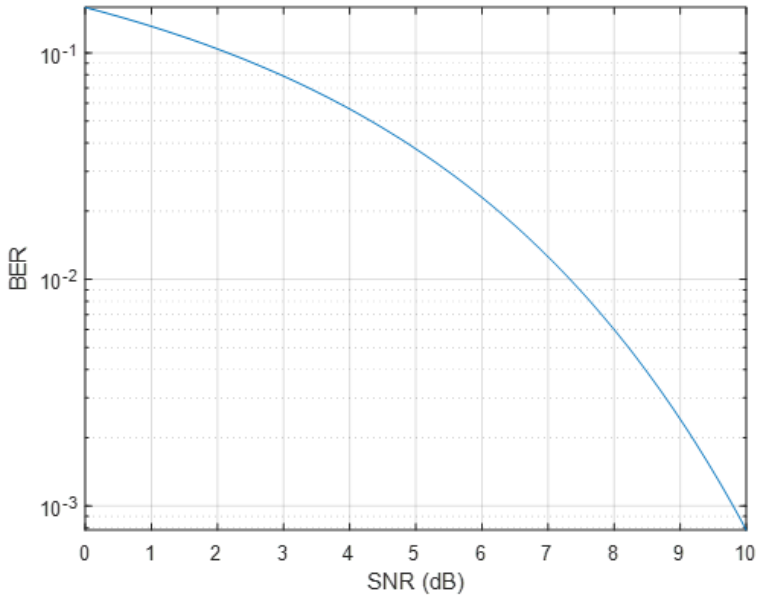

Fig. 1-6 Relationship between bit error rate and signal to noise ratio for on-off keying modulation.

Consequently, comparing with WDM-PON systems, our switching-based TDM-PON system requires simple light sources for generating data signal with specific wavelength in OLT and ONUs. The time slot is flexibly changed on demand from the user. The pump control lights can have narrow bandwidth and be amplified at the same time in OLT. The comparison of PON systems is shown in Table. 1-2.

Table 1-2. Comparison of PON systems.

	Conventional TDM-PON (XG-PON)	**WDM-PON**	**TWDM-PON (NG-PON2)**	**Remotely-controllable TDM-PON**
Bit rate per user	10 Gbps	10 Gbps	40 Gbps (10 G×4 λ)	100 Gbps
Time efficiency	High	Low	High	High
Remote node	Splitter	AWG	Splitter	All-optical TO switch (This work)

Additional units in OLT	-	WDM couplers	WDM couplers	WDM couplers for pump lights
Additional units in ONU	-	TLD	TLD, WDM couplers	-

1.4 Silicon-based integrated all-optical switches based on thermo-optic effect

Owing to the TO phase shift caused by the metal heaters, the integrated all-optical TO switches can be designed and prepared on an SOI platform. Generally, there are two typical structures to design the all-optical TO switches demonstrated in this research, which are microring resonators (MRRs) and Mach-Zehnder interferometers (MZIs). In this section, these two kinds of structures to design the silicon-based integrated all-optical TO switches will be discussed, including the pros and cons of both of them.

1.4.1 Microring resonators type

MRR is one of the most common integrated optical components in PICs. MRR-based switches offer a wavelength selective filtering feature and are suitable for WDM systems in fiber-optic communications. An all-pass MRR consists of an input/output straight waveguide and a microring, while an add-drop MRR consists of two waveguides and a microring coupled to both of them. Here, we use three add-drop MRRs for the demonstration of the all-optical TO switch to realize multiple outputs, as shown in Fig. 1-7. $Out_{1–3}$ are the outputs at the drop ports of each MRRs. With well-designed microrings, each MRR should have particular resonant wavelengths as the pump-off state shown in Fig. 1-8 when the transverse electric (TE)-mode-polarized signal light is inputted. If we induce a TM-mode-polarized pump control light, light-to-heat conversion will be occurred at the metal heaters embedded above the microrings and TO phase shifts will be implemented. As the pump-on state shown in Fig. 1-8, it results in the switching of certain resonant wavelengths at the drop ports. Note that, we use a wavelength range for pump control light different from the wavelength range used for the signals.

The MRR-based all-optical TO switch can be expected to have compact sizes and relatively low tuning power consumption owing to its high modulation efficiency for heating and phase shift. However, on one hand, the transmission spectrum of the MRR has a Lorentzian line-shape [63] which limits the optical bandwidth and the crosstalk between adjacent channels. On the other hand, the resonant wavelength of the MRR is sensitive to the fabrication errors, laser wavelength drift, on-chip temperature changes and thus the wavelength alignment and stabilization are very challenging.

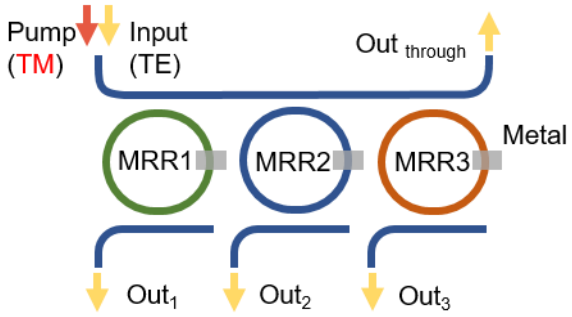

Fig. 1-7 Schematic of the MRR-based all-optical TO switch.

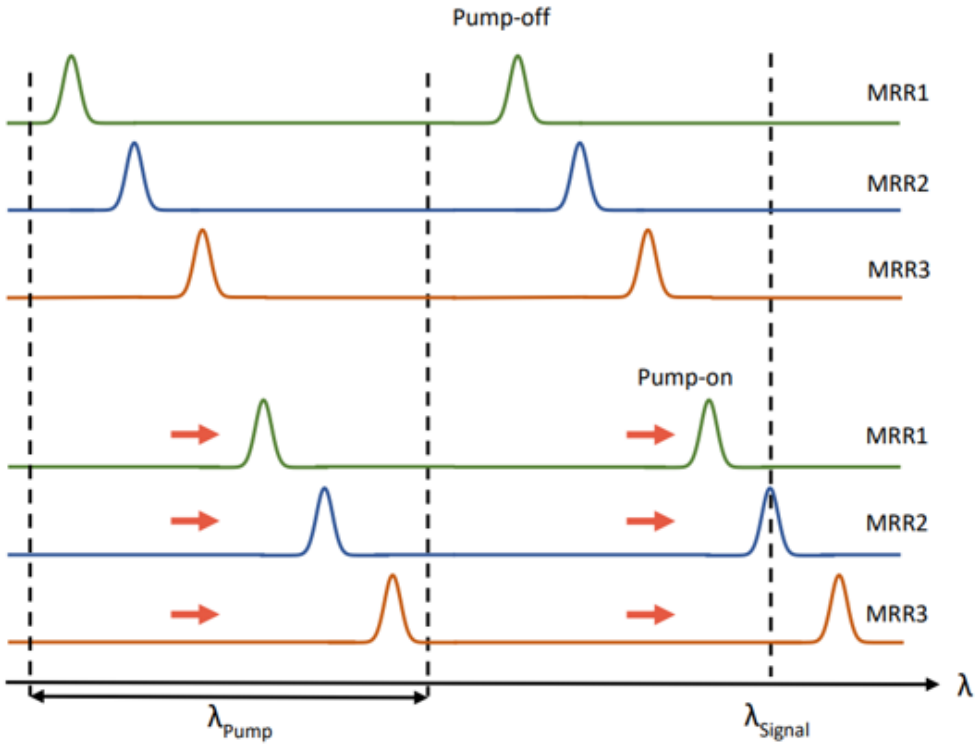

Fig. 1-8 Signal switching at the drop ports of the MRR-based all-optical TO switch.

1.4.2 Mach-Zehnder interferometers type

MZIs are also among the most widely used configurations of PICs. MZI-based switches are suitable for space switching in fiber-optic communications because of no limitation by channel spacing and grid configuration. A typical MZI is composed of two 3 dB couplers for the input/output and two waveguide arms between them. The optical lengths of two arms are equal to each other for a symmetric MZI while an asymmetric MZI contains an optical delay line in the arms. 3 dB couplers can be realized by 1×2 or 2×2 multimode interferometer (MMI) coupler, directional coupler (DC), or mode evolution structure. By cascading the elementary units, 1×2 MZI-based switches, a 1×N MZI-based switch can be realized. A demonstration of a 1×N MZI-based all-optical TO switch is illustrated as Fig. 1-9. As shown in Fig. 1-9, each 1×2 MZI has an extra waveguide adjacent to one arm for inducing the TM-polarized pump control light. The area with the metal deposited above the waveguides is the TO modulation area, which is also called as the TO phase shifter. As the pump control light is induced, the pump light is then absorbed by the metal heater and thus, phase shift occurs due to the TO effect caused by light-to-heat conversion. The output states can be alternated when the phase difference between two arms corresponds to π owing to phase interference. We can use certain combination of the pump control lights induced to selected 1×2 MZIs to control the switching process. For instance, the off-state (low-transmittance) Out $_N$-off output port can be switched to on-state (high-transmittance) Out $_N$-on by inducing the pump control lights, as shown in Fig. 1-10. There are broadband operation wavelengths for a well-designed 1×N MZI-based all-optical TO switch with balanced loss between two arms of each 1×2 MZI.

The demonstrated 1×N MZI-based all-optical TO switch realizes broadband switching and is suitable for WDM and modulation systems. The high scalability and feasibility of MZI makes it possible to build up large-scale multiple input/output ports optical switches. Also, the MZI-based switch can trim the fabrication-induced initial phase errors by

applying additional pump light to the other ports. However, the modulation area or the phase shifter of MZI is usually large compared to MRR which will cause a larger footprint.

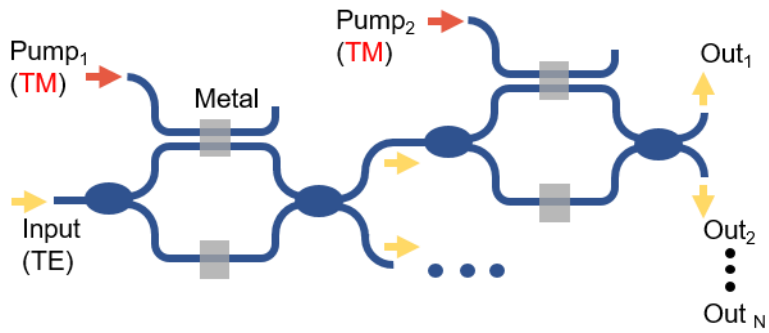

Fig. 1-9 Schematic of the 1×N MZI-based all-optical TO switch.

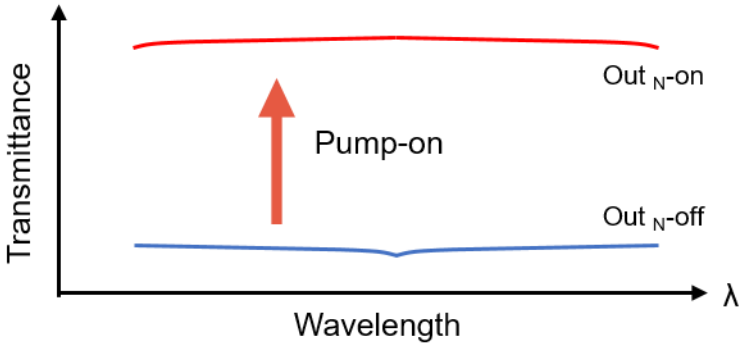

Fig. 1-10 Broadband switching of a 1×N MZI-based all-optical TO switch.

1.5 Research objective and dissertation organization

Benefiting from the mature, low-cost and robust process of silicon semiconductor device on silicon platforms, silicon-based all-optical TO switches can be expected to make a massive contribution to optical communication networks in the future. In this section, the objective of this research as well as the organization of this dissertation will be described.

1.5.1 Research objective

Considering the requirements for optical switches as well as the advantages of silicon photonics, in this dissertation, the all-optical remotely controllable silicon thermo-optic switches will be proposed and demonstrated. Based on the previous studies [55,56], we will design the MRR-based all-optical TO switch first to verify the efficient tuning by the TM-mode-polarized pump light to control the TE-mode-polarized signal light. MRR configuration allows efficient heating at a small volume due to TO effect within looped cavity. By reducing the absorption loss for the signal light, higher extinction ratio is expected. Then we will design the 1×2 MZI-based all-optical TO switch for the preparation of designing large-scale switches. By designing the TO phase shifter with metal heater utilizing light-induced heat, sufficient phase shift can be realized without looped structure. Finally, we will further realize a 1×8 MZI-based all-optical TO switch which can find the application in passive optical network systems to achieve remote control in all-optical signal processing.

1.5.2 Dissertation organization

This dissertation is divided into five chapters as shown in Fig. 1-11. In Chapter 1, we have shown the background of optical communication and optical switching technologies, the development and significance of silicon photonics and the introduction and discussion of the all-optical thermo-optic switches.

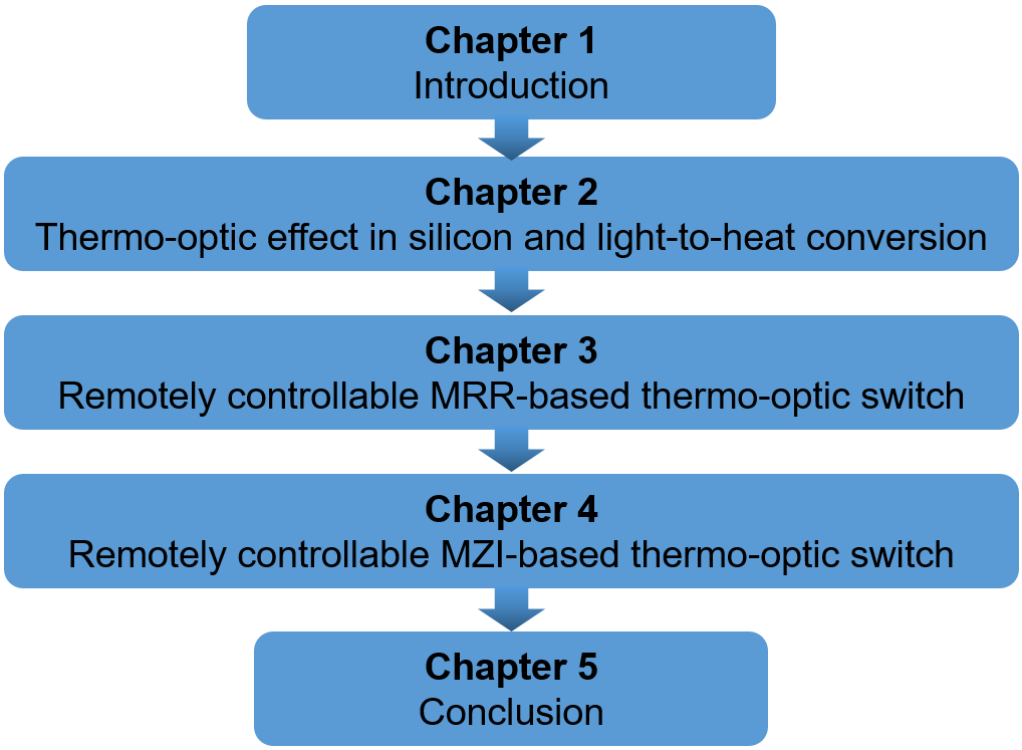

Fig. 1-11 Organization of this dissertation.

Chapter 2 will explain the basic theory of TO effect on an SOI platform and the principle of light-to-heat conversion in the all-optical TO phase shifter with a metal heater.

Chapter 3 will describe the demonstration of the MRR-based TO switch in order to verify the method of using the metal to tune the TO phase shifter efficiently as the preparation to design a high-performance all-optical TO switch.

Chapter 4 will analyze the design of the 1×2 MZI-based all-optical TO switch and describe the demonstration of the 1×8 MZI-based all-optical TO switch, which has the application for all-optical remote control of signal processing in passive optical network systems in the future.

In Chapter 5, we will briefly summarize all the work and look forward to future research directions.

References

1. J. Bardeen and W. H. Brattain, “The transistor, a semi-conductor triode,” Phys. Rev. 74, 230–232 (1948).
2. J. S. Kilby, “Miniaturized electronic circuits,” U.S. Patent 3,138,743, Jun.23, 1964.
3. R.S. Williams, “What's next?[The end of Moore's law],” Computing in Science & Engineering 19(2), 7-13 (2017).
4. S.E. Miller, “Integrated optics: An introduction,” The Bell System Technical Journal 48(7), 2059-2069 (1969).
5. L.C. Kimerling, “Silicon microphotonics,” Applied Surface Science 159, 8-13 (2000).
6. E. B. Basch, R. Egorov, S. Gringeri, S. Elby, “Architectural tradeoffs for reconfigurable dense wavelength-division multiplexing systems,” IEEE J. Sel. Top. Quantum Electron. 12, 615–626 (2006).
7. R. Jensen, A. Lord, N. Parsons, “Colourless, directionless, contentionless ROADM architecture using low-loss optical matrix switches,” Proceedings of the 2010 European Conference on Optical Communication in Turino, Italy. 19–23 (2010).
8. P.D. Colbourne, B. Collings, “ROADM Switching Technologies,” Proceedings of the 2011 Optical Fiber Communications Conference in Los Angeles, CA, USA. 6–10 (2011).
9. Lin, Gong-Ru, et al., “Si-rich SiNx based Kerr switch enables optical data conversion up to 12 Gbit/s,” Scientific Reports 5(1), 9611 (2015).
10. L. Schares et al., “A Throughput-Optimized Optical Network for Data-Intensive Computing,” in IEEE Micro 34(5), 52-63 (2014).
11. X. Tu, C. Song, T. Huang, Z. Chen, H. Fu, “State of the Art and Perspectives on Silicon Photonic Switches,” Micromachines. 10(1), 51 (2019).
12. Y. Shi, Y. Zhang, Y. Wan, Y. Yu, Y. Zhang, X. Hu, X. Xiao, H. Xu, L. Zhang, and B. Pan, “Silicon photonics for high-capacity data communications,” Photon. Res. 10, A106-A134 (2022).
13. R. A. Soref and J. P. Lorenzo, “Single-Crystal Silicon: A New Material For 1.3 And 1.6 μm Integrated-Optical Components,” Electron. Lett. 21(21), 953–954 (1985).
14. R. A. Soref and B. R. Bennett, “Electrooptical effects in silicon,” IEEE J. Quantum Electron. 23(1), 123–129 (1987).

15. R. A. Soref, J. Schmidtchen, and K. Petermann, “Large Single-Mode Rib Waveguides in GeSi-Si and Si-on-SiO2,” IEEE J. Quantum Electron. 27(8), 1971–1974 (1991).
16. A. G. Rickman, G. T. Reed, and F. Namavar, “Silicon-on-Insulator Optical Rib Waveguide Loss and Mode Characteristics,” J. Light. Technol. 12(10), 1771–1776 (1994).
17. A. Liu, R. Jones, L. Liao, et al. “A high-speed silicon optical modulator based on a metal–oxide–semiconductor capacitor,” Nature 427, 615–618 (2004).
18. S. Manipatruni, Q. Xu, and M. Lipson, “PINIP based high-speed high-extinction ratio micron-size silicon electro-optic modulator,” Opt. Express 15(20), 13035-13042 (2007).
19. K. Li et al., “Electronic–photonic convergence for silicon photonics transmitters beyond 100 Gbps on–off keying,” Optica 7(11), 1514–1516 (2020).
20. W. Yang, J. Chen, Y. Zhang, Y. Zhang, J. He and X. Fang, “Silicon‐compatible photodetectors: trends to monolithically integrate photosensors with chip technology,” Advanced Functional Materials 29(18), 1808182 (2019).
21. G. T. Reed, G. Mashanovich, F. Y. Gardes and D. Thomson, “Silicon optical modulators,” Nature Photonics 4(8), 518-526 (2010).
22. P. Dong, “Silicon photonic integrated circuits for wavelength-division multiplexing applications,” IEEE Journal of Selected Topics in Quantum Electronics 22(6), 370-378 (2016).
23. D. Dai, J. Wang and S. He, “Silicon multimode photonic integrated devices for on-chip mode-division-multiplexed optical interconnects (invited review),” Progress In Electromagnetics Research 143, 773-819 (2013).
24. E. Mounier and J.-L. Malinge, “Silicon Photonics and Photonic Integrated Circuits 2019 - Yole Développement,” https://medias.yolegroup.com/uploads/2019/04/YD19015_Silicon_Photonics_SiPh_and_Photonic_IC_PIC_yole_sample.pdf
25. J. Gosciniak, S. Bozhevolnyi, “Performance of thermo-optic components based on dielectric-loaded surface plasmon polariton waveguides,” Sci Rep 3, 1803 (2013).
26. Y. Enami, D. Mathine, C. T. DeRose, R. A. Norwood, J. Luo, A. K-Y. Jen, N. Peyghambarian, “Hybrid electro-optic polymer/sol-gel waveguide directional coupler

switches," Appl. Phys. Lett. 94 (21), 213513 (2009).
27. J. Shang, J. Sun, Q. Li, et al., "Single-block pulse-on electro-optic Q-switch made of $LiNbO_3$," Sci Rep 7, 4651 (2017).
28. L. Qiao, W. Tang, and T. Chu, "32×32 silicon electro-optic switch with built-in monitors and balanced-status units," Sci Rep 7, 42306 (2017).
29. X. Liu et al., "Ferroelectric crystals with giant electro-optic property enabling ultracompact Q-switches," Science 376, 371-377(2022).
30. I. Armstrong, I. Andonovic, and A. Kelly, "Semiconductor optical amplifiers: performance and applications in optical packet switching [Invited]," J. Opt. Netw. 3, 882-897 (2004).
31. K. A. Williams, "Integrated semiconductor-optical-amplifier-based switch fabrics for high-capacity interconnects [Invited]," J. Opt. Netw. 6, 189-199 (2007)
32. T. Sutili, P. Rocha, C. M. Gallep, and E. Conforti, "Energy Efficient Switching Technique for High-Speed Electro-Optical Semiconductor Optical Amplifiers," J. Lightwave Technol. 37, 6015-6024 (2019)
33. T. Murai, Y. Shoji, N. Nishiyama and T. Mizumoto, "Wavelength-tunable operation of magneto–optical switch consisting of amorphous silicon microring resonator on garnet," Jpn. J. Appl. Phys. 58 (7), 072006 (2019).
34. T. Murai, Y. Shoji, N. Nishiyama and T. Mizumoto, "Magneto-optical microring switch based on amorphous silicon-on-garnet platform for photonic integrated circuits," IEICE Transactions on Electronics 103(11), 645-652 (2020).
35. F. Castet, V. Rodriguez, J. L. Pozzo, L. Ducasse, A. Plaquet and B. Champagne, "and characterization of molecular nonlinear optical switches," Accounts of chemical research 46(11), 2656-2665 (2013).
36. F. Mançois, et al., "Acido-triggered nonlinear optical switches: Benzazolo-oxazolidines," The Journal of Physical Chemistry B 111(33), 9795-9802 (2007).
37. Z. Zhou, B. Yin, Q. Deng, X. Li, and J. Cui, "Lowering the energy consumption in silicon photonic devices and systems," Photon. Res. 3, B28–B46 (2015).
38. B. Stern, X. Zhu, C. P. Chen, et al., "On-chip mode-division multiplexing switch," Optica 2, 530–535 (2015).
39. J. Wang, H. Shen, F. Li, et al., "Reconfigurable radio-frequency arbitrary waveforms

synthesized in a silicon photonic chip," Nat. Commun. 6, 5957 (2015).

40. S. Yan, X. Zhu, L. H. Frandsen, et al., "Slow-light-enhanced energy efficiency for graphene microheater on silicon photonic crystal waveguides," Nat. Commun. 8, 14411 (2017).
41. R. Zhang, Y. He, Y. Zhang, et al., "Ultracompact and low-power-consumption silicon thermo-optic switch for high-speed data," Nanophotonics 10 (2), 937-945 (2021).
42. I. Rendina, "Thermo-optical modulation at 1.5m in silicon etalon," Electron. Lett. 28(1), 83–85(2) (1992).
43. G. Cocorullo, F. G. Della Corte, and I. Rendina, "Temperature dependence of the thermo-optic coefficient in crystalline silicon between room temperature and 550 K at the wavelength of 1523 nm," Appl. Phys. Lett.74(22), 3338–3340 (1999).
44. M. Jacques, A. Samani, E. El-Fiky, D. Patel, Z. Xing, and D. V. Plant, "Optimization of thermo-optic phase-shifter design and mitigation of thermal crosstalk on the SOI platform," Opt. Express 27, 10456-10471 (2019).
45. J. Van Campenhout, W. M. J. Green, S. Assefa, and Y.A. Vlasov, "Integrated NiSi waveguide heaters for CMOS-compatible silicon thermo-optic devices," Opt. Lett. 35, 1013-1015 (2010)
46. X. Qiang, X. Zhou, J. Wang, et al., "Large-scale silicon quantum photonics implementing arbitrary two-qubit processing," Nature Photon 12, 534–539 (2018).
47. B. Gholipour, et al, "An all-optical, non-volatile, bidirectional, phase-change meta-switch," Advanced materials 25(22), 3050-3054 (2013).
48. W. Yu, S. Zheng, Z. Zhao, B. Wang and W. Zhang, "Reconfigurable Low-Threshold All-Optical Nonlinear Activation Functions Based on an Add-Drop Silicon Microring Resonator," in IEEE Photonics Journal 14(6), 1-7 (2022).
49. C. Qiu, C. Zhang, H. Zeng, and T. Guo, "High-performance graphene-on-silicon nitride all-optical switch based on a Mach-Zehnder interferometer," J. Lightwave Technol. 39(7), 2099–2105 (2021).
50. C. Qiu, Y. Yang, C. Li, Y. Wang, K. Wu, and J. Chen, "All-optical control of light on a graphene-on-silicon nitride chip using thermo-optic effect," Sci. Rep. 7(1), 1–7 (2017).
51. Z. W. Li, Q. Liu, H. Wang, M. Deng, Q. Huang, and Y. Wang, "Photo-induced

thermo-optical refraction switching by a graphene-assisted silicon microring resonator," J. Lightwave Technol. 39(11), 3471–3477 (2021).

52. T. Guo, S. Gao, H. Zeng, et al., "All-optical control of a single resonance in a graphene-on-silicon nanobeam cavity using thermo-optic effect," J. Lightwave Technol. 39(14), 4710–4716 (2021).
53. L. Jiang, Q. Huang, and K. S. Chiang, "Low-power all-optical switch based on a graphene-buried polymer waveguide Mach-Zehnder interferometer," Opt. Express 30, 6786-6797 (2022).
54. L. Li, T. Tamanuki, and T. Baba, "All-optic control using a photo-thermal heater in Si photonics," Opt. Express 30, 41874-41883 (2022).
55. 村井 俊哉, "シリコンリング共振器を用いた 導波路型光メモリに関する研究," 東京工業大学 工学院 電気電子系 電気電子コース, (2019).
56. 近藤 優一郎, "非線形光学効果を用いた材料特性評価と全光スイッチに関する研究," 東京工業大学 工学院 電気電子系 電気電子コース, (2020).
57. H. S. Abbas and M. A. Gregory, "The next generation of passive optical networks: A review," Journal of Network and Computer Applications 67, 53-74 (2016).
58. K. Hara, S. Kimura, H. Nakamura, N. Yoshimoto, and H. Hadama, "New AC-Coupled Burst-Mode Optical Receiver Using Transient-Phenomena Cancellation Techniques for 10 Gbit/s-Class High-Speed TDM-PON Systems," J. Lightwave Technol. 28, 2775-2782 (2010).
59. F. Daido, T. Inoue, Y. Kawanishi, K. Yamazaki, A. Yoshimura, S. Shiba, S. Kouyama, "Development of asymmetric 10G-EPON system," SEI Technical Review 69, (2009).
60. Asymmetric 10G EPON ONU SFP+ 1310nm / 1577nm PRX30 Transceiver, https://wavesplitter.com/wp-content/uploads/2024/03/WST-SFPEPAU2-C.pdf
61. NG-PON2 Council, https://www.broadband-forum.org/ng-pon2-council
62. J. Shan Wey, D. Nesset, M. Valvo, K. Grobe, H. Roberts, Y. Luo, and J. Smith, "Physical Layer Aspects of NG-PON2 Standards—Part 1: Optical Link Design [Invited]," J. Opt. Commun. Netw. 8, 33-42 (2016).
63. W. Bogaerts, P. De Heyn, T. Van Vaerenbergh, K. De Vos, S. Kumar Selvaraja, T. Claes, P. Dumon, P. Bienstman, D. Van Thourhout, R. Baets, "Silicon microring resonators," Laser & Photon. Rev. 6(1), 47-73 (2012).

Chapter 2

Thermo-optic effect in silicon and light-to-heat conversion

2.1 Introduction

In this study, thermo-optic (TO) effect in silicon and light-to-heat conversion by the light absorption from the metal layer deposited above the silicon waveguide with a short distance between them are crucial principles in the design of our proposed device. TO effect applied in conventional TO phase shifter or TO switch has been widely investigated by a lot of researchers [1–3]. However, the light-induced TO effect remains a large potential to be efficiently utilized in all-optical TO switch.

In this chapter, we will discuss TO effect in silicon and its application in TO phase shifter at first. When a metal heater is employed to induce TO phase shift while applying a high-intensity pump light to the device, non-linear effects are negligibly small compared to TO effect, which will be discussed in the following section. Subsequently, thermal response of the all-optical TO phase shifter will be simulated utilizing COMSOL Multiphysics to analyze the light-to-heat conversion by the light absorption from the metal layer. We will then discuss the determination of the parameters of the metal layer used in our proposed device.

2.2 Thermo-optic effect

In this section, a theoretical description of TO effect in silicon will be introduced. Using the methods of calculation and simulation, we will then explain properties of

silicon TO phase shifter, including a comparation between conventional type and all-optical type, and silicon TO switch, including MRR-based TO switch and MZI-based TO switch. Moreover, we will analyze the TO effect with a metal layer embedded in the device compared with non-linear optical effect because a high-intensity pump light will be induced to the device in our research.

2.2.1 Thermo-optic effect in silicon

TO effect consists of the variation of the refractive index of a dielectric material, due to a temperature variation of the material itself [1]. TO effect is present in all materials and is described by the TO coefficient, given by $\partial n/\partial T$, where n is the refractive index of the material at temperature T and thus, we have

$$\Delta n_{\text{eff}} = \frac{\partial n_{\text{eff}}}{\partial T}\Delta T\ , \tag{2.1}$$

where n_{eff} donates the effective refractive index of waveguide and ΔT denotes the change of temperature.

The modification of the refractive index in silicon is due to the changes in the distribution functions of carriers and phonons, and the temperature-induced shrinkage of the bandgap [4]. G. Cocorullo et al. [5] analyzed the TO coefficient of crystalline silicon in the C-band among the temperature range 300–600 K, given by

$$\frac{\partial n}{\partial T} = 9.48\times10^{-5} + 3.47\times10^{-7}\times T - 1.49\times10^{-10}\times T^2\ (K^{-1})\ . \tag{2.2}$$

It is more common to consider the TO coefficient of silicon near 300 K at the wavelength around 1550 nm, whose value can be expressed as [6]

$$\frac{\partial n}{\partial T} = 1.86\times10^{-4}\ K^{-1}\ . \tag{2.3}$$

We can also simulate the temperature dependence of silicon strip waveguide utilizing Lumerical MODE solutions, as shown in Fig. 2-1. It indicates that the effective index increased linearly as the temperature increased, with a slope of $2.04\times10^{-4}\ K^{-1}$, which can be comparable with Eq. (2.3).

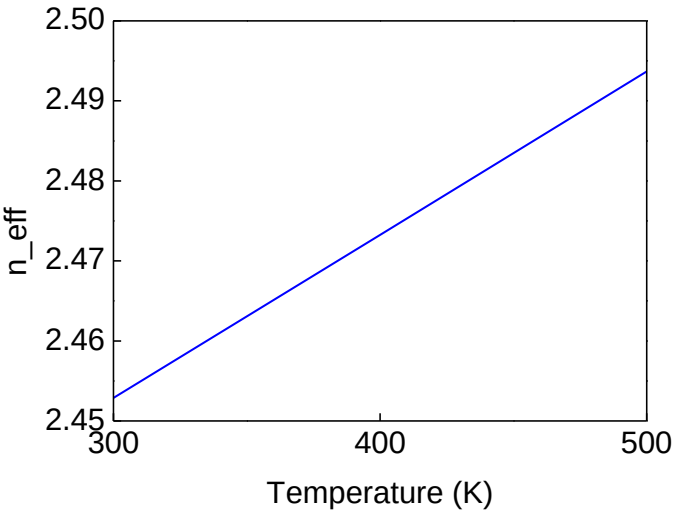

Fig. 2-1 Simulated effective index of silicon waveguide versus temperature.

2.2.2 Silicon thermo-optic phase shifter and thermo-optic switch

A TO phase shifter is basically composed of a waveguide structure and a heater. On the SOI platform, the waveguide structure can be a strip or rib silicon waveguide and the heater can be various types of materials owing to functional integration and CMOS-compatible fabrication of silicon photonics. We consider the resistive heater in the conventional TO phase shifter at first. Generally, the amount of phase shift caused by the resistive heater can be expressed as [2]

$$\Delta\varphi = \frac{2\pi}{\lambda}\left(\frac{\partial n_{\text{eff}}}{\partial T}\right)\Delta T \cdot L\,, \tag{2.4}$$

where λ is the wavelength of the light, $\left(\frac{\partial n_{\text{eff}}}{\partial T}\right)$ is the thermo-optic coefficient of the silicon waveguide, L is the length of the conventional TO phase shifter, and ΔT denotes the change of temperature. Since ΔT is caused by the action of the resistive heater, it can be written as

$$\Delta T = \frac{\eta P}{C_P \rho L S}, \tag{2.5}$$

where η is the utilization tuning efficiency of applied power, P is the power consumed by the resistive heater, C_P is the heat capacity of the waveguide, ρ is the density of the

silicon waveguide, and S is the cross-sectional area of the waveguide. Hence, from Eqs. (2.4) and (2.5) $\Delta\varphi$ can be written as

$$\Delta\varphi = \frac{2\pi}{\lambda}\left(\frac{\partial n_{\text{eff}}}{\partial T}\right)\frac{\eta P}{C_P \rho S}. \tag{2.6}$$

The tuning efficiency of the conventional TO phase shifter is usually expressed in terms of electrical power needed for a π phase shift (P_π), which can be expressed as

$$P_\pi = \frac{\lambda}{2}\left(\frac{\partial T}{\partial n_{\text{eff}}}\right)\frac{C_P \rho S}{\eta}. \tag{2.7}$$

Therefore, the tuning efficiency of the conventional TO phase shifter is mainly determined by the utilization tuning efficiency of applied power. An effective way to improve the tuning efficiency of the TO phase shifter is reducing heat leakage to the environment. In addition to tuning efficiency, the thermal time constant is also an important factor for the TO phase shifter. The thermal time constant of the conventional TO phase shifter can be written as

$$\tau = \frac{H}{G}, \tag{2.8}$$

where H is the heat capacity of the heated waveguide, and G denotes the thermal conductance of the waveguide to the environment. H and G can be expressed as

$$\begin{cases} H = C_P \rho L A \\ G = {P_\pi}/{\Delta T_\pi} \end{cases}. \tag{2.9}$$

Here, A is the area of heat flow. By substituting Eqs. (2.5) and (2.9) into Eq. (2.8), the thermal time constant can be rewritten as

$$\tau = \frac{\eta A}{S}. \tag{2.10}$$

Therefore, the thermal time constant is influenced by the utilization tuning efficiency by the applied power, the area perpendicular to the direction of heat flow, and the cross-sectional area of the waveguide. Moreover, the product of thermal time constant and power consumption, i.e., the figure of merit (FOM), can be expressed as

$$FOM = P_\pi \cdot \tau = \frac{\lambda C_P \rho A}{2}\left(\frac{\partial T}{\partial n_{\text{eff}}}\right), \tag{2.11}$$

which can be reduced by decreasing the area perpendicular to the direction of heat flow.

In addition, conventional TO phase shifters with folded and multi-pass waveguide have been proposed to reduce power consumption. However, this type of structure would increase the size of the footprint and insertion loss of the device.

On the other hand, for all-optical TO switch, the tuning efficiency is usually not constant for the whole TO phase shifter with a length of L. Hence, $\Delta T \cdot L$ in Eq. (2.4) should be reconsidered. The phase shift $\Delta\varphi$ of an all-optical TO phase shifter can be written as

$$\Delta\varphi = \frac{2\pi}{\lambda}\left(\frac{\partial n_{\text{eff}}}{\partial T}\right)\int_0^L \Delta T \, \mathrm{d}L \,, \tag{2.12}$$

where ΔT is the change of temperature at the center of wide waveguide per distance $\mathrm{d}L$ along light propagating direction. The principle of the all-optical TO switch may not satisfy all the equations related to conventional TO switch. However, we can make a similar analysis for the all-optical TO switch utilizing the combination of simulation and theoretical calculation.

As mentioned in Section 1.4, we have described the switching process of a TO switch based on microring resonator (MRR) or Mach-Zehnder interferometer (MZI). In order to analyze the TO phase shift of the TO switch, we simulated the silicon TO switch utilizing Lumerical INTERCONNECT solutions.

For an MRR-based TO switch, a switching can be implemented by applying a temperature change inside the microring. Usually, a small phase shift of the MRR can yield a large switching ratio for the switch owing to Lorentzian line-shape [7] of its transmission spectra. Nevertheless, if we have to observe a π phase shift of an MRR, a high temperature needs to be applied to a small-size microring, e.g., if $\Delta T = 775\ K$ was supplied to a 5-μm-long TO phase shifter inside the microring in the simulation as the on-state, a π phase shift transmission spectra at the drop port can be characterized as shown in Fig. 2-2.

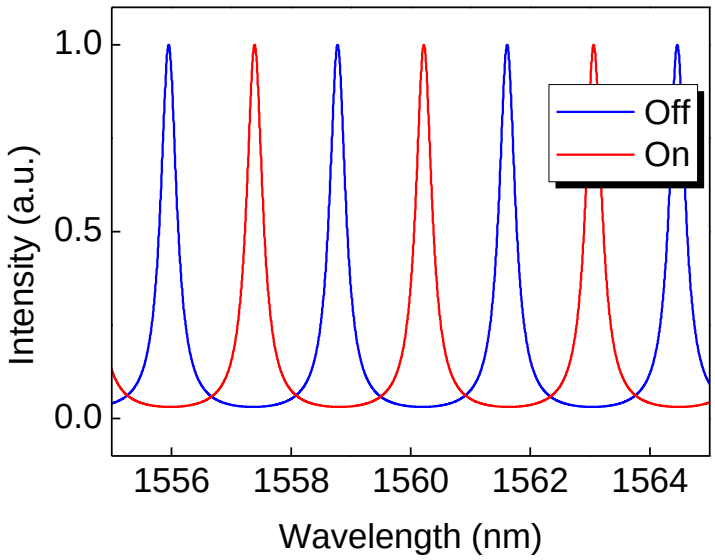

Fig. 2-2 Simulated transmission spectra of an add-drop MRR-based TO switch at drop port.

For an MZI-based TO switch, a switching can be implemented by applying a temperature difference between its arms. Figure 2-3 shows the simulated transmission spectra of an MZI-based TO switch, whose delay line was set to be 40 μm between its two arms. The off-state meant there was no temperature change in the simulated device, i.e., $\Delta T = 0$, while the on-state transmission spectra denotes a temperature difference was applied to the simulated device, here, $\Delta T = 193.5\ K$ was set for 20-μm-long TO phase shifter to obtain a π phase shift.

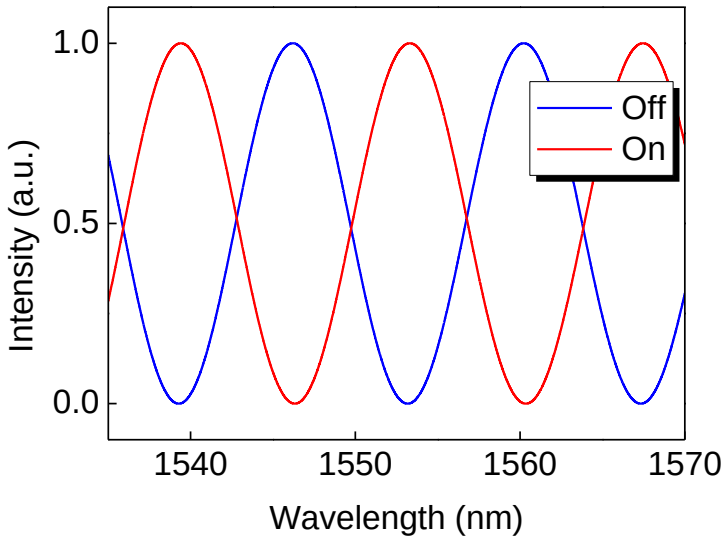

Fig. 2-3 Simulated transmission spectra of an MZI-based TO switch.

2.2.3 Thermo-optic effect with a metal layer compared with non-linear effect

A metal layer, assumed as titanium (Ti) in this research, which is supposed to be fabricated above the silicon waveguide with a short distance between them across a silica cladding layer, can be proved to dominate the heat conduction with TO effect rather than non-linear effects that occur together from the following discussion while taking an MRR-based switch as an example structure.

Firstly, the linear and non-linear absorption that cause the change of temperature can be given by

$$\Delta T = R_{th}(\alpha_{Linear} + \alpha_{TPA} + \alpha_{FCA})P_{inside} \tag{2.13}$$

while R_{th}, α_{Linear}, α_{TPA}, α_{FCA} and P_{inside} donate resistance of waveguide, linear absorption rate, two-photon absorption (TPA) rate, free-carrier absorption (FCA) rate and power inside the MRR, respectively. It should be noted that ΔT is temperature increase per unit length and the equation is hold only when the device length is shorter than an effective length L_{eff}. In Eq. (2.13), α_{TPA} and α_{FCA} is given by [8,9]

$$\alpha_{TPA} = \beta \frac{P_{inside}}{A_{eff}}, \tag{2.14}$$

and

$$\alpha_{FCA} = \sigma N = \frac{\sigma \tau \beta}{2h\nu} \left(\frac{P_{inside}}{A_{eff}} \right)^2, \tag{2.15}$$

respectively.

In Eqs. (2.13) and (2.14), the parameters can be expressed in the following Table 2-1.

Table 2-1. Parameters used in calculation.

Parameter	Value
FCA cross section σ	$1.45 \times 10^{-21}\ m^2$[10]
Carrier lifetime τ	$10\ ns$
TPA coefficient β	$8 \times 10^{-12}\ m \cdot W^{-1}$ [8]
Planck constant h	$6.63 \times 10^{-34} J \cdot s$
Frequency ν	$c \cdot \lambda^{-1}$ $(\lambda = 1.55 \mu m)$
Effective modal area A_{eff}	$0.429 \times 10^{-12}\ m^2$ [11]
Thermal resistance R_{th} (Si)	$1.97 \times 10^3\ K \cdot W^{-1}$ [11]
Thermal resistance R_{th} (Ti-to Si)	$42.8 \times 10^3\ K \cdot W^{-1}$ [11]
Group refractive index n_g for TM-mode	3.67
Thermo-Optic Coefficient $\partial n / \partial T$	$1.86 \times 10^{-4}\ K^{-1}$ [6]
Linear absorption by waveguide	$2\ dB \cdot cm^{-1}$ [11]

Hence, taking Eqs. (2.13), (2.14) and (2.15) into consideration, Eq. (2.1) can be rearranged as

$$\Delta n_{TO} = \frac{\partial n}{\partial T} R_{th} (\alpha_{Linear} + \alpha_{TPA} + \alpha_{FCA}) P_{inside}, \tag{2.16}$$

from which the change of refractive index due to TO effect can be calculated in the case that without or with a metal layer.

On the other hand, the change of refractive index in MRR is also affected by non-linear optical effects including free-carrier dispersion (FCD) and Kerr effect basically, which can be calculated by [8,12]

$$\Delta n_{FCD} = -[8.8 \times 10^{-4} N_e + 8.5 \times (N_h)^{0.8}] \times 10^{-18}, \quad (2.17)$$

and

$$\Delta n_{Kerr} = n_2 \frac{P_{inside}}{A_{eff}}, \quad (2.18)$$

respectively.

In Eq. (2.17), N_e and N_h denote the density of electron and hole, respectively. While in Eq. (2.18), $n_2 = 4.4 \times 10^{-8}\, m^2 \cdot W^{-1}$ [8] represents second-order nonlinear refractive index.

Consequently, the calculation results of the whole changes of refractive index in MRR are shown in Fig. 2-4 as follows, in which TO-FCA, TO-TPA, TO-Linear and TO-Linear Ti stand for the change of refractive index causing by TO effect duo to absorption by FCA, absorption by TPA, linear absorption and linear absorption of Ti, respectively.

(a)

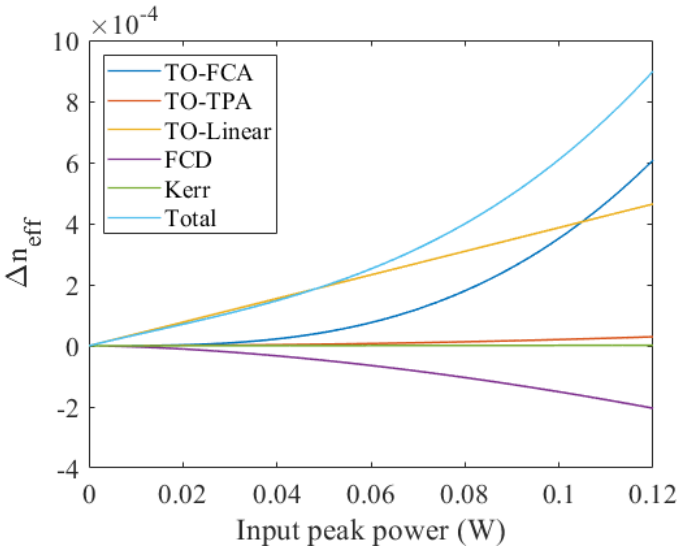

(b)

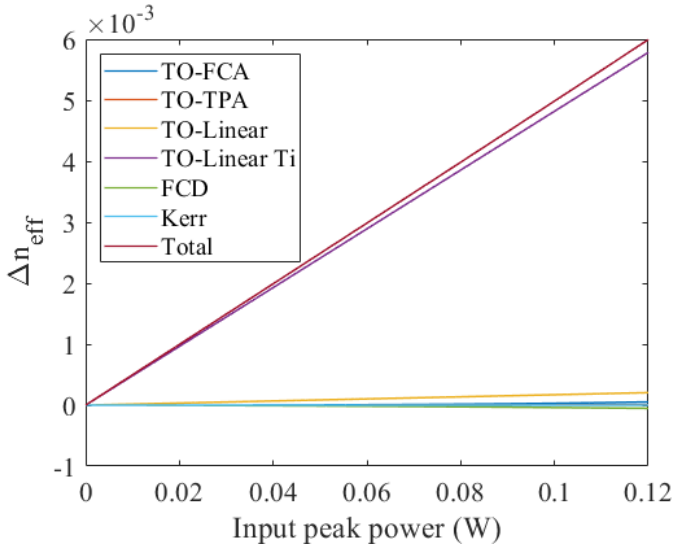

Fig. 2-4 Reflection index change of the MRR without Ti (a) and with Ti (b).

Therefore, Fig. 2-4(a) and (b) indicate that when a metal layer was embedded, when the input peak power was at the range from several tens of mW to a few hundreds of mW, TO effect dominated the change of refractive index rather than non-linear optical effects and also the change is ten-times larger than the structure without any metal.

Moreover, by taking these results into Eq. (2.19) as shown below, the change of wavelength due to the TO effect can be calculated.

$$\Delta\lambda = \lambda_0 \frac{\Delta n_{eff}}{n_g}, \tag{2.19}$$

where λ_0 denotes central wavelength and n_g denotes group refractive index. As a result, the change of wavelength while depositing a metal layer is over ten-fold compared with the change of wavelength of an MRR without this metal layer. It can be indicated that for an all-optical switch embedded with a metal layer, TO effect makes it performs an over ten-fold tuning efficiency with the same high-intensity power compared to non-linear effect.

2.3 Light-to-heat conversion

As we know, the modification of the refractive index in silicon can be caused by temperature change and usually is changed by heating. Therefore, we are going to investigate such heat induced by the light-to-heat conversion from the metal above the silicon waveguide with a short distance in this section. Considering of the light absorption by the metal, which is Ti in our research, that performs a high optical absorption and effective thermal resistance, we have made the simulations as follows.

2.3.1 In the condition of a single waveguide

The model used to simulate the thermal response of a TO phase shifter, which was comprised of a silicon waveguide, a Ti layer and the background material as silicon dioxide, was constructed by an Infinite Element Domain boundary fixed at room temperature as well as the components of the TO phase shifter, utilizing COMSOL Multiphysics. The thermal properties of the materials are listed in Table 2-2. Ti used in this simulation has the complex refractive index of 4.04+3.82i at the wavelength of 1550 nm. The external temperature was set as 293.15 K. We assumed that silicon waveguide was a normal 450 nm × 220 nm strip waveguide, the metal Ti was 4-μm-wide and 20-nm-thick and the distance between silicon waveguide and Ti was 170 nm. The TO phase shifter was set to be 5-μm-long. A three-dimension (3-D) structure of the simulation model is shown as Fig. 2-5(a).

According to guide books of COMSOL Multiphysics [13,14], the Electromagnetic Heating multiphysics coupling, used in this simulation, added the electromagnetic surface losses from the electromagnetic waves on the boundary as a heat source in the heat transfer part of the model, and the electromagnetic material properties could depend on the temperature. Therefore, we firstly simulated the boundary mode profile of the fundamental TM mode injected to the silicon waveguide (as shown in Fig. 2-5(b)) and then, performed the simulation of Frequency Domain and Frequency Transient. The temperature distribution results of the model can be extracted at a certain simulation time.

(a)

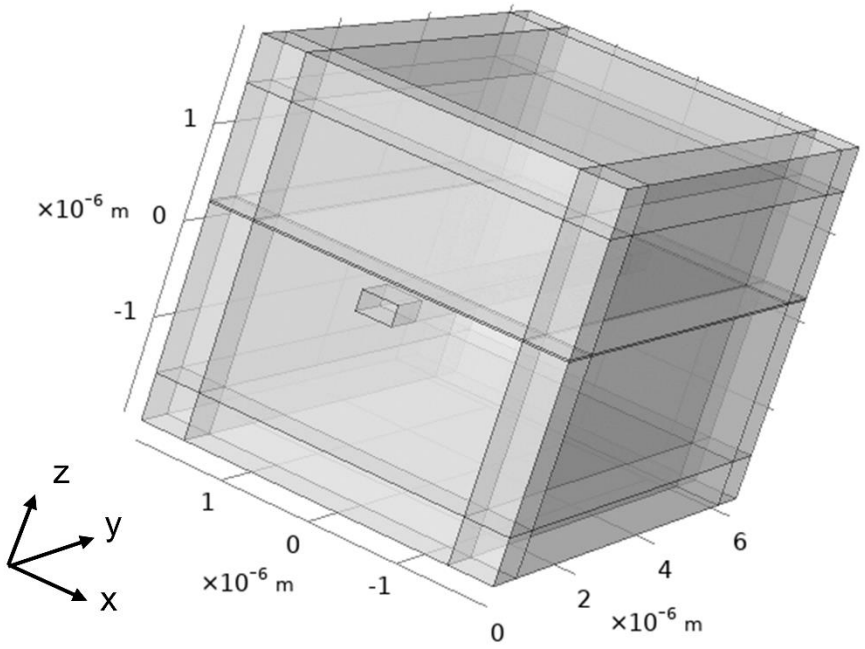

(b)

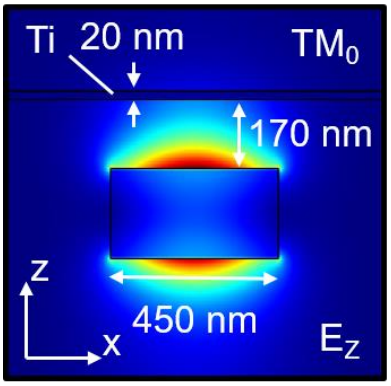

Fig. 2-5 (a) 3-D structure of the simulation model for a single waveguide with a Ti layer above. (b) Mode profile of fundamental TM mode for a single waveguide with a Ti layer above.

Table 2-2. Thermal properties of materials in the thermal simulation.

Material	Density (kg/m^3)	Specific heat [J/(kg·K)]	Thermal conductivity [W/(m·K)]
Titanium [15]	4510	523	9.6
Silicon [16]	2329	700	130

Silica [17]	2203	703	1.38

In this simulation, a TM-mode-polarized light was injected to the TO phase shifter with a power of 5 mW. The two-dimension (2-D) cross-section z-x plane at position y = 2.5 μm and x-y plane at position z = 0 temperature distributions of the TO phase shifter are shown in Figs. 2-6(a) and (b), respectively. In addition, the one-dimension (1-D) cross-section temperature change different from room temperature at position x = 0 and z = 0 is shown as Fig. 2-7, which can be used to calculate the increasing temperature of this TO phase shifter. Therefore, $\int_0^L \Delta T \, \mathrm{d}L$ of this TO phase shifter can be calculated to be 1050.9 K · μm with a total length of 5 μm and when a TM-polarized pump light with a power of 5 mW was injected to this 5-μm-long TO phase shifter, from Eq. (2.12) the phase shift $\Delta\varphi$ was calculated to be 0.252 π, which infers a theoretical tuning efficiency of 0.0101 π · μm^{-1} · mW^{-1}.

(a)

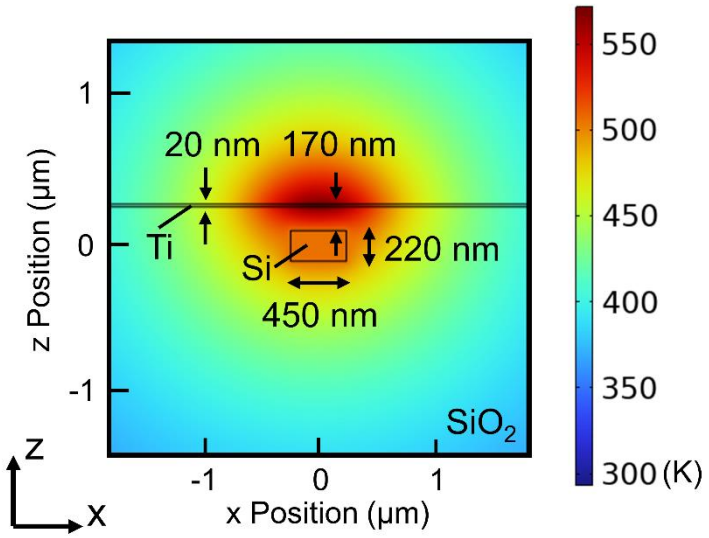

(b)

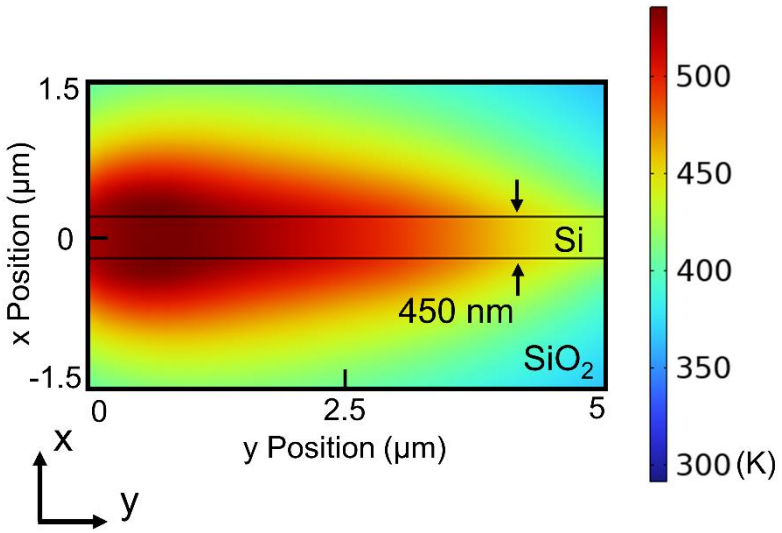

Fig. 2-6 Temperature distribution of the core silicon waveguide with a Ti layer above at the cross-section (a) z-x plane and (b) x-y plane.

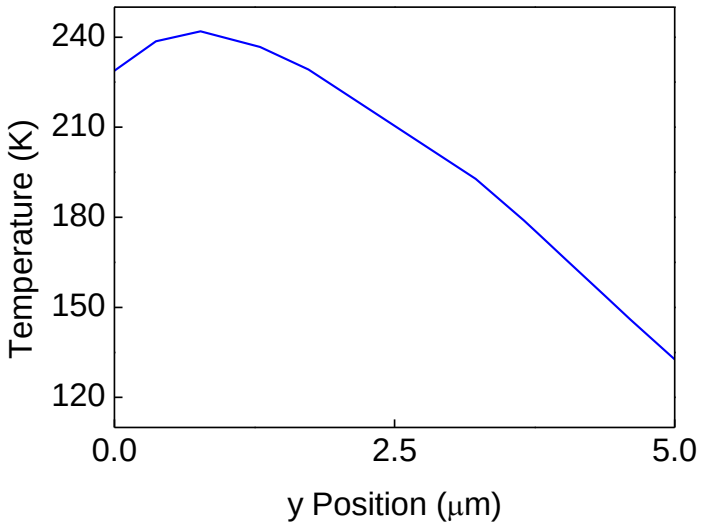

Fig. 2-7 1-D cross-section temperature change at position x = 0 and z = 0.

2.3.2 In the condition of two adjacent waveguides

Similar to the model described in previous section, we have also considered the TO phase shifter with two adjacent waveguides and the thermal response in the case that one of the adjacent waveguides is applied the TM-mode-polarized light. If the distance between two adjacent waveguides is close enough, it can be expected that the light-induced heat is adequate to cause a phase shift inside the TO phase shifter. For the simulation model, we assumed there were two 220-nm-thick adjacent silicon waveguides with a gap of 200 nm between them. A narrow waveguide was assumed to be 350-nm-wide for the TM-mode-polarized light input while the wide waveguide was assumed to be 750-nm-wide. The distance between waveguides and the Ti layer was set to be 230 nm and the Ti was set to be 6-μm-wide and 20-nm-thick. This TO phase shifter was set to be 10-μm-long to estimate the tuning efficiency of the TO phase shifter in an MZI-based TO switch. A 3-D structure of this simulation model is shown as Fig. 2-8(a). Also, we started from simulating the boundary mode profile of the fundamental TM mode injected to the narrow silicon waveguide (as shown in Fig. 2-8(b)) and then, performed the simulation of Frequency Domain and Frequency Transient. The temperature distribution results of this model can be extracted at a certain simulation time.

(a)

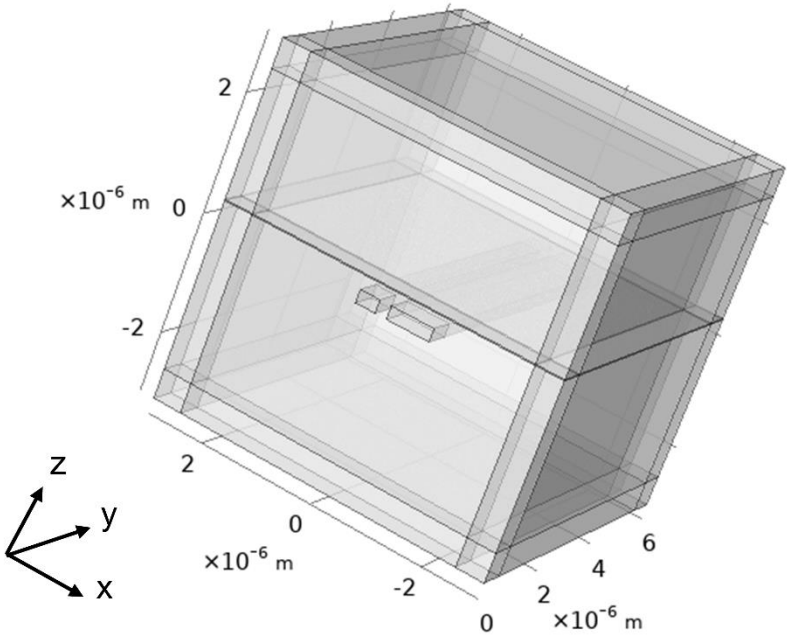

(b)

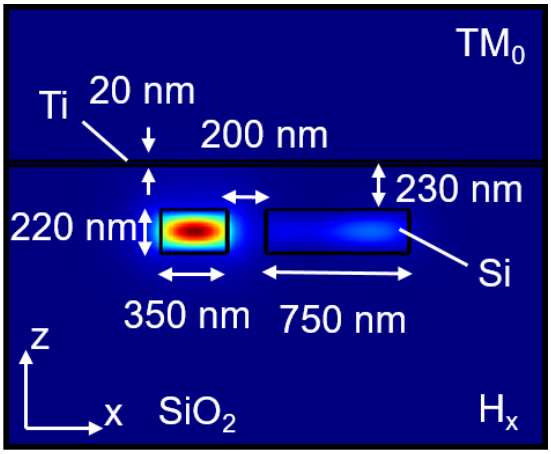

Fig. 2-8 (a) 3-D structure of the simulation model for two adjacent waveguides with a Ti layer above. (b) Mode profile of fundamental TM mode in a narrow waveguide for two adjacent waveguides with a Ti layer above.

In this simulation, a TM-mode-polarized light was injected to the narrow waveguide of the TO phase shifter with a power of 5 mW. The 2-D cross-section z-x plane and x-y plane temperature distributions of the TO phase shifter are shown in Figs. 2-9(a) and (b), respectively. In addition, the 1-D cross-section temperature change different from room temperature at position x = - 4.75 μm and z = 0 is shown as Fig. 2-10, which can be used

to calculate the increasing temperature of this TO phase shifter. Therefore, $\int_0^L \Delta T \, \mathrm{d}L$ of this TO phase shifter can be calculated to be 1364.7 K · μm with a total length of 10 μm and when a TM-polarized pump light with a power of 5 mW was injected to this 10-μm-long TO phase shifter, from Eq. (2.12) the phase shift $\Delta\varphi$ was calculated to be 0.328 π, which infers a theoretical tuning efficiency of 0.0066 π · μm^{-1} · mW^{-1}.

(a)

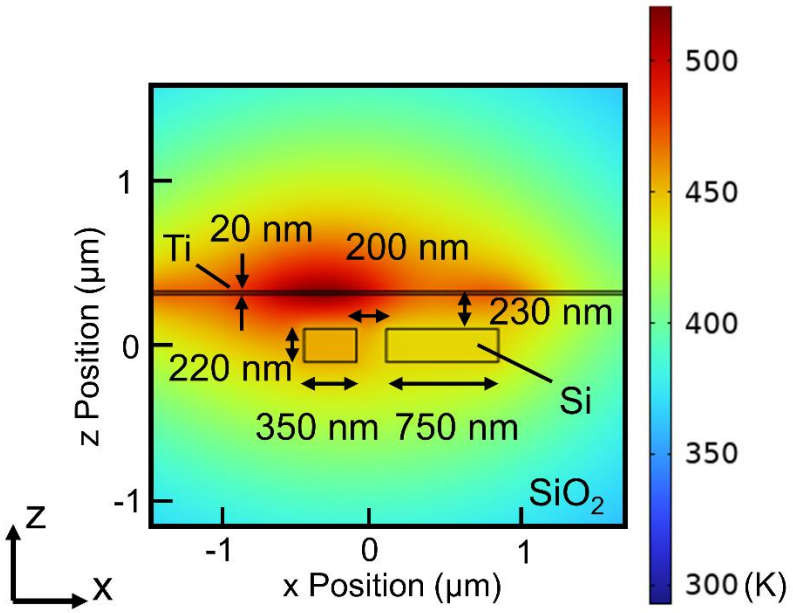

(b)

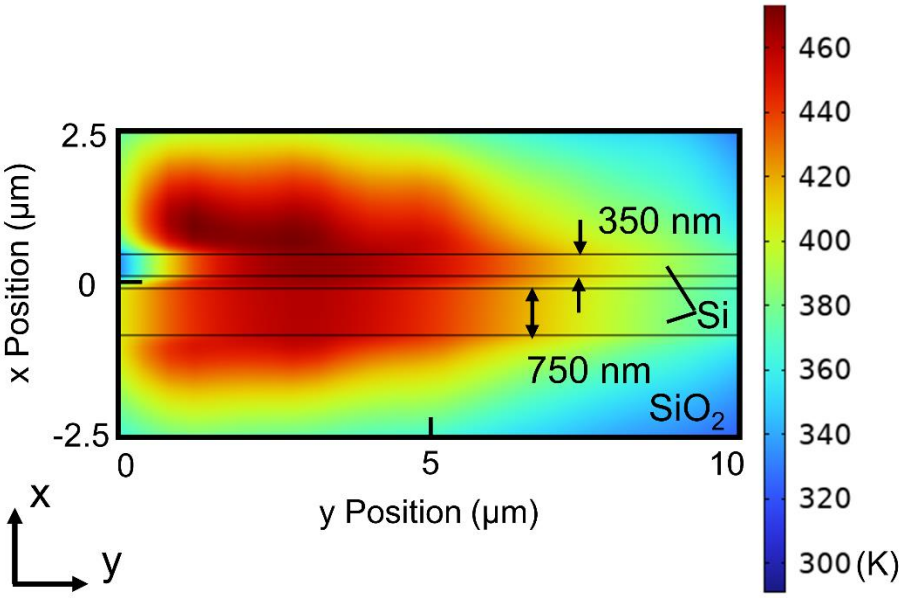

Fig. 2-9 Temperature distribution of the core silicon waveguides with a Ti layer above at the cross-section (a) z-x plane and (b) x-y plane.

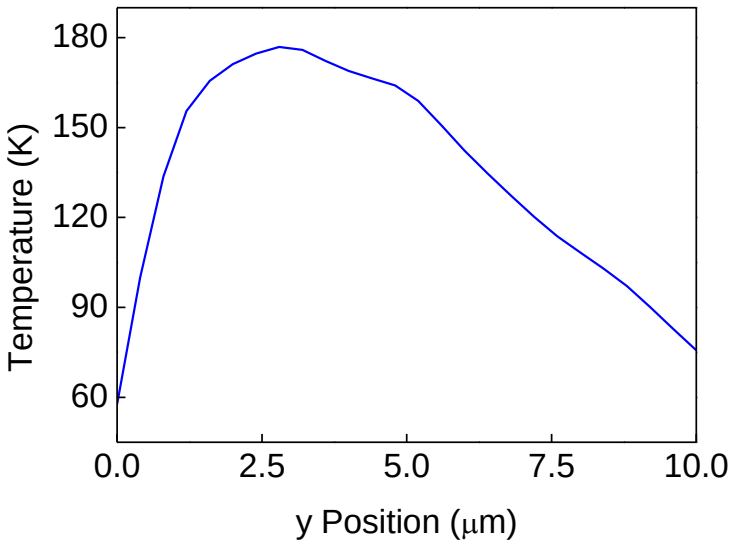

Fig. 2-10 1-D cross-section temperature change at position x = - 4.75 μm and z = 0.

2.4 Metal layer used in thermo-optic phase shifter

In Section 2.2.3, the significance of the metal layer used in the all-optical TO switch has been discussed. On the other hand, the light-to-heat conversion from the metal heater has been confirmed from the simulation discussed in Section 2.3. Thus, in order to design a high-performance all-optical TO switch utilizing the metal heater, we will characterize and analyze the properties of the Ti layer which is supposed to be deposited above the silicon waveguide as the heater in this section.

2.4.1 Thickness and length of titanium layer

We analyzed the relationship between light absorption loss in the silicon waveguide by the Ti layer and the thickness or length of this layer. The structure of the simulation model was composed of a 450 nm × 220 nm silicon strip waveguide, a Ti layer and surrounded material as silicon dioxide. The refractive index of materials used in the simulation were $n_{Si} = 3.48$, $n_{SiO_2} = 1.444$, and $n_{Ti} = 4.04 + 3.82i$. The length was assumed to be 20-μm-long at the simulation of differing the thickness of Ti layer, while the thickness was set to be 20-nm-thick at the simulation of differing the length of Ti layer. Figures 2-11(a) and (b) show the variation of light absorption rate for TM mode and absorption loss for TE mode under different thickness and length of Ti layer, respectively. It indicates from the simulation results that the thickness of the Ti could not affect the light absorption loss too much so that 20 nm could be considerable for a small-volume all-optical TO switch. The length of the Ti layer is also an important parameter for the design. From Fig. 2-11(b) we can observed the increasing light absorption rate for TM mode as well as the loss for TE mode when we increased the length of Ti layer. Since we require more light-induced heat from the absorption of TM mode from the metal while we demand the device to perform a low insertion loss of TE mode, it reveals a trade-off relationship between the heat tuning and insertion loss of the device towards the length of the Ti layer.

(a)

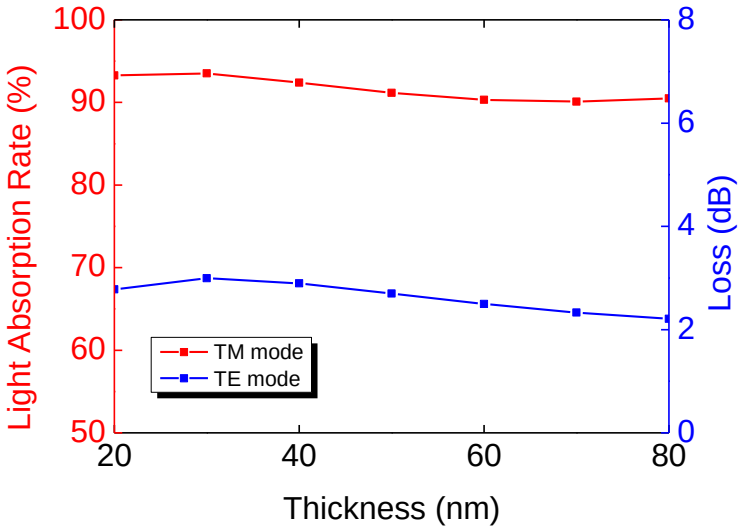

(b)

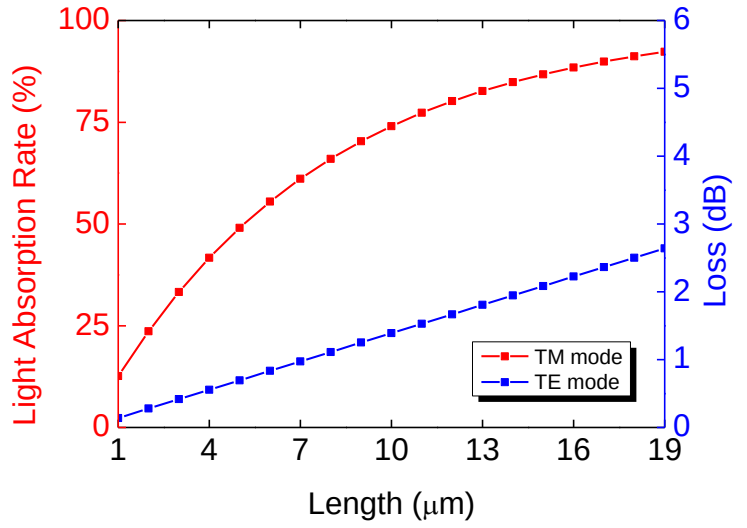

Fig. 2-11 Variation of light absorption rate for TM mode and absorption loss for TE mode under different (a) thickness of Ti layer and (b) length of Ti layer.

2.4.2 Distance between titanium layer and silicon waveguide

Next, for the design of distance between Ti layer and silicon waveguide, we also performed the simulation to analyze the relationship between light absorption loss for

TM/TE mode and this distance. Note that, this distance corresponds to the thickness of a silicon dioxide cladding layer between silicon waveguide and the deposited Ti layer. Figures 2-12 shows the variation of light absorption rate for TM mode and absorption loss for TE mode under different distance between silicon waveguide and Ti layer. The Ti layer used for the simulation was assumed to be 20-μm-long and 20-nm-thick. Similar to the parameter of the length of the Ti layer, the simulated result reveals a trade-off relationship between the heat tuning and insertion loss of the device towards the distance between silicon waveguide and Ti layer. However, taking in account the thermal conductance between Ti layer and silicon waveguide, this distance should not be designed as too long because the light-induced heat conducted from the Ti layer has a trend of random diffusion and the TM-mode-polarized light can be hardly absorbed by the Ti layer. On the other hand, this distance should not be designed as too small, which should cause a reflection loss at the boundary as well as a high insertion loss of the TE-mode-polarized input signal light. Consequently, we consider to design the distance between silicon waveguide and the Ti layer in the range from 170 nm to 330 nm.

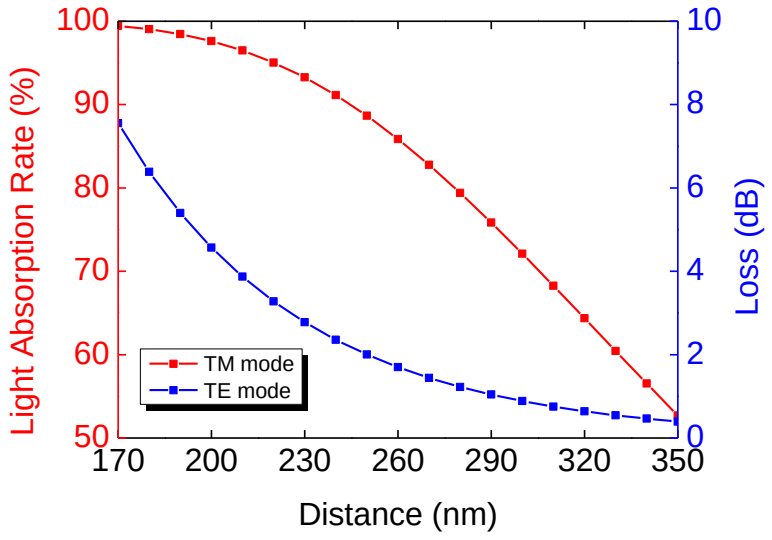

Fig. 2-12 Variation of light absorption rate for TM mode and absorption loss for TE mode under different distance between silicon waveguide and Ti layer.

2.4.3 Arrayed patterns of titanium layer

The switching time is also an important factor to value the performance of the device. Generally, the TO switches have response times of microsecond-scale to millisecond-scale. From Eq. (2.10) we have known that for the conventional TO phase shifter it is influenced by the utilization tuning efficiency by the applied power as well as the heat flow area and the cross-sectional area of the waveguide. Considering the switching time of the all-optical TO phase shifter (or switch), it can be inferred that the switching time is mainly influenced by the properties of the heating material, which is Ti in our research, as well as the position and the pattern of the metal heater. However, switching time of the all-optical TO switch can hardly be simulated accurately because of nonuniform heat source due to pump light. We measured the switching time of several fabricated device through preliminary experiments. For the measurement, the pump light was emitted from a tunable diode laser (TLD) with a wavelength of 1550 nm and then modulated by a pulse pattern generator and an electro-optic modulator into a pulse signal with the frequency of 25 kHz and a duty cycle of 10%. The pump light was then amplified by an erbium doped fiber amplifier to a peak power of around 50 mW and polarized into TM mode through a polarization controller. The signal light was emitted from a TLD with a wavelength of 1560 nm and propagated as a continuous-wave after being polarized into TE mode through a polarization controller. Then, both of the pump light and the signal light were injected to the fabricated device. The output signal lights were detected by an avalanche photodiode after going through the band-pass filter, and then characterized by an oscilloscope. Figure 2-13(a) shows the temporal responses of the output signal lights of a device deposited a 15-μm-long normal-pattern Ti layer as well as a device deposited a 15-μm-long arrayed-pattern Ti layer. This arrayed-pattern Ti layer consisted of three 5-μm-long normal-pattern Ti layers with an internal of 5-μm between the first and second Ti pad as well as an internal of 5-μm between the second and third Ti pad. The 10%–90% rising time and the 90%–10% falling time of the device with normal-pattern Ti layers were measured to be 1.61 μs and 12.61 μs, respectively. Whereas for the device with arrayed-pattern Ti layers, they were measured to be 1.17 μs and 3.72 μs, respectively. It indicates that the all-optical TO switch with arrayed-pattern Ti layers performed a

faster switching time, especially for the 90%–10% cooling time. We presume the reason as follows. The heat generated by the pump light is mainly located at the input side and then spread in the metal plane. The heat is spread in the vertical and lateral directions in the case of the normal pattern while only in the vertical direction in the case of arrayed pattern, as shown in Fig. 2-13(b). Therefore, the heat remains on the silicon waveguide for longer time in the case of normal pattern.

(a)

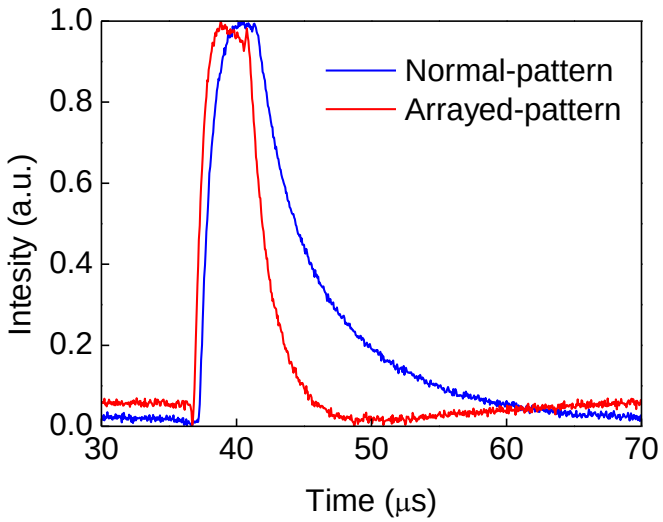

(b)

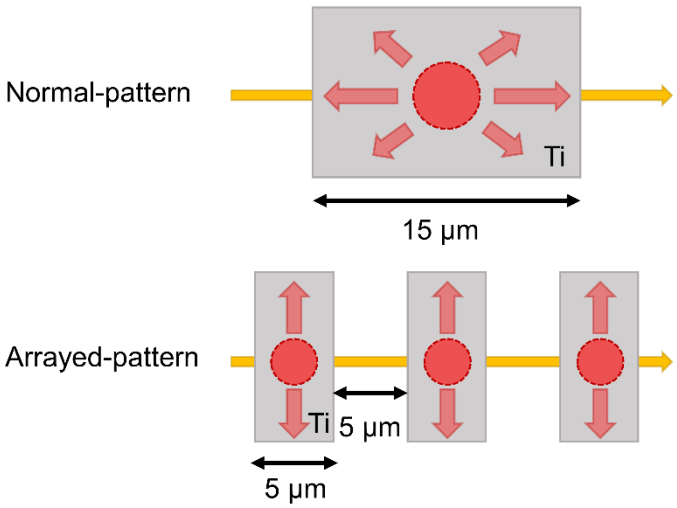

Fig. 2-13 (a) Normalized temporal response of all-optical TO switch with a normal-pattern Ti and an arrayed-pattern Ti layer. (b) Schematic for heat diffusion in normal-

pattern and arrayed-pattern metal heater.

2.5 Summary

Thermo-optic effect in silicon can be used efficiently by embedding a metal layer above silicon waveguide with a short distance between them, and the metal is supposed to be Ti in this research. When a high-intensity pump light is induced to an all-optical TO phase shifter with a metal layer, from the simulation of thermal response, temperature increase can be implemented by the light-to-heat conversion effectively. Moreover, this temperature increase is dominated by TO effect rather than non-linear optical effect through the analysis in Section 2.2.3, resulting in the change of refractive index of the silicon waveguide. An all-optical TO switch can be designed based on this heating process and can be optimized by designing the metal layer properly.

References

1. G. Coppola, L. Sirleto, I. Rendina, M. Iodice, “Advance in thermo-optical switches: principles, materials, design, and device structure,” Opt. Eng. 50(7), 071112 (2011).
2. S. Liu, J. Feng, Y. Tian, H. Zhao, L. Jin, B. Ouyang, J. Zhu and J Guo, “Thermo-optic phase shifters based on silicon-on-insulator platform: state-of-the-art and a review,” Frontiers of Optoelectronics 15(1), 9 (2022).
3. S. Chung, M. Nakai, H. Hashemi, “Low-power thermo-optic silicon modulator for large-scale photonic integrated systems,” Opt. Express 27(9), 13430–13459 (2019).
4. L. Pavesi and G. Gérard, “Optical interconnects,” Springer series in optical sciences 119 (2006).
5. G. Cocorullo, F. G. Della Corte, and I. Rendina, “Temperature dependence of the thermo-optic coefficient in crystalline silicon between room temperature and 550 K at the wavelength of 1523 nm,” Appl. Phys. Lett.74(22), 3338–3340 (1999).
6. I. Rendina, “Thermo-optical modulation at 1.5m in silicon etalon,” Electron. Lett. 28(1), 83–85(2) (1992).
7. W. Bogaerts, P. De Heyn, T. Van Vaerenbergh, K. De Vos, S. Kumar Selvaraja, T. Claes, P. Dumon, P. Bienstman, D. Van Thourhout, R. Baets, “Silicon microring resonators,” Laser & Photon. Rev. 6(1), 47-73 (2012).
8. M. Dinu, F. Quochi, and H. Garcia, “Third-order nonlinearities in silicon at telecom wavelengths,” Appl. Phys. Lett. 82(18), 2954–2956 (2003).
9. R. A. Soref and B. R. Bennett, “Electrooptical effects in silicon,” IEEE J. Quantum Electron. 23(1), pp. 123–129 (1987).
10. A. Cutolo, M. Iodice, P. Spirito, and L. Zeni, “Silicon electro-optic modulator based on a three terminal device integrated in a low-loss single-mode SOI waveguide,” IEEE J. Light. Technol. 15(3), 505–518 (1997).
11. 村井 俊哉, “シリコンリング共振器を用いた 導波路型光メモリに関する研究,” 東京工業大学 大学院理工学研究科, (2018).
12. T. K. Liang and H. K. Tsang, “Role of free carriers from two-photon absorption in Raman amplification in silicon-on-insulator waveguides,” Appl. Phys. Lett., vol. 84, no. 15, pp. 2745–2747, 2004.
13. COMSOL, “Wave Optics Module User’s Guide,” Version: COMSOL 5.3,

https://doc.comsol.com/5.3/doc/com.comsol.help.woptics/WaveOpticsModuleUsersGuide.pdf

14. COMSOL, “COMSOL Multiphysics Reference Manual,” Version: COMSOL 6.2, https://doc.comsol.com/6.2/doc/com.comsol.help.comsol/COMSOL_ReferenceManual.pdf
15. J. Shim, J. Lim, D.-M. Geum, B. H. Kim, S.-Y. Ahn, and S. Kim, “Tailoring bolometric properties of a TiOx/Ti/TiOx tri-layer film for integrated optical gas sensors,” Opt. Express 29, 18037-18058 (2021).
16. W. Liu, and M. Asheghi, “Thermal Conductivity Measurements of Ultra-Thin Single Crystal Silicon Layers,” ASME. J. Heat Transfer. 128(1), 75–83 (2006).
17. L. Ren, K. Pashayi, H. R. Fard, S. P. Kotha, T. Borca-Tasciuc and R. Ozisik, “Engineering the coefficient of thermal expansion and thermal conductivity of polymers filled with high aspect ratio silica nanofibers,” Composites Part B: Engineering 58, 228-234 (2004).

Chapter 3

Remotely controllable microring resonator-based thermo-optic switch

3.1 Introduction

In this chapter, we will design and optimize the performance of the all-optical remotely controllable microring resonator (MRR)-based TO switch to verify the efficient tuning by the TM-mode-polarized pump light to control switching operation of the TE-mode-polarized signal light. An all-optical switching process is implemented by inducing the pump light as MRR configuration allows efficient heating at a small volume utilizing TO effect within looped cavity. The structure of MRR will be designed for TE-mode-polarized input probe signal in order to reduce the absorption loss by the metal layer embedded above the microring silicon waveguide across a middle silicon dioxide layer. In a previous study [1], TM mode light was used for both the probe and pump signals and suffered from high absorption by the metal of the probe signals in TM mode polarization, thus leading to a relatively low quality factor (Q-factor) performance by the MRR. Thus, its switching ratio is not well while using a peak input power of ~20 mW. Therefore, we will use TE mode probe signal to ensure a higher Q-factor of the MRR which can be expected to achieve low insertion loss and high extinction ratio [2] that contributes to the improvement of the switching ratio of the proposed MRR-based TO switch at burst switching operation. Moreover, the proposed device is supposed to keep a relatively fast switching times owing to compact modulation area.

Herein, we will show the operation principle and structural parameters design of the proposed MRR-based TO switch in detail. The measured characterization of the

proposed device will be discussed as well.

3.2 Operation principle

In this section, properties of a microring resonator will be introduced especially the add-drop microring resonator, which can be used for multiple outputs as the future design of our proposed device. The operation principle of the proposed remotely controllable microring resonator-based TO switch will also be analyzed.

3.2.1 Microring resonator

A microring resonator (MRR) generally consists of a looped optical waveguide and a coupling mechanism to access the loop [2]. Figure 3-1 shows the structures of the all-pass MRR as well as the add-drop MRR. The all-pass MRR consists of a bus waveguide and a ring coupled to the waveguide, as shown in Fig. 3-1(a), while the add-drop MRR consists of two waveguides and a ring coupled to them, as shown in Fig. 3-1(b). For the add-drop MRR, if multiple rings are coupled to an input bus waveguide and each ring is coupled to a different output waveguide, the incident field can be partly transmitted to multiple drop ports, which can realize a multiple output operation. Before discussing our device, we will analyze the transmission properties of the add-drop MRR in the following.

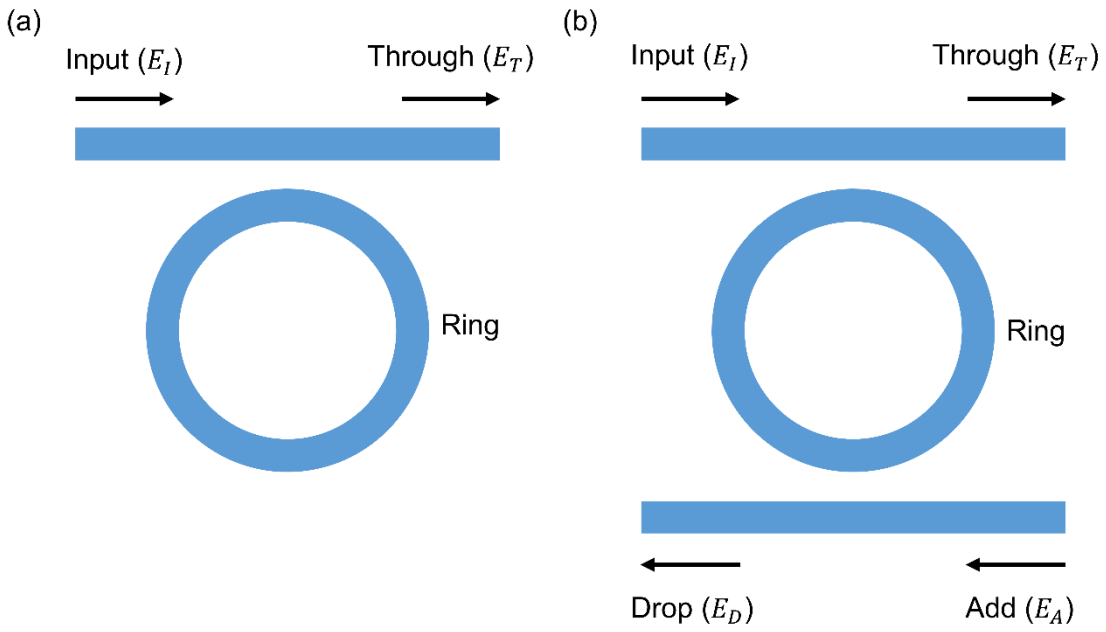

Fig. 3-1 (a) Structure of an all-pass microring resonator. (b) Structure of an add-drop microring resonator.

Figure 3-2(a) shows the schematic of an add-drop MRR. To analyze this structure, we divide this MRR into two subcomponents, which are the coupling region and the round-trip region. The coupling region magnifies one of the bus waveguide and part of the microring while the round-trip region describes the schematics of the microring. The quantities given by E_I, E_T, E_A and E_D are complex transfer functions representing the fields of lights at input port, through port, add port and drop port as indicated in Fig. 3-2(a), respectively.

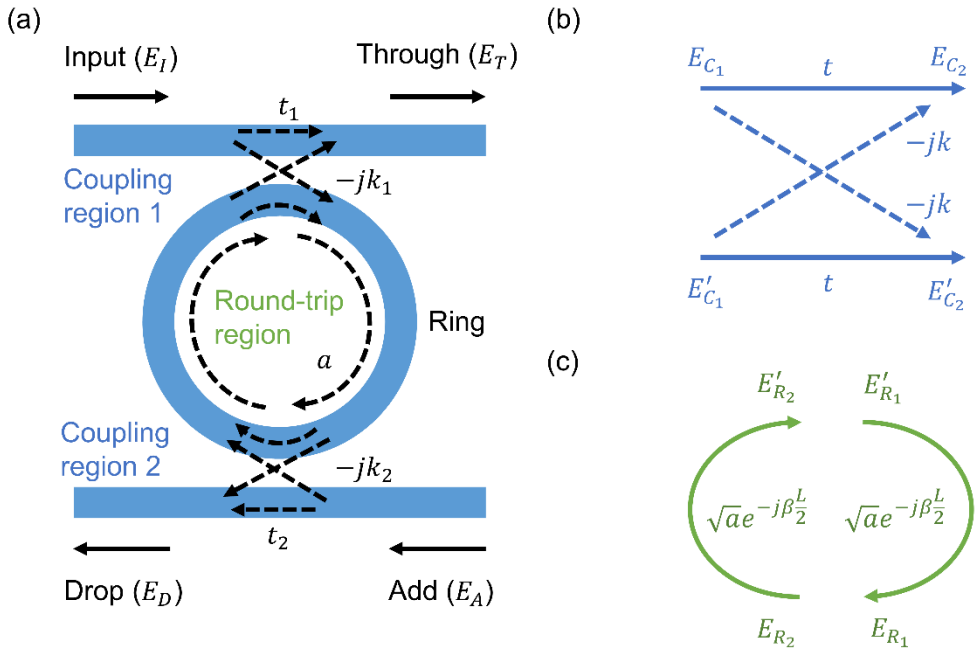

Fig. 3-2 (a) Schematic of an add-drop microring resonator. (b) Schematic of the magnified coupling region. (c) Schematic of the round-trip region.

Firstly, for the coupling region as shown in Fig. 3-2(b), the relationship between the fields of E_{C_1}, E'_{C_1}, E_{C_2} and E'_{C_2} is given by

$$\begin{pmatrix} E'_{C_2} \\ E_{C_2} \end{pmatrix} = [T] \begin{pmatrix} E'_{C_1} \\ E_{C_1} \end{pmatrix}, \tag{3.1}$$

where

$$T = \begin{pmatrix} t & -jk \\ -jk & t \end{pmatrix}, \tag{3.2}$$

also t and k are self-coupling coefficient and cross-coupling coefficient between the straight waveguide and the microring, respectively. It can be noted that t^2 and k^2 correspond to the power splitting ratios of the coupler, and when the coupling loss is assumed as negligibly small, they satisfy

$$t^2 + k^2 = 1 . \tag{3.3}$$

Hence, from Eq. (3.1) and Eq. (3.2) the relationship between the fields of E_{C_1}, E'_{C_1}, E_{C_2} and E'_{C_2} can be expressed by

$$\begin{pmatrix} E'_{C_1} \\ E'_{C_2} \end{pmatrix} = [C] \begin{pmatrix} E_{C_1} \\ E_{C_2} \end{pmatrix}, \tag{3.4}$$

where

$$C = \frac{j}{k} \begin{pmatrix} -t & 1 \\ -1 & t \end{pmatrix}. \tag{3.5}$$

Secondly, for the round-trip region as shown in Fig. 3-2(c), the quantities given by E_{R_1}, E'_{R_1}, E_{R_2} and E'_{R_2} are complex transfer functions within the ring such that R'_1 and R'_2 are mirror points of R_1 and R_2, respectively. Meanwhile we define L, β and α as the quantities of the round-trip path length, propagation constant and power attenuation coefficient inside the ring, respectively.

The relationship between the quantities of E_{R_1}, E'_{R_1}, E_{R_2} and E'_{R_2} can be expressed by

$$E_{R_1} = \sqrt{a} e^{-j\beta \frac{L}{2}} E'_{R_1}, \tag{3.6}$$

and

$$E'_{R_2} = \sqrt{a} e^{-j\beta \frac{L}{2}} E_{R_2}. \tag{3.7}$$

where a satisfies the relation

$$a^2 = \exp(-\alpha L), \tag{3.8}$$

and a can be described as roundtrip transmission of the filed amplitude.

When defining a matrix $[R]$ as

$$R = \begin{pmatrix} \frac{1}{\sqrt{a}} e^{j\beta \frac{L}{2}} & 0 \\ 0 & \sqrt{a} e^{-j\beta \frac{L}{2}} \end{pmatrix}, \tag{3.9}$$

the relationship between E_{R_1}, E'_{R_1}, E_{R_2} and E'_{R_2} can be written as

$$\begin{pmatrix} E'_{R_1} \\ E'_{R_2} \end{pmatrix} = [R] \begin{pmatrix} E_{R_1} \\ E_{R_2} \end{pmatrix}, \tag{3.10}$$

Next is to combine the coupling region and the round-trip region of the MRR together. Let $[W]$ be a matrix such that

$$W = \begin{pmatrix} 0 & 1 \\ 1 & 0 \end{pmatrix}. \tag{3.11}$$

Subsequently, for an add-drop MRR, the relationship between the quantities of E_I, E_T,

E_A and E_D can be expressed by

$$\begin{pmatrix} E_D \\ E_A \end{pmatrix} = [W][C_2][W][R]\,[C_1]\begin{pmatrix} E_I \\ E_T \end{pmatrix}. \tag{3.12}$$

Hence, by taking $E_A = 0$ and using Eqs. (3.3), (3.5) and (3.9) to eliminate k_1 and k_2, the transmission of power to through port and drop port can be expressed by

$$\left|\frac{E_T}{E_I}\right|^2 = \frac{t_1^2 - 2at_1t_2cos(\varphi) + a^2t_2^2}{1 - 2at_1t_2cos(\varphi) + a^2t_1^2t_2^2}, \tag{3.13}$$

and

$$\left|\frac{E_D}{E_I}\right|^2 = \frac{a(1-t_1^2)(1-t_2^2)}{1 - 2at_1t_2cos(\varphi) + a^2t_1^2t_2^2}, \tag{3.14}$$

respectively, where $\varphi = \beta L$ represents the accumulated phase in the ring after a single roundtrip transmission.

When the MRR is under the condition of resonance, the accumulated phase φ in the MRR becomes a multiple of 2π and if m is an integer (m = 1, 2, 3…). We have

$$\varphi = 2m\pi\,. \tag{3.15}$$

Therefore, at resonance, Eq. (3.13) and (3.14) can be simplified into

$$\left|\frac{E_T}{E_I}\right|^2 = \frac{(t_1 - at_2)^2}{(1 - at_1t_2)^2}, \tag{3.16}$$

and

$$\left|\frac{E_D}{E_I}\right|^2 = \frac{a(1-t_1^2)(1-t_2^2)}{(1 - at_1t_2)^2}, \tag{3.17}$$

respectively.

If the attenuation is negligible ($a \approx 1$), critical coupling occurs at symmetric coupling ($k_1 = k_2$). For a lossy MRR ($a < 1$), critical coupling occurs when the losses match the coupling expressed as

$$t_1 = at_2\,. \tag{3.18}$$

Under the condition $a < 1$, if the add-drop MRR is symmetric and satisfies $k_1 = k_2 = k$ ($t_1 = t_2 = t$), Eq. (3.16) and (3.17) simplify to

$$\left|\frac{E_T}{E_I}\right|^2 = \frac{t^2(1-a)^2}{(1 - at^2)^2}, \tag{3.19}$$

and

$$\left|\frac{E_D}{E_I}\right|^2 = \frac{a(1-t^2)^2}{(1-at^2)^2}, \tag{3.20}$$

respectively.

Moreover, from Eqs. (3.13) and (3.14) we can derive the on-off extinction ratio as well as insertion loss of through port and drop port by considering the expressions as functions of φ, which can be given by

$$T_T(\varphi) = \left|\frac{E_T}{E_I}\right|^2 = \frac{t_1^2 - 2at_1t_2cos(\varphi) + a^2t_2^2}{1 - 2at_1t_2cos(\varphi) + a^2t_1^2t_2^2}, \tag{3.21}$$

and

$$T_D(\varphi) = \left|\frac{E_D}{E_I}\right|^2 = \frac{a(1-t_1^2)(1-t_2^2)}{1 - 2at_1t_2cos(\varphi) + a^2t_1^2t_2^2}. \tag{3.22}$$

Hence, the extinction ratio of through port (ER_t) and drop port (ER_d) can be expressed as

$$ER_t = \frac{T_T\left[\left(2m+\frac{1}{2}\right)\pi\right]}{T_T(2m\pi)} = \frac{(t_1+at_2)^2(1-at_1t_2)^2}{(1+at_1t_2)^2(t_1-at_2)^2}, \tag{3.23}$$

and

$$ER_d = \frac{T_D(2m\pi)}{T_D\left[\left(2m+\frac{1}{2}\right)\pi\right]} = \left(\frac{1+at_1t_2}{1-at_1t_2}\right)^2, \tag{3.24}$$

respectively.

Also, the insertion loss of through port (IL_t) and drop port (IL_d) can be expressed as

$$IL_t = T_T\left[\left(2m+\frac{1}{2}\right)\pi\right] = \frac{(t_1+at_2)^2}{(1+at_1t_2)^2}, \tag{3.25}$$

and

$$IL_d = T_D(2m\pi) = \frac{a(1-t_1^2)(1-t_2^2)}{(1-at_1t_2)^2}, \tag{3.26}$$

respectively.

3.2.2 Microring resonator-based thermo-optic switch

Figure 3-3(a) shows the three-dimensional structure of the proposed remotely

controllable MRR-based TO switch which is supposed to be fabricated on a silicon-on-isolator (SOI) platform. Initially a TE-mode-polarized probe signal is induced into the silicon waveguide propagating through the bus waveguide. Above the microring waveguide, which is surrounded by the material silicon dioxide, is the metal layer (Ti), represented by the red thin cuboid. This deposited metal layer is away from the silicon microring at a proper distance that can guarantee that the microring can be tuned by the heat that converted from the absorbed pump light from the metal efficiently. As shown in Fig. 3-3(b), when a high-intensity TM-mode-polarized pump light is induced with a wavelength different from the one of probe signal, due to the TO effect, the transmission spectra of the MRR will have a red shift, which can realize a signal switching of the output port. The switching operations of the through port and the drop port are implemented simultaneously. Note that, TO effect dominates the change of the refractive index of the microring rather than nonlinear optical effect while a high-intensity pump signal is induced according to the discussion in Chapter 2.3.

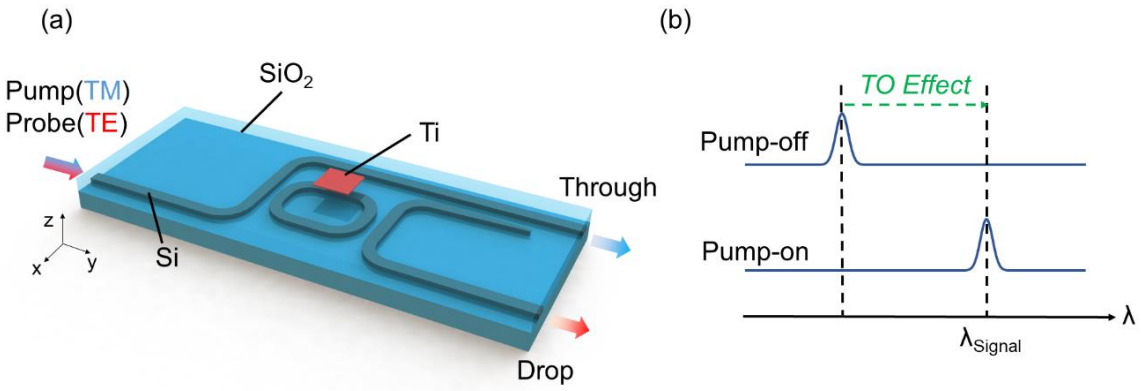

Fig. 3-3 (a) Schematic of the proposed MRR-based thermo-optic switch. (b) Illustration of the thermo-optic phase shift at the drop port of an MRR.

3.3 Device design and experiment

In this section, the design of the parameters of the MRR-based TO switch will be

investigated using the methods of simulation, calculation and experiments. At this point, there are two main kinds of parameters that need to be decided, which are the parameters used to design a TE-mode implemented add-drop MRR and the parameters related to the design of the metal layer.

3.3.1 Design of microring resonator-based thermo-optic switch

For the design of the TE-mode implemented add-drop MRR of the MRR-based TO switch, we would like it to perform a low insertion loss and a high extinction ratio. Considering the range of phase shift and sufficient space for designing the size of the metal layer at the microring, a bending radius of 20 μm and coupling length of 12 μm, were designed and a 25-μm-long straight waveguides were chosen to deposit the metal above. We used spot-size converters for our device, which can adiabatically convert the mode from the large mode in the single mode fiber down to the small mode of the silicon photonic edge coupler, and thus, enhance the edge coupling efficiency of the device [3]. The spot-size converter was a 100-μm-long tapered waveguide with the input width of 240 nm and output width of 500 nm [4].

It was necessary to distinguish the round-trip propagation loss of the microring which was mainly caused by the absorption of light due to the metal layer. Therefore, using software Lumerical MODE solutions, we simulated the mode profile of a silicon waveguide with a Ti layer above it across a certain distance while the surrounding material was silicon dioxide. The parameters of materials used in the simulation were $n_{Si} = 3.48$, $n_{SiO_2} = 1.444$, and $n_{Ti} = 4.04 + 3.82i$.The distance between silicon waveguide and Ti was assumed to be 170 nm and the thickness of Ti layer was set to be 20 nm. Simulated mode profiles of the fundamental TE-mode and TM-mode are shown in Figs. 3-4(a) and (b), respectively. Thus, we simulated the light absorption rate by the Ti for both TE and TM mode of the core silicon waveguide with a Ti layer above corresponding to different distances, as shown in Fig. 3-5. The light absorption of the pump signal polarized in the TM mode and the probe signal polarized in the TE mode were balanced owing to the metal. When the distance decreased, the light absorption in both fundamental modes increased, and the ratio of the TM mode to the TE mode

decreased. It indicates that when the distance was 170 nm, the differential light absorption rate between TE mode and TM mode was around maximum and approximately 78.2 % of the TM-mode-polarized pump light was absorbed by the metal (Ti) and converted to heat. For this condition, the loss for TM mode and TE mode was simulated by calculating the effective mode of the core waveguide. The results show that the loss for TM mode was 1.32 dB/μm, whereas that for the TE mode was 0.37 dB/μm. This observation implies that the light absorption by the metal in the TM mode was 3.5 times higher than that in the TE mode. Therefore, we selected the distance between silicon waveguide and Ti layer to be 170 nm.

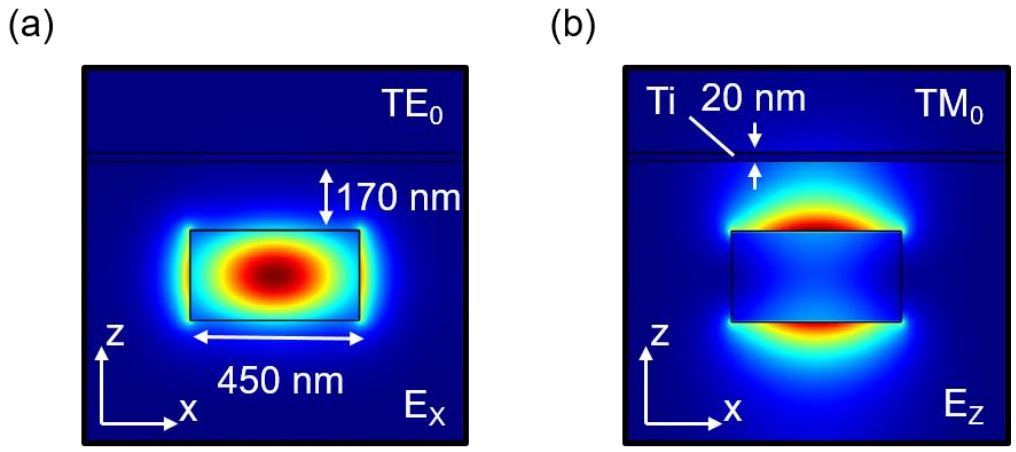

Fig. 3-4 Mode field distribution of silicon waveguide with a Ti layer above for (a) TE mode and (b) TM mode.

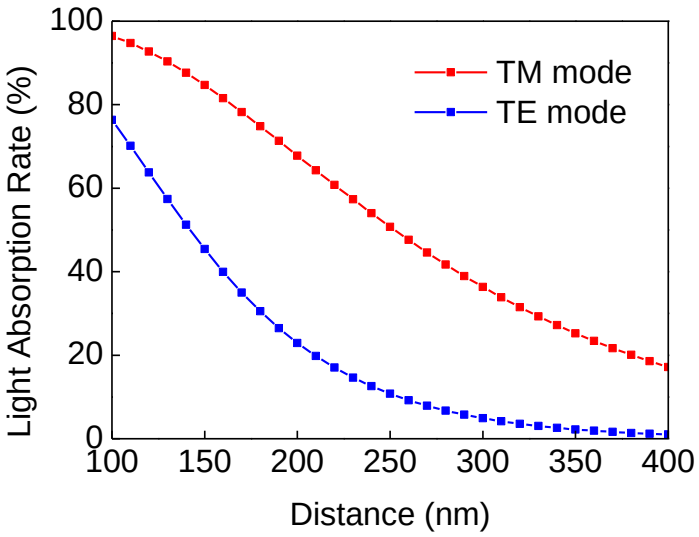

Fig. 3-5 Light absorption rate of the TM-mode and TE-mode as a function of distance between the silicon waveguide and the 5-μm-long metal layer.

For the length design of Ti layer along the light propagating direction, we fabricated actual device on a silicon-on-isolator (SOI) platform to calculate the round-trip propagation loss of the MRR. We fabricated MRRs with the same design excluding the length of Ti layer. The lengths of Ti layer were set to be 5, 10, and 15 μm of the fabricated device. As we measured the extinction ratio of each device, we calculated from Eqs. (3.23) and (3.24) and it resulted that the ring round-trip loss coefficient a equaled to 0.8, 0.65, and 0.5 corresponding to the lengths of Ti layer as 5, 10, and 15 μm, respectively. Parameter a is defined by Eq. (3.8), and $a = 1$ indicates lossless. To reduce the high absorption loss of the input signal due to the metal, a length of 5 μm was chosen, i.e., $a = 0.8$.

Under above conditions, we fabricated the add-drop MRRs with symmetric gaps between the bus waveguides at the through/drop port and the microring, ranging from 160 to 260 nm. The result is shown in Figs. 3-6(a) and (b), where the design gap corresponded to the remaining power through the bus waveguide after the coupling region. Figure 3-6(a) shows that for TE mode the extinction ratio (ER) of through port became smaller while drop port getting larger when the gap increased and Fig. 3-6(b) shows that for TE mode insertion loss (IL) of through port became lower because when

the gap became larger, the coupling between ring and bus waveguide would be weaker, thus, IL of the drop port became larger. Therefore, it indicates that 200 nm was the best choice to achieve a balanced ER and IL at both through and drop ports.

(a)

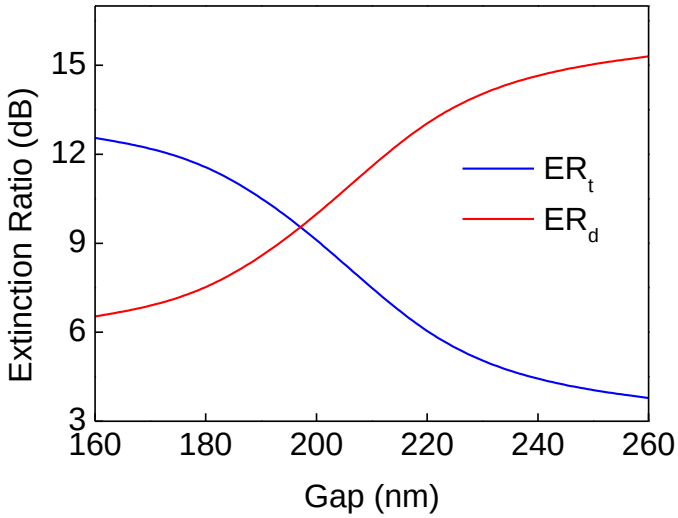

(b)

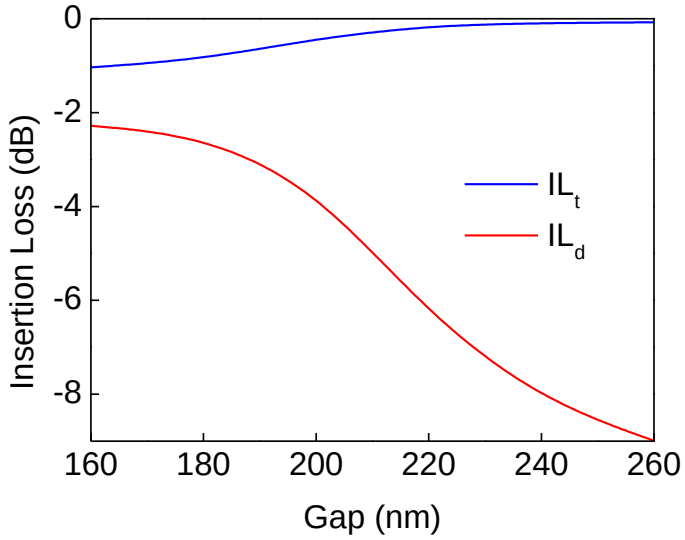

Fig. 3-6 (a) Relationships between extinction ratio (ER) and designed gap for symmetric-gap microring resonators of through (ER_t) and drop (ER_d) port. (b) Relationships between insertion loss (IL) and designed gap for symmetric-gap microring resonators of through (IL_t) and drop (IL_d) port.

However, according to the discussions above, we have only designed the most suitable parameters for the MRR-based TO switch with symmetric gaps between the microring and waveguides at the through/drop port. For add-drop MRR with asymmetric gaps, the ER distribution of both the drop port and the through port were simulated through Eqs. (3.23) and (3.24), as shown in Figs. 3-7(a) and (b), under the condition of $a = 0.8$. Here, we have defined $t_{through}$ as the self-coupling coefficient between the through port waveguide and the microring and t_{drop} as the self-coupling coefficient between the drop port waveguide and the microring. As shown in Fig. 3-2(a), the structure of asymmetric-gap ring resonators where the gap of the directional coupler on the through port side and the gap of the directional coupler on the drop port side can be designed separately, and $t_{through}$ & t_{drop} are used to signify the difference. It indicates that the drop port's ER exhibited a maximum value of 19.10 dB in an ideal condition where the self-coupling coefficient of both the through ($t_{through}$) and drop (t_{drop}) sides of the microring are equal to one. However, ensuring a low insertion loss when the asymmetric-gap MRR is in the critical coupling condition is challenging as it will have a high ER at the through port but less than 13.17 dB at the drop port. Therefore, an MRR with symmetric gaps of 200 nm was chosen for design of the MRR-based TO switch.

(a)

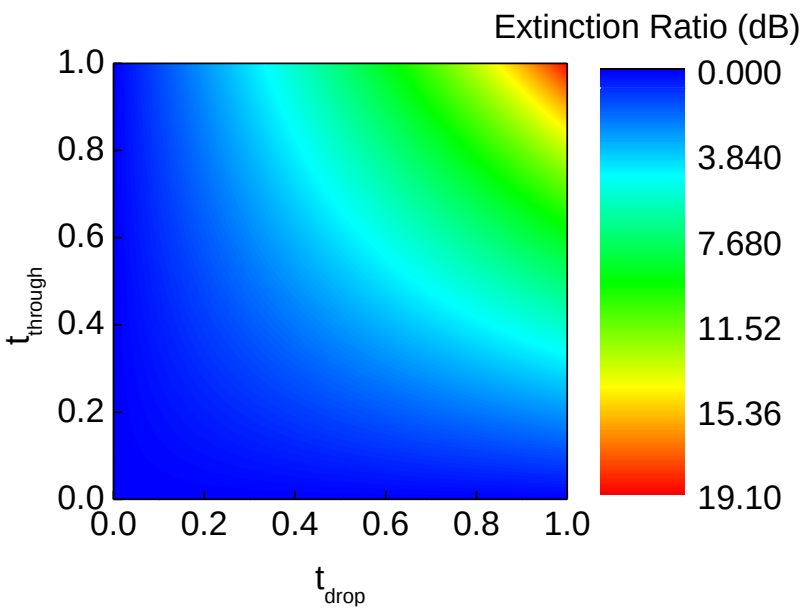

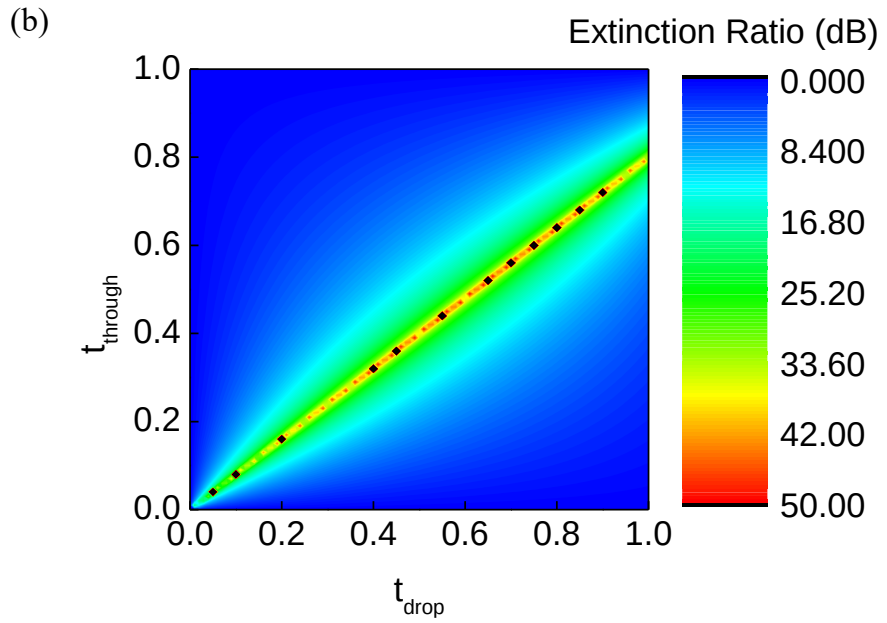

Fig. 3-7 Simulated extinction ratio of (a) through port and (b) drop port of the MRR with a round trip loss coefficient of $a = 0.8$.

3.3.2 Simulation and discussion

The temperature distribution in the region of the core silicon waveguide with the Ti layer above was simulated through COMSOL Multiphysics, and Infinite Element Domain fixed at room temperature was used as the boundary. The thermal properties of the materials are listed in Table 3-1. Ti used in this simulation has the complex refractive index of 4.04+3.82i at the designed wavelength of 1550 nm. The external temperature was set as 293.15 K. The mode profile of the fundamental TM mode used in this simulation was the same as Section 3.3.1, as shown in Fig. 3-4(a). The thermal simulation results are shown in Figs. 3-8(a) and (b), which show the temperature distribution around the core waveguide plane when the input power to the waveguide was set to 5 mW. Note that the input pump light was absorbed by Ti, the metal which covered all the simulation zone above waveguide in the z-direction, and the induced heat was conducted from the Ti to the waveguide. A distinct temperature rise along the waveguide was observed, and

the temperature shift was calculated to be approximately 150 K. Additionally, the effective index temperature sensitivity was calculated and found to be 0.000204 (1/K) using Lumerical MODE Solutions. Thus, the device was simulated using Lumerical INTERCONNECT to generate a π phase shift of the microring. The power efficiency of phase shift is calculated to be 0.0101 $\pi \cdot \mu m^{-1} \cdot mW^{-1}$ which is comparable with about a half of that in conventional electrically driven TO switches.

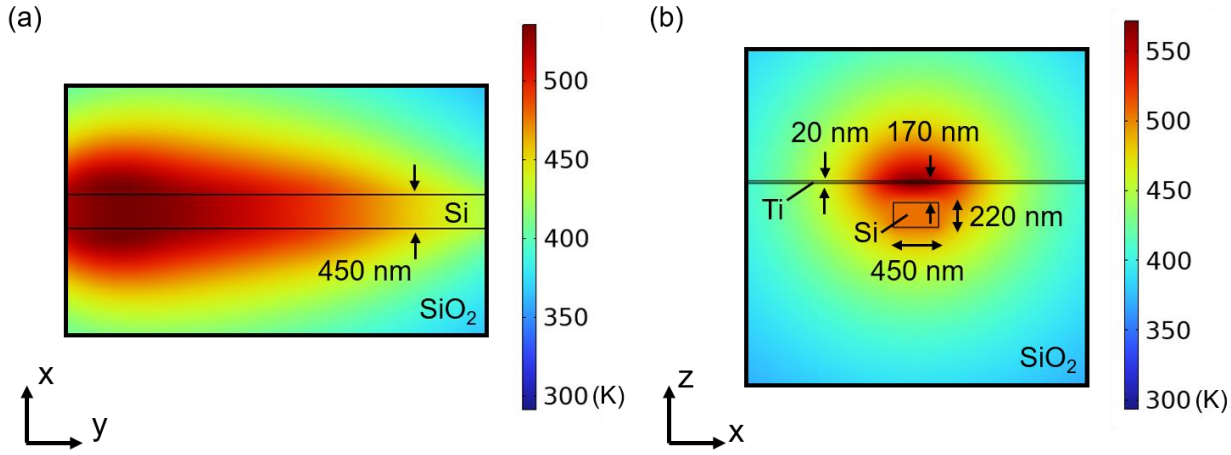

Fig. 3-8 Temperature distribution of the core silicon waveguide with a Ti layer above in the (a) x-y plane and (b) z-x plane.

Table 3-1. Thermal properties of materials in the thermal simulation.

Material	Density (kg/m^3)	Specific heat [J/(kg·K)]	Thermal conductivity [W/(m·K)]
Titanium [5]	4510	523	9.6
Silicon [6]	2329	700	130
Silica [7]	2203	703	1.38

3.3.3 Fabrication of the designed microring resonator-based thermo-optic switch

According to the discussions above, we fabricated the designed MRR-based TO switch on an SOI platform (see Appendix A2 for detailed fabrication flows). Firstly, we prepared an SOI wafer and used electron beam lithography and reactive ion etching to

generate the pattern of silicon waveguides. Subsequently, plasma-enhanced chemical vapor deposition (P-CVD) was used to deposit a 170-nm-thick silicon dioxide layer to determine the absorption of light by the metal layer, which was later deposited onto this middle silicon dioxide layer above the silicon microring waveguide. The 20-nm-thick Ti layer, whose pattern was generated by photolithography, was then deposited by electron-beam physical vapor deposition. Lastly, a 2-μm-thick layer of silicon dioxide was deposited via P-CVD as the overcladding. Figure 3-9(a) shows the microscopic image of the fabricated device which indicates the position of Ti that deposited above the microring as well as the size of the device. A cross-sectional scanning electron microscopy (SEM) image of the cross-sectional core waveguide with a Ti layer is shown in Fig. 3-9(b), and the parameters of the fabricated device were approximately the same as the ones of the designed structure. The transmission spectra of the fabricated device for the TE-mode-polarized light input are as shown in Fig. 3-10, indicating the extinction ratio of 9.1 dB and 9.5 dB at through port and drop port, respectively.

(a)

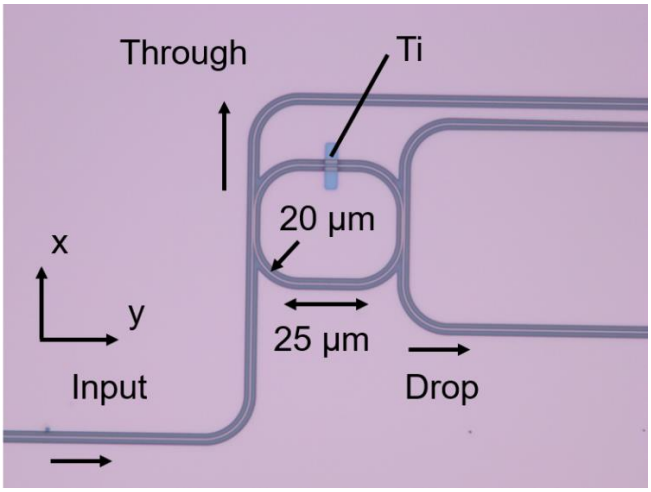

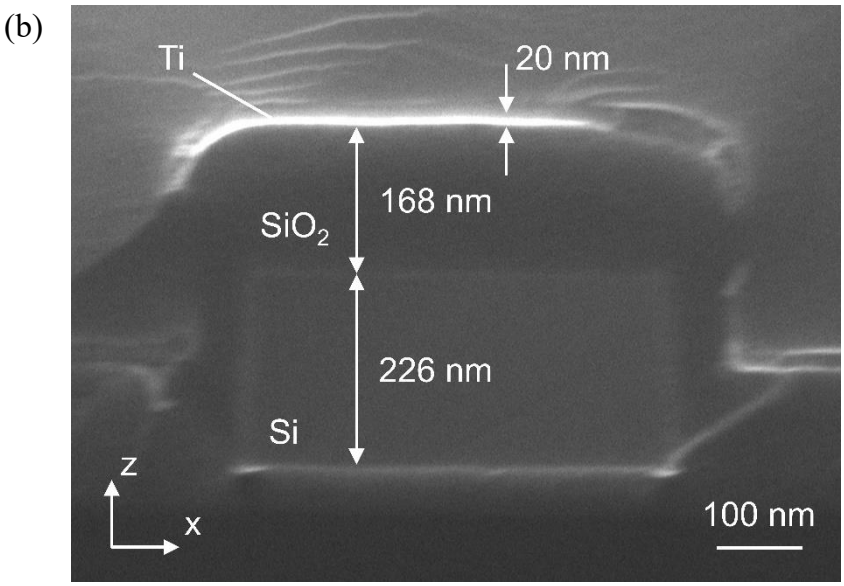

Fig. 3-9 (a) Microscopic image of the fabricated MRR-based thermo-optic switch. (b) SEM image of cross-sectional core waveguide with a Ti layer.

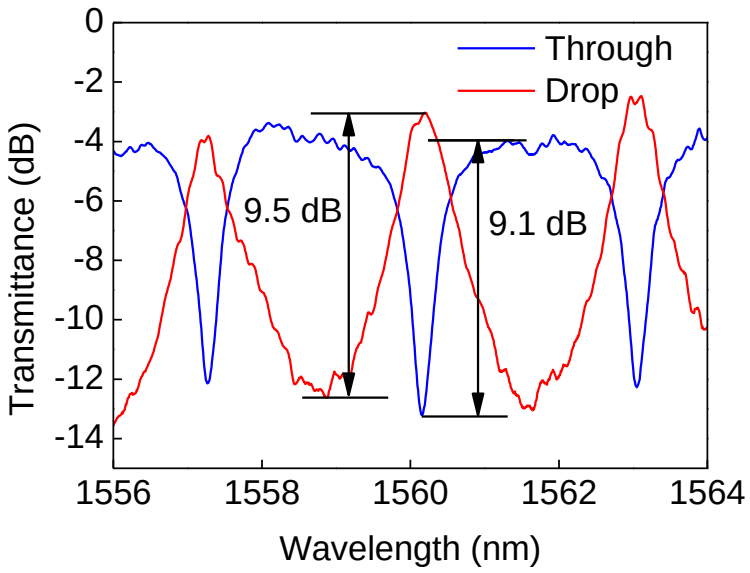

Fig. 3-10 Transmission spectra of the fabricated MRR-based thermo-optic switch.

3.4 Pump-probe measurement and device characterization

We have conducted pump-probe experiments using the pump/probe signal lights to measure the performances of our device, which are composed of temporal response measurement and burst switching measurement. Before exhibiting the characterization of device, the experimental setup will be introduced first.

Figure 3-11 shows the experimental setup for the pump-probe measurement. Probe signal light with a certain wavelength was emitted by the tunable laser diode (TLD). It propagated as a continuous-wave (CW) for the temporal response measurement while was modulated by a pulse pattern generator (PPG) and an electro-optic modulator into packets signal for the burst switching measurement. Then the probe signal was polarized into TE mode through the polarization controller (PC). On the other hand, pump signal light with a certain wavelength was emitted by the TLD and modulated by a PPG and an electro-optic modulator into pulse signal for the pump-probe experiments. Subsequently, pump signal was amplified by an erbium doped fiber amplifier (EDFA) to a certain optical power and polarized into TE mode through the PC. We used a 3-dB coupler to couple the probe and pump signal into device under test (DUT) or into the power meter through the attenuator to measure the average power. There was a matrix optical switch to switch the input signals to any of its outputs. The static characterization of the DUT was observed by the spectrum analyzer while the output signals of the pump-probe measurements were detected by an avalanche photodiode (APD) after going through the band-pass filter (BPF), and then characterized by an oscilloscope.

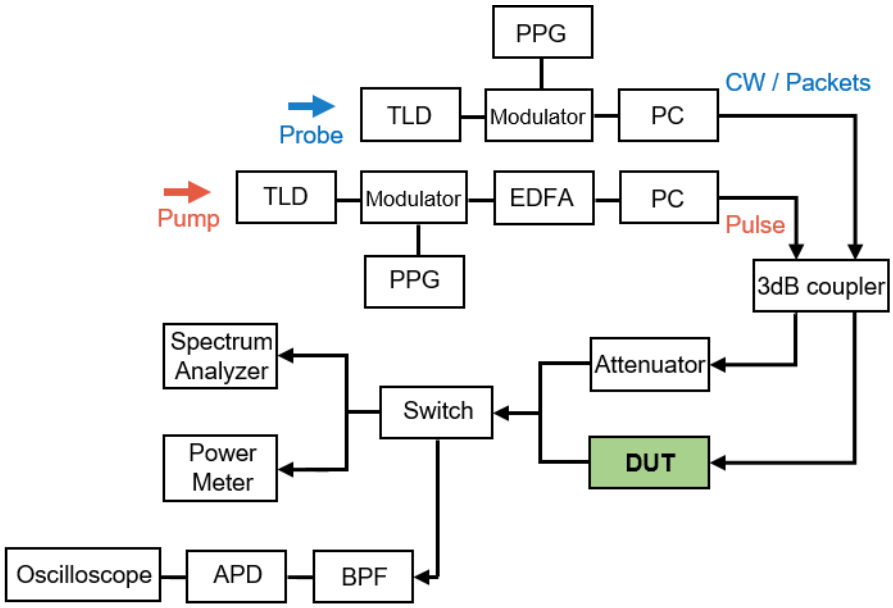

Fig. 3-11 Schematic of temporal response and burst switching measurement setup. (TLD: tunable laser diode, PPG: pulse pattern generator, EDFA: erbium doped fiber amplifier, PC: polarization controller, CW: continuous wave, DUT: device under test, BPF: band-pass filter, APD: avalanche photodiode)

3.4.1 Temporal response measurement

For the temporal response measurement, we used the CW probe signal with the wavelength of 1560.24 nm in the TE mode polarization and pulse pump signals with the wavelength of 1553.27 nm in the TM mode polarization. The pump light was amplified to a peak power of 16.8 mW by the EDFA with a period of 40 μs and 10% duty cycle modulated by a PPG and an electro-optic modulator. The CW probe signal and pulse pump signal were combined with a 3-dB coupler and the combined light was input into the DUT. The output probe signal light passed through a BPF, and it was subsequently detected by an APD and measured by an oscilloscope. As shown in Figs. 3-12(a)&(b), a switching can be observed while the pump signal was induced because the spectrum of the device had a red shift to the long wavelength side due to thermo-optic effect so that at the through port the optical power of the input signal increased while the optical power of the input signal at the drop port decreased. At a wavelength of 1560.24 nm, the on/off

switching ratio was measured to be 8.4 dB at the through port and 7.3 dB at the drop port. The 10%–90% rising time and the 90%–10% falling time were estimated to be 0.71 μs and 2.66 μs at the through port, respectively. Whereas at the drop port, they were estimated to be 1.44 μs and 4.33 μs, respectively. This difference could be due to the different sharpness in the spectra in the through and drop ports. Moreover, the modulation efficiency of this device can be calculated to be approximately 0.04 nm/mW from the transmission spectra and temporal response waveforms, which is the same as previous research. FSR of this device can be observed from Fig. 3-10, which was approximately 2.9 nm. Therefore, tuning efficiency of the proposed device can be calculated to be approximately 0.0276 $\pi \cdot mW^{-1}$. Since this device exhibited a better Q-factor, while adding a same power, the switching ratio can be expected to perform better than previous research [1].

(a)

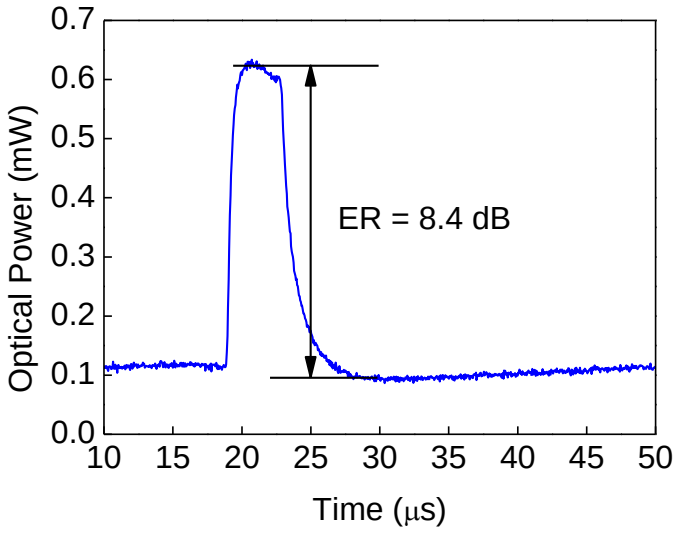

(b)

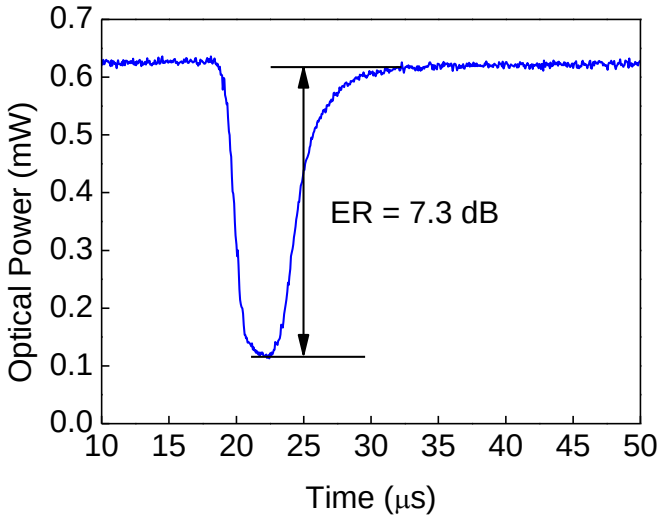

Fig. 3-12 Temporal response waveforms of the probe signal at the (a) through port and (b) drop port (λ= 1560.24 nm).

3.4.2 Burst switching measurement

For the burst switching measurement, we used a 10 Gb/s packets probe signal which was emitted by the TLD with a wavelength of 1560.24 nm, modulated by a PPG (MP1761C) and an electro-optic modulator and polarized into TE-mode through the PC. The packet signal sequence was composed of '1,0,0,0' repeated for 6,400 times and the guard time of internal '0,0,0,0' repeated for 19,200 times, which contained 102,400 bits. Thus, for each period the '1,0,0,0' packet signals lasted for 2.56 μs while the guard time lasted for 7.68 μs and totally, one period of the packet signal sequence was 10.24 μs. Figure 3-13(a) shows a single period of the packet signal sequence including 6,400 bits of '1' packet signal. Using another TLD to emit the pump light with a wavelength of 1553.27 nm, the pulse width of pump signal was then set to be 4.096 μs, which could cover the 2.56-μs-long '1,0,0,0' packet signals, through a PPG (WX1281B) and an electro-optic modulator and its period was set to be 40.96 μs that was quadruple compared with period of probe signal, which is shown as Fig. 3-13(b). After being

amplified to a peak power of 16.8 mW by an EDFA, the pump signal was polarized into TM-mode through the PC. The peak power dropped in pump pulse is due to the EDFA but it was beneficial to compensate slow response of heating. Therefore, signal switching was implemented every four periods of packet signals during a period of the pulse pump signal launching synchronized with the packet signals. The output packet signals could be detected by an APD after using the BPF, and then measured by an oscilloscope.

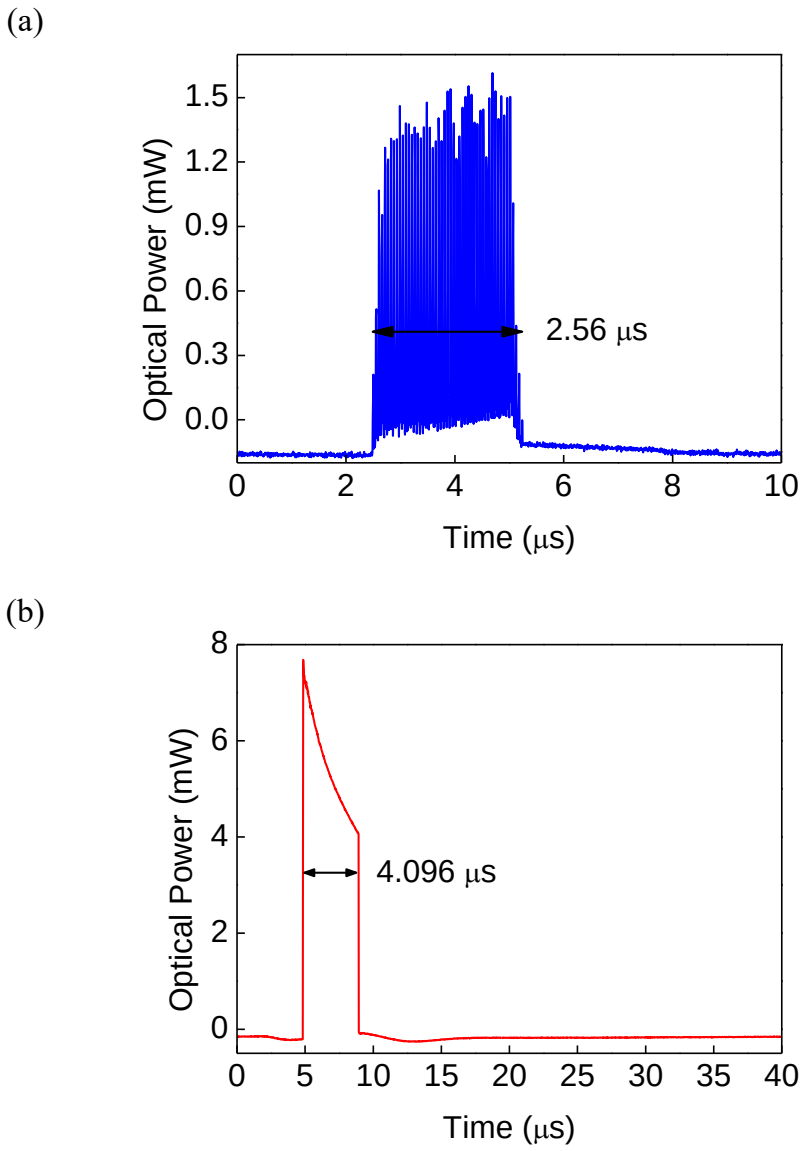

Fig. 3-13 (a) Temporal response of packet signals (λ= 1560.24 nm) in one period applied in burst switching measurement. (b) Temporal response of pulse pump signal

(λ= 1553.27 nm) in one period applied in this measurement.

Figure 3-14 reveals that for every four periods, when the pump signal was induced synchronized with the first period of packet signals, the output light from through port was switching from low level to high level, as we can also see from Fig. 3-12(a). Thus, only the first period of packet signals reached a power of high level, the remaining three periods of packet signals kept its power as the low level at the through port when pump signal was not launched. Similarly, at the drop port the low power level of packet signals of the first period can be observed while inducing the pulse pump signal synchronized with the first period of the probe packet signals. The switching ratio was estimated by on/off state of the packet signals as 7.3 dB and 7.2 dB at through port and drop port, respectively, with a peak pump power of 16.8 mW in the burst switching measurement.

(a)

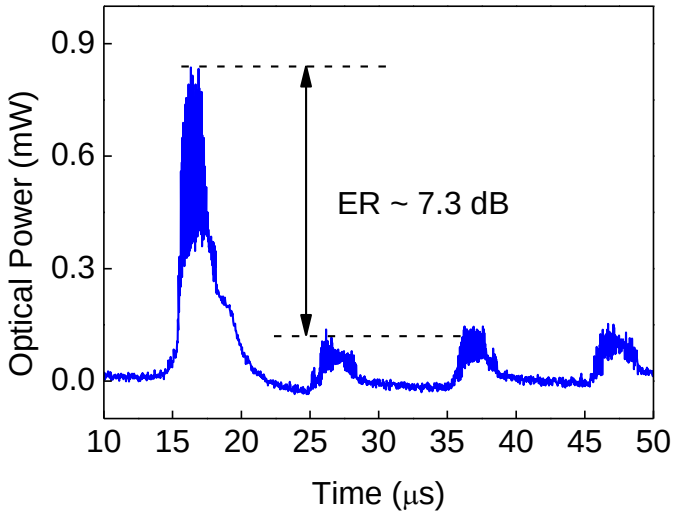

(b)

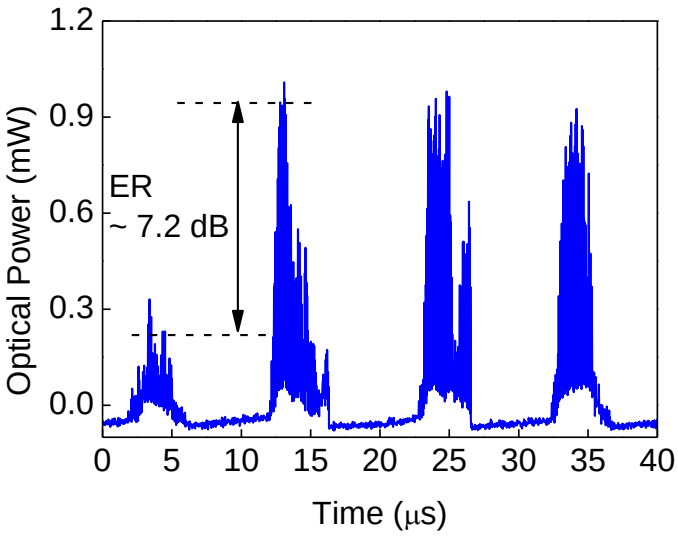

Fig. 3-14 Switching of packet signals in the burst switching measurement at the (a) through port and (b) drop port.

3.5 Summary

We have proposed and demonstrated an all-optical remotely controllable MRR-based TO switch on an SOI platform in this chapter. The fabricated device performed at 10–90 % switching times of 0.71 μs for the rising time and 2.66 μs for the falling time in the temporal response measurement. Moreover, it performed an on/off switching ratio of 7.3 dB at the through port and 7.2 dB at the drop port, with a peak pump power of 16.8 mW in the burst switching measurement, which exhibited a better switching ratio than previous research. This work has been published as a journal paper on *Jpn. J. Appl. Phys.* [8]. Therefore, we successfully verified the efficient heat tuning of the TE-mode-polarized probe signal by the TM-mode-polarized pump light of a remotely controllable TO switch. Based on this idea, our next step is to realize an all-optical broadband switching of a large-scale switch with multiple inputs/outputs that can be applied into practical passive optical network system in the future.

References

1. Y. Kondo, T. Murai, Y. Shoji, et al., “All-Optical Switch by Light-to-Heat Conversion in Metal Deposited Si Ring Resonator,” IEEE Photonics Technology Letters 32(13), 807-810 (2020).
2. W. Bogaerts, P. De Heyn, T. Van Vaerenbergh, K. De Vos, S. Kumar Selvaraja, T. Claes, P. Dumon, P. Bienstman, D. Van Thourhout, R. Baets, “Silicon microring resonators,” Laser & Photon. Rev. 6(1), 47-73 (2012).
3. V. R. Almeida, R. R. Panepucci, and M. Lipson, “Nanotaper for compact mode conversion,” Opt. Lett. 28(15), 1302 (2003).
4. 村井 俊哉, “シリコンリング共振器を用いた 導波路型光メモリに関する研究,” 東京工業大学 大学院理工学研究科, (2018).
5. J. Shim, J. Lim, D.-M. Geum, B. H. Kim, S.-Y. Ahn, and S. Kim, “Tailoring bolometric properties of a TiOx/Ti/TiOx tri-layer film for integrated optical gas sensors,” Opt. Express 29, 18037-18058 (2021).
6. W. Liu, and M. Asheghi, “Thermal Conductivity Measurements of Ultra-Thin Single Crystal Silicon Layers,” ASME. J. Heat Transfer. 128(1), 75–83 (2006).
7. L. Ren, K. Pashayi, H. R. Fard, S. P. Kotha, T. Borca-Tasciuc and R. Ozisik, “Engineering the coefficient of thermal expansion and thermal conductivity of polymers filled with high aspect ratio silica nanofibers,” Composites Part B: Engineering 58, 228-234 (2004).
8. Z. Liang, S. Liu and Y. Shoji, “Improvement of extinction in optically-controlled silicon thermo-optic switch based on micro-ring resonator with distinct probe signal,” Jpn. J. Appl. Phys. 62, 032001 (2023).

Chapter 4

Remotely controllable Mach-Zehnder interferometer-based thermo-optic switch

4.1 Introduction

Owing to the experiment results of the microring resonator-based thermo-optic (TO) switch discussed in Chapter 3, the all-optical TO switching process can be realized effectively by utilizing a TM-mode-polarized pump light to control the TE-mode-polarized signal light. However, the problem of how to realize a broadband switching remains to be solved.

In this chapter, we will discuss the design of the remotely controllable Mach-Zehnder interferometer (MZI)-based TO switch. In order to apply the all-optical TO switch in a remotely controllable time division multiplexing (TDM) passive optical network (PON) system, our goal is to design and demonstrate a 1×8 MZI-based all-optical TO switch that satisfies the demands for remotely controllable TDM-PON system. The first step is to design a 1×2 MZI-based all-optical TO switch, which is an elementary unit of the 1×8 MZI-based all-optical TO switch. Therefore, the operation principle and structural parameters design of the proposed device will be analyzed in detail, and what follows next, is the measured characterization of the proposed device. Last but not least, the comparison between the performance of the proposed device and the expected performance of the remotely controllable TDM-PON system will be discussed.

4.2 Operation principle

In this section, properties of a normal MZI will be introduced at first. The switching process of an MZI-based switch can be realized by tuning the phase shift inside the arms of the MZI structure. Next, the operation principle of the proposed 1×2 MZI-based all-optical TO switch will be discussed. The following section as the operation principle of the proposed 1×8 MZI-based all-optical TO switch, constructed by the elementary unit as the 1×2 MZI-based all-optical TO switch, will be explained as well.

4.2.1 Mach-Zehnder interferometer

Figure 4-1 shows a sample Mach-Zehnder interferometer structure, which consists of two 3-dB couplers for the input/output and two waveguide arms between them. The optical lengths of two arms are equal to each other for a symmetric MZI while an asymmetric MZI contains an optical delay line in the arms. 3-dB couplers can be realized by 1×2 or 2×2 multimode interferometer (MMI) coupler, directional coupler (DC), or mode evolution structure. We analyze this simple model of MZI by cascading the transfer functions of two couplers and that of the optical delay line based on single-mode waveguides.

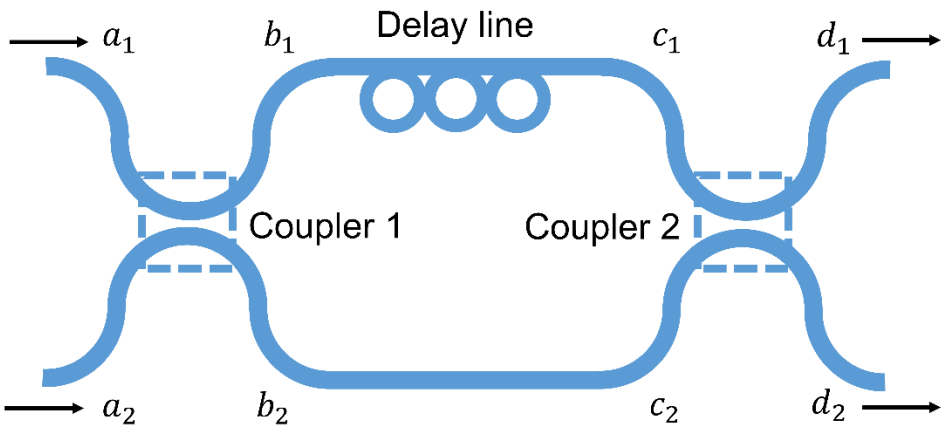

Fig. 4-1 Schematic of a Mach-Zehnder interferometer.

Let the quantities a_1, a_2, b_1, b_2, etc. refer to the complex transfer functions at the respective positions. The transfer matrixes at Coupler 1 and Coupler 2 can be expressed as

$$\begin{pmatrix} b_1 \\ b_2 \end{pmatrix} = \begin{pmatrix} \sqrt{1-\varepsilon_1} & j\sqrt{\varepsilon_1} \\ j\sqrt{\varepsilon_1} & \sqrt{1-\varepsilon_1} \end{pmatrix} \begin{pmatrix} a_1 \\ a_2 \end{pmatrix}, \tag{4.1}$$

and

$$\begin{pmatrix} d_1 \\ d_2 \end{pmatrix} = \begin{pmatrix} \sqrt{1-\varepsilon_2} & j\sqrt{\varepsilon_2} \\ j\sqrt{\varepsilon_2} & \sqrt{1-\varepsilon_2} \end{pmatrix} \begin{pmatrix} c_1 \\ c_2 \end{pmatrix}, \tag{4.2}$$

where the power splitting coefficients of Coupler 1 and Coupler 2 are ε_1 and ε_2, respectively. For this MZI model, we assume power splitting ratios of both couplers are 50% as a normal MZI uses 3-dB couplers, and thus, $\varepsilon_1 = \varepsilon_2 = 0.5$ and Eqs. (4.1) and (4.2) simplify into

$$\begin{pmatrix} b_1 \\ b_2 \end{pmatrix} = \frac{1}{\sqrt{2}} \begin{pmatrix} 1 & j \\ j & 1 \end{pmatrix} \begin{pmatrix} a_1 \\ a_2 \end{pmatrix}, \tag{4.3}$$

and

$$\begin{pmatrix} d_1 \\ d_2 \end{pmatrix} = \frac{1}{\sqrt{2}} \begin{pmatrix} 1 & j \\ j & 1 \end{pmatrix} \begin{pmatrix} c_1 \\ c_2 \end{pmatrix}. \tag{4.4}$$

Suppose the propagation constants of lights in the upper arm and lower arm are $\beta_1 = \frac{2\pi n_1}{\lambda}$ and $\beta_2 = \frac{2\pi n_2}{\lambda}$, while the waveguides of the upper arm and lower arm have lengths L_1 and $L_2 = L_1 - \Delta L$, respectively. Since the phase delays of the two waveguides are $\varphi_1 = \beta_1 L_1$ and $\varphi_2 = \beta_2 L_2$, the relation between $\begin{pmatrix} b_1 \\ b_2 \end{pmatrix}$ and $\begin{pmatrix} c_1 \\ c_2 \end{pmatrix}$ is given by

$$\begin{pmatrix} c_1 \\ c_2 \end{pmatrix} = \begin{pmatrix} e^{-j\varphi_1} & 0 \\ 0 & e^{-j\varphi_2} \end{pmatrix} \begin{pmatrix} b_1 \\ b_2 \end{pmatrix}, \tag{4.5}$$

From Eqs. (4.1) – (4.3) we can derive the relation between $\begin{pmatrix} a_1 \\ a_2 \end{pmatrix}$ and $\begin{pmatrix} d_1 \\ d_2 \end{pmatrix}$ as

$$\begin{pmatrix} d_1 \\ d_2 \end{pmatrix} = \frac{1}{\sqrt{2}} \begin{pmatrix} 1 & j \\ j & 1 \end{pmatrix} \begin{pmatrix} e^{-j\varphi_1} & 0 \\ 0 & e^{-j\varphi_2} \end{pmatrix} \frac{1}{\sqrt{2}} \begin{pmatrix} 1 & j \\ j & 1 \end{pmatrix} \begin{pmatrix} a_1 \\ a_2 \end{pmatrix}, \tag{4.6}$$

which can be simplified as

$$\begin{pmatrix} d_1 \\ d_2 \end{pmatrix} = \frac{1}{2}\begin{pmatrix} e^{-j\varphi_1} - e^{-j\varphi_2} & je^{-j\varphi_1} + je^{-j\varphi_2} \\ je^{-j\varphi_1} + je^{-j\varphi_2} & e^{-j\varphi_2} - e^{-j\varphi_1} \end{pmatrix}\begin{pmatrix} a_1 \\ a_2 \end{pmatrix}. \tag{4.7}$$

If $\begin{pmatrix} a_1 \\ a_2 \end{pmatrix} = \begin{pmatrix} 1 \\ 0 \end{pmatrix}$, which means the input light is only from one input port (Coupler 1 can be also seen as a 1×2 3-dB coupler), we have

$$d_1 = \frac{1}{2}\left(e^{-j\varphi_1} - e^{-j\varphi_2}\right)a_1 = -e^{-j\varphi_0}\sin\left(\frac{\Delta\varphi}{2}\right), \tag{4.8}$$

and

$$d_2 = \frac{1}{2}j\left(e^{-j\varphi_1} + e^{-j\varphi_2}\right)a_1 = je^{-j\varphi_0}\cos\left(\frac{\Delta\varphi}{2}\right), \tag{4.9}$$

where $\varphi_0 = \frac{\varphi_1+\varphi_2}{2}$ is the average phase delay, and $\Delta\varphi = \varphi_1 - \varphi_2$ is the differential phase shift of the two arms of the MZI structure. Hence, the power transmissions $|d_1|^2$ and $|d_2|^2$ satisfy

$$\begin{cases} |d_1|^2 = \sin^2\left(\frac{\Delta\varphi}{2}\right) \\ |d_2|^2 = \cos^2\left(\frac{\Delta\varphi}{2}\right) \end{cases}. \tag{4.10}$$

If two arms of the MZI structure have the same refractive index ($n_1 = n_2 = n$) and the length of the delay line in this asymmetric MZI is ΔL, $\Delta\varphi$ can be written as

$$\Delta\varphi = \frac{2\pi n\Delta L}{\lambda}. \tag{4.11}$$

Under the condition $\begin{pmatrix} a_1 \\ a_2 \end{pmatrix} = \begin{pmatrix} 1 \\ 0 \end{pmatrix}$, if $\varphi = (2m+1)\pi$, where $m = 0, \pm1, \pm2, \pm3\cdots$, we have

$$\begin{cases} |d_1|^2 = 1 \\ |d_2|^2 = 0 \end{cases}. \tag{4.12}$$

On the other hand, if $\varphi = 2m\pi$, where $m = 0, \pm1, \pm2, \pm3\cdots$, we have

$$\begin{cases} |d_1|^2 = 0 \\ |d_2|^2 = 1 \end{cases}. \tag{4.13}$$

This implies that when the induced phase difference between the MZI arms correspond to π, the output can be shifted from cross to bar port. Moreover, for a symmetric MZI which has no initial phase difference between two arms, it offers broadband operating wavelengths and effectively avoids the free spectral range (FSR)

matching or alignment during the wavelength switching [1].

4.2.2 1×2 Mach-Zehnder interferometer-based all-optical thermo-optic switch

Before explaining the operation principle of a 1×8 MZI-based all-optical TO switch, it is necessary to analyze the operation principle of an elementary unit of such device, which is the 1×2 MZI-based all-optical TO switch, whose design will be discussed in Section 4.3. Figure 4-2 shows a 3-D schematic structure of the proposed device.

The proposed 1×2 MZI-based all-optical TO switch consists of a silicon 1×2 MZI structure designed for TE-polarized input, the metal heater embedded above the waveguides and two extra waveguides, one is for TM-polarized pump control light input and the other is used to balance the loss between two arms of the MZI, as shown in Fig. 4-2. Since this device is based on a silicon-on-insulator (SOI) platform, the background material surrounding silicon waveguides and metal heater is silicon dioxide. The area composed of the metal heater as well as the waveguides for TM-polarized pump control light and TE-polarized signal light can be regarded as an all-optical TO phase shifter in the proposed structure, whose design will be discussed later in Section 4.3 together with the design of the MZI structure, which consists of a 1×2 multimode interferometer (MMI) coupler for the input, a 2×2 MMI coupler for the output and two arms waveguides between them.

As discussed in Chapter 2, when a high-intensity TM-polarized light is induced to the all-optical TO phase shifter with a metal layer, temperature increase will occur caused by the light-induced heat. Therefore, initially, the TE-polarized input light comes out from the 1×2 MMI of the MZI equally. Meanwhile, a high-intensity TM-polarized pump control light is induced and propagates in the waveguide for TM-polarized light input. At the all-optical TO phase shifter which deposits the buried metal layer, most of the TM-polarized pump control light is absorbed by the metal layer while the input light propagating inside the arms waveguides has little loss owing to its TE-mode polarization (and is barely coupled to the adjacent waveguide if there is an adjacent waveguide for the TM-polarized light input inside the TO phase shifter). Since the metal layer is

deposited above the silicon waveguides with a short distance between them, the temperature in the all-optical TO phase shifter increases immediately through light-to-heat conversion from the metal. The phase difference is generated between two arms of the MZI due to TO effect and it will modify light power distribution in the 2×2 MMI of the MZI. According to Eqs. (4.10) – (4.13), the output states can be alternated when this phase difference corresponds to π. Consequently, the all-optical switching between the bar-port output and the cross-port output is achieved by this TO phase shift of the MZI. Besides, the metals are embedded above both arms of the MZI so as to balance the loss between two arms.

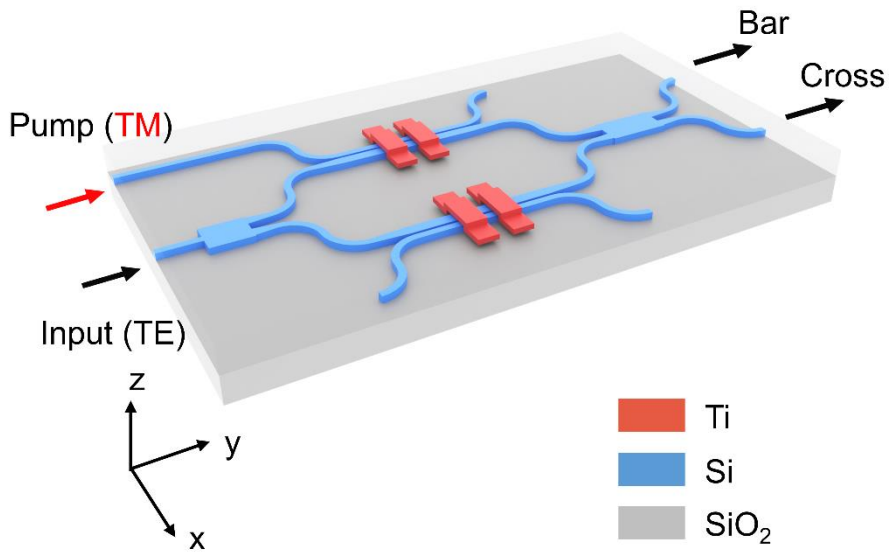

Fig. 4-2 Schematic of the proposed 1×2 MZI-based all-optical TO switch.

4.2.3 1×8 Mach-Zehnder interferometer-based all-optical thermo-optic switch

The schematic structure of the proposed 1×8 MZI-based all-optical TO switch is shown in Fig. 4-3, which has 16 input/output ports including one TE-polarized input light port, seven TM-polarized pump control lights input ports ($Pump_1$, $Pump_{2\_i\ (i = 1,2)}$ and $Pump_{3\_i\ (i = 1–4)}$) that used to control the output states and eight output ports ($Out_{i\ (i = 1–8)}$). As we can see from 3-D structures shown in Figs. 4-2 and 4-3, the proposed 1×8 MZI-

based all-optical TO switch is constructed by cascading the elementary units of the 1×2 MZI-based all-optical TO switch. A single input can be allocated to any one of the eight output ports through three stages of cascaded 1×2 MZIs while totally three pump control lights are applied. For example, the input light can be switched to the output side for Out_1–Out_4 when propagating through the first 1×2 MZI-based switch as we induce pump control light $Pump_1$ with a certain power. Subsequently, it will be switched to the output side for Out_1–Out_2 as we induce $Pump_{2\_1}$ with a certain power simultaneously and finally switched to output port Out_1 as we induce $Pump_{3\_1}$ with a certain power simultaneously. Similarly, for other output ports, we can add particular combination of pump control lights to remotely control the switching states.

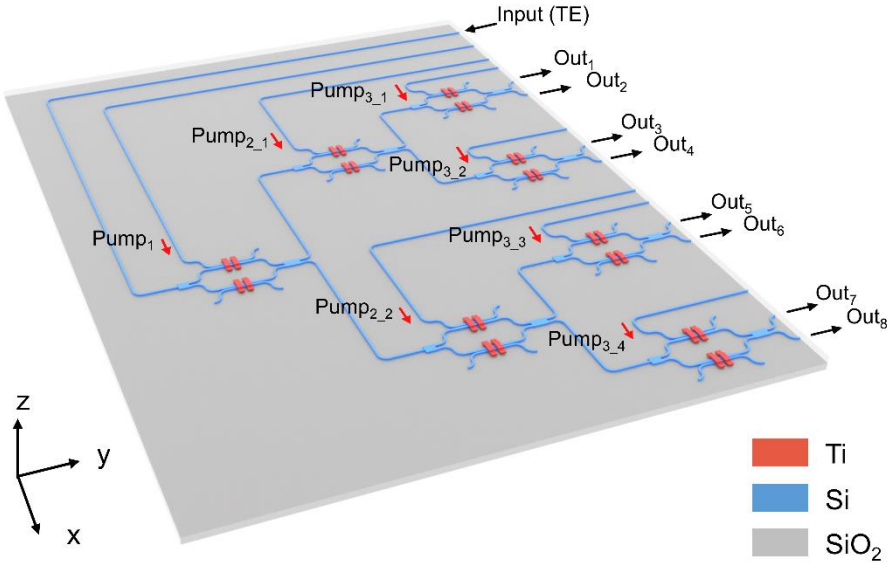

Fig. 4-3 Schematic of the proposed 1×8 MZI-based all-optical TO switch.

The application of the proposed remotely controllable 1×8 MZI-based all-optical TO switch in a practical optical system can be found in Fig. 4-4. A wavelength division multiplexing (WDM) coupler can be used to divide the input light into control signal and

data signal with different waveguide range, as shown in Fig. 4-4(a). The control signal can be further divided into multiple inputs and then polarized into TM mode, which can control the TO phase shifters inside the switch. On the other hand, the data signal will be polarized into TE mode as the input of the device. In order to make a better description for the input lights, we propose a concept of data processing as the application of this device, as shown in Fig. 4-4(b), where the pump lights are assumed to be allocated in L-band wavelength range (λ = 1565–1625 nm) with narrow bandwidth since we assume the burst or circuit switching in the time domain for wideband signal light among C-band wavelength range (λ = 1530–1565 nm). This mean of data processing satisfies the characteristic of PONs system and can reduce the cost by using all-optical signal processing. As discussed in Section 1.3.3, the proposed device can be expected to be applied in a remotely controllable TDM-PON system.

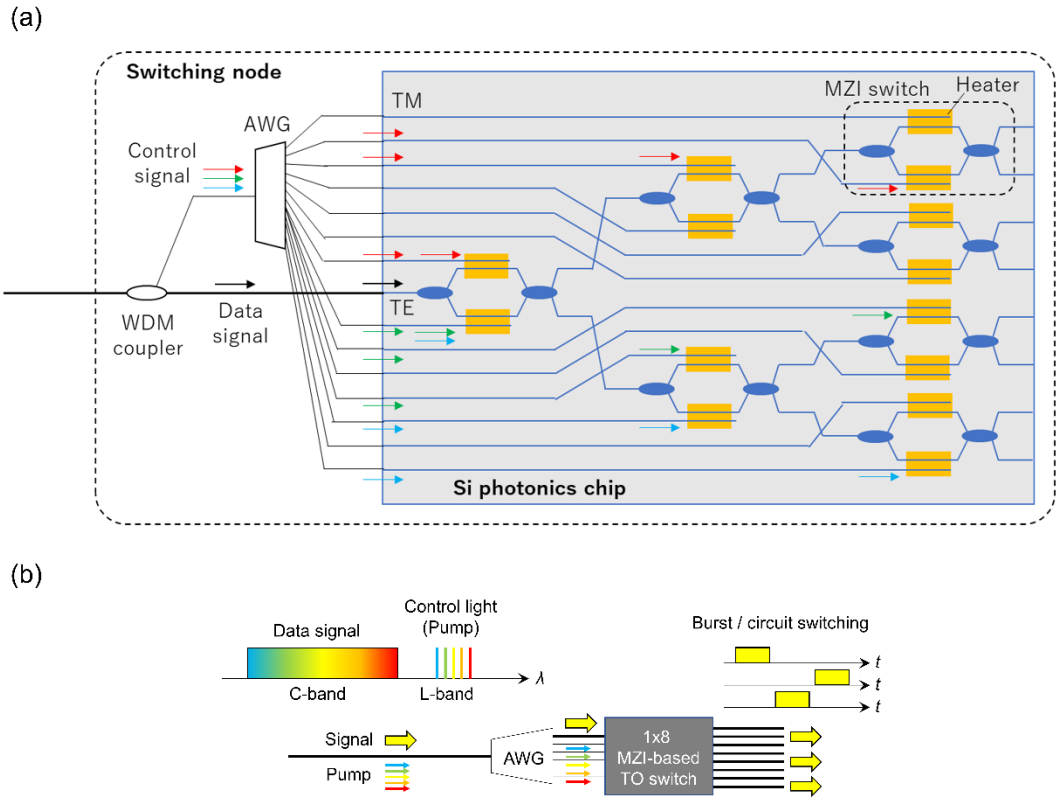

Fig. 4-4 (a) Assumed practical optical system as the application of the proposed remotely controllable 1×8 MZI-based all-optical TO switch. (b) A concept of data processing as the application of the proposed device.

4.3 Device design and experiment

In this section, the design of the 1×2 MZI-based all-optical TO switch will be investigated and determined using the methods of simulation, calculation and experiments as the main content. We will start from designing the input/output MMI couplers for the basic structure of the MZI. Then, we will consider two-types of design for the all-optical TO phase shifter, which is the most important component of the device. Lastly, we will discuss about the routing design of the 1×8 MZI-based all-optical TO switch shortly.

4.3.1 Design of the 1×2 Mach-Zehnder interferometer-based all-optical thermo-optic switch

For the design of the 1×2 MZI-based all-optical TO switch, we generally divide the design into two parts. The first part is to design the input/output couplers of the MZI structure, which are a 1×2 MMI coupler as the input and a 2×2 MMI coupler as the output in our proposed device. Then, we will design the all-optical TO phase shifter, using a metal layer deposited above the silicon waveguide as the heater. We will consider the TO phase shifter with a single waveguide which is similar to the design of MRR-based TO switch described in Section 3.3 at first. Then, we will also consider the TO phase shifter using two adjacent waveguides which has been simulated in Section 2.3.2.

4.3.1.1 Multimode interferometer couplers

To obtain a broadband switching characteristic, we firstly designed a symmetric 1×2 MMI coupler as the input of the MZI which inherently gives a balanced division of the input light. This 1×2 MMI structure consists of a tapered input, two tapered outputs and a coupler. The width and the length of this MMI coupler were designed to be 2.21 μm and 4.152 μm, respectively. We then designed the linear tapers for input and output

waveguides. For the input waveguide, the linear taper structure was 0.5-μm-wide for the input side and 0.91-μm-wide for the output side with a length of 5.776 μm. For both of the output waveguides, the linear taper structure was 0.91-μm-wide for the input side and 0.5-μm-wide for the output side also with a length of 5.776 μm. There was a 0.19-μm-wide gap between the beginnings of the output tapered waveguides. Utilizing Lumerical MODE solutions, we simulated the transmission field distribution of this structure, as shown in Fig. 4-5, while adding a fundamental TE-mode-polarized light to the input port (P_{in}). The splitting ratio of the 1 × 2 MMI coupler can be defined as P_{out1}/ P_{in} or P_{out2}/ P_{in}, which denotes to transmission power rate of output power compared to input power at bar output port or cross output port, respectively. Simulated results of the splitting ratio of the 1 × 2 MMI coupler are as shown in Fig. 4-6, which was 0.494 at the wavelength around 1550 nm for both output ports. It indicates a same transmission for the output power at bar port and cross port. A low insertion loss can be observed from the simulation by calculation the sum of transmission power rates at two output ports.

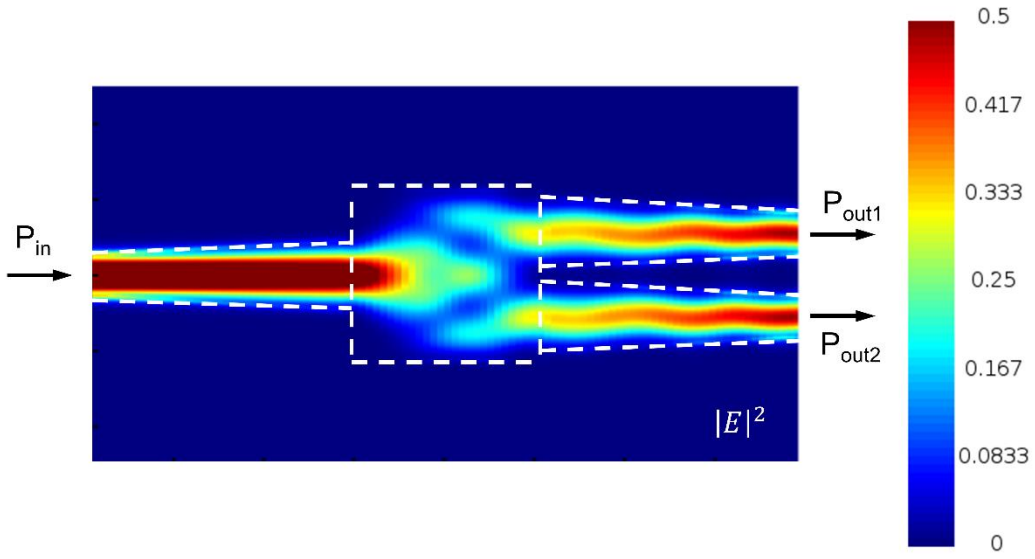

Fig. 4-5 Simulated transmission field distribution of 1×2 MMI coupler.

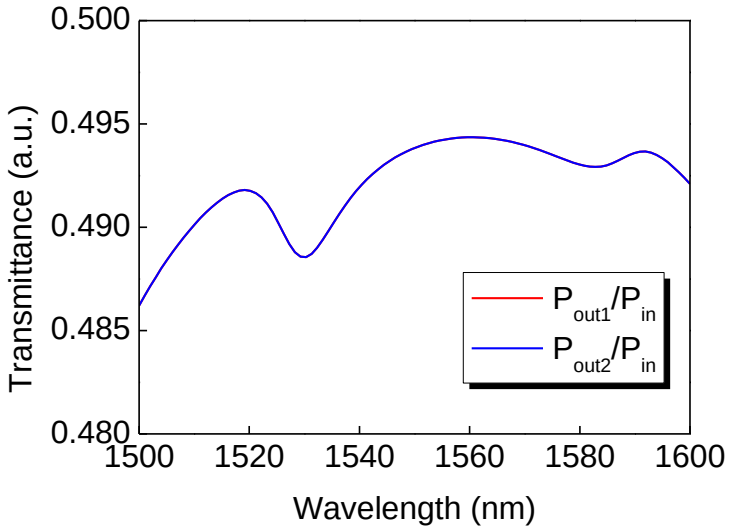

Fig. 4-6 Simulated splitting ratio of 1×2 MMI coupler for TE mode input.

We then designed a 3-dB 2×2 MMI coupler as the output of the MZI. The width and the length of this MMI coupler were designed to be 2.21 μm and 16.602 μm, respectively. We also designed the linear tapers for input and output waveguides. For both of the input waveguides, the linear taper structure was 0.5-μm-wide for the input side and 0.91-μm-wide for the output side with a length of 12.2 μm. There was a 0.19-μm-wide gap between the ends of the input tapered waveguides. Inverse structures for the output waveguides were designed for the 2×2 MMI coupler compared with the input waveguides. Utilizing Lumerical MODE solutions, we simulated the transmission field distribution of this structure, as shown in Fig. 4-7, while adding a fundamental TE-mode-polarized light to the upper input port (P_{in1}). The splitting ratio of the 2 × 2 MMI coupler can be defined as P_{out1}/ P_{in1} or P_{out2}/ P_{in1}, which denotes to transmission power rate of output power compared to input power at bar output port or cross output port, respectively. Simulated results of the splitting ratio of the 2 × 2 MMI coupler are as shown in Fig. 4-8, which were 0.422 and 0.494 at the wavelength around 1550 nm for P_{out1}/ P_{in1} and P_{out2}/ P_{in1}, respectively. It indicates a small difference between the output power at bar port and cross port, which can be eliminated by tuning the phase of the input lights. A low insertion loss can be observed from the simulation by calculation the sum of transmission power rates at two output ports.

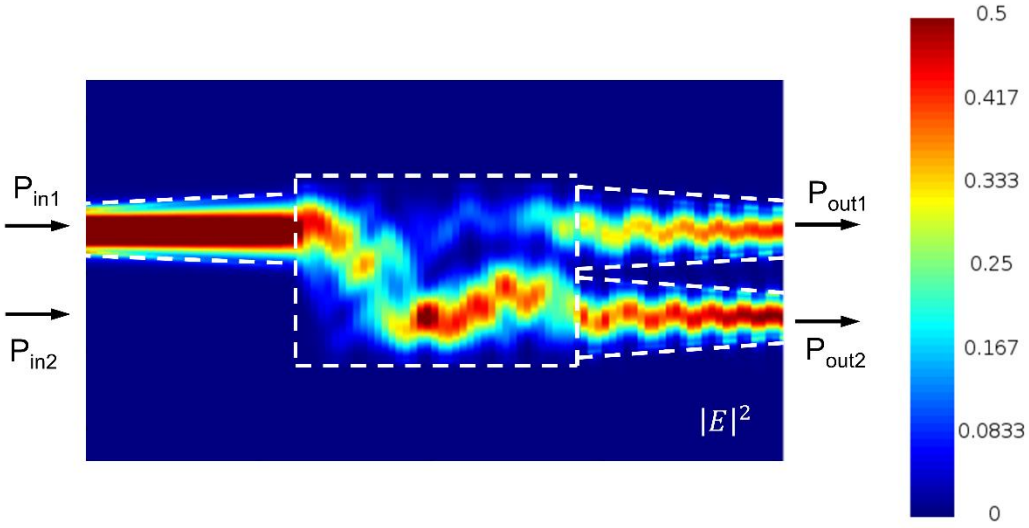

Fig. 4-7 Simulated transmission field distribution of 2×2 MMI coupler.

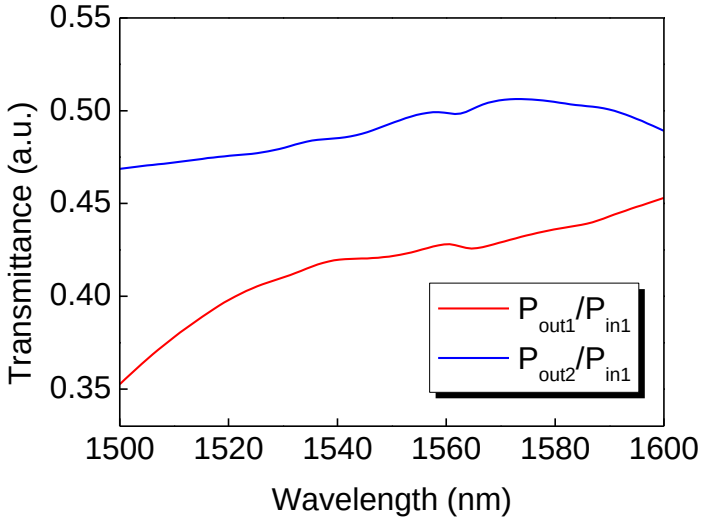

Fig. 4-8 Simulated splitting ratio of 2×2 MMI coupler for one TE mode input.

4.3.1.2 Thermo-optic phase shifter (type-A)

Taking the effective switching process in a microring resonator-based all-optical TO switch into account, the refractive index of a single silicon waveguide can be modified by a high-intensity TM-mode-polarized pump light propagating within the waveguide when a metal layer is deposited above the waveguide. Thus, the idea of using a single waveguide for the all-optical TO phase shifter in the MZI structure came into our mind. Consequently, we designed a 1×2 MZI-based all-optical TO switch using the all-optical TO phase shifter composed of a TM/TE mode combiner and a single waveguide with a metal layer embedded above (we called it as type-A TO phase shifter hereafter), as shown in Fig. 4-9. The TM/TE mode combiner in the MZI was used to combine the TM-mode-polarized pump light and the TE-mode-polarized signal light into the arm waveguide of the MZI. Note that, two combiners and two metal layers inside the MZI structure, which can be seen in Fig. 4-9, were used to balance the loss between two arms of the MZI.

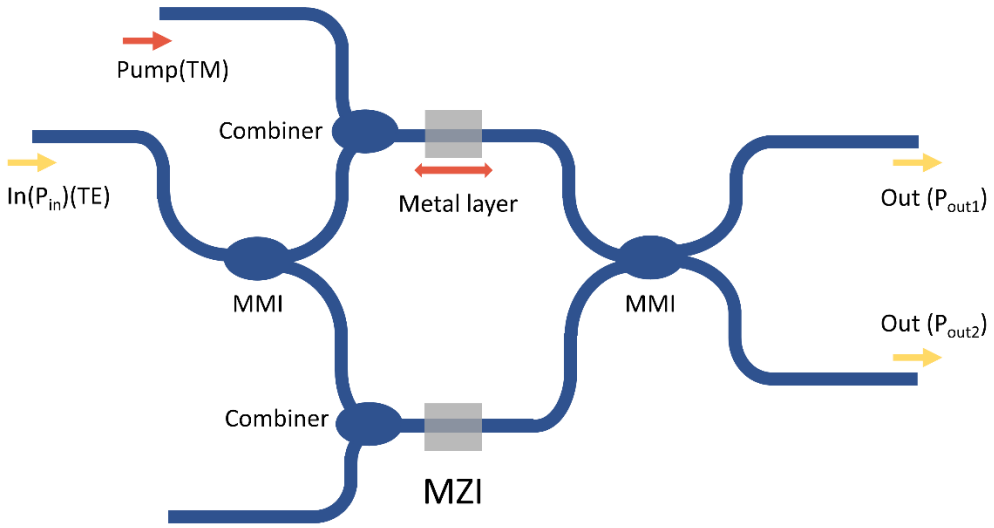

Fig. 4-9 Schematic diagram of a 1×2 MZI-based all-optical TO switch using type-A TO phase shifter.

The operation principle of this device was the same as the description in Section 4.2.2. The TM/TE mode combiner had a design of two symmetric waveguides with a width of 440 nm and a gap of 240 nm between them. The coupling length of this combiner was designed to be 4 μm to let the TM mode be coupled to the adjacent waveguide and suppress the coupling loss of TE mode. A simulated transmission field distribution of designed TM/TE mode combiner in type-A TO phase shifter is shown as Fig. 4-10. As shown in Fig. 4-10(a), when a fundamental TM mode with a waveguide of 1550 nm was injected to the upper waveguide, a TM mode light with about 60.0% of its power was transmitted to the lower waveguide. On the other hand, as shown in Fig. 4-10(b), when a fundamental TE mode with a waveguide of 1550 nm was injected to the lower waveguide, a TE mode light with about 79.8% of its power was left to propagate in the lower waveguide through this TM/TE mode combiner.

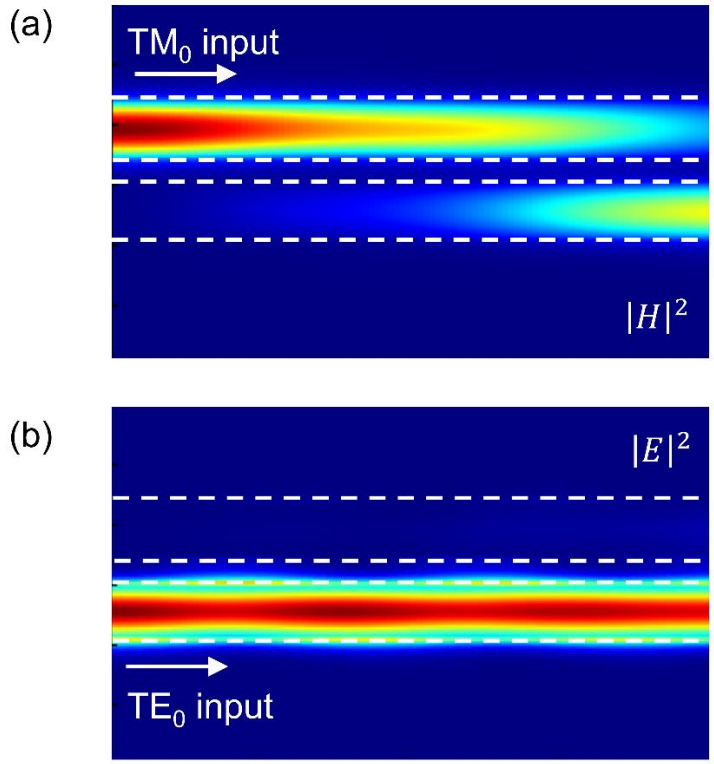

Fig. 4-10 Simulated transmission field distribution of (a) fundamental TM mode input and (b) fundamental TE mode input for the designed TM/TE mode combiner in

type-A TO phase shifter.

Based on the experiment results of the MRR-based TO switch described in Sections 3.3 and 3.4, we decided to use a distance of 170 nm between the silicon waveguide and metal layer. Using the design of type-A TO phase shifter, we fabricated the device with different lengths of Ti layer and measured the characterization of the fabricated device, as shown in Fig. 4-11, while a continuous-wave TM-polarized pump light with a power of 49.4 mW was induced to each of the fabricated device. It reveals a high insertion loss of more than 5 dB can be observed for the fabricated device when depositing an added 5-μm-long Ti layer. The insertion loss of the fabricated device was from the coupling loss of the TM/TE mode combiner for TE mode as well as the absorption loss by the metal layer for TE mode. On the other hand, the MZI-based switches performed relatively low extinction ratios because loss mismatch between two arms of the MZI structure may be caused by the coupled TM-polarized pump light.

(a)

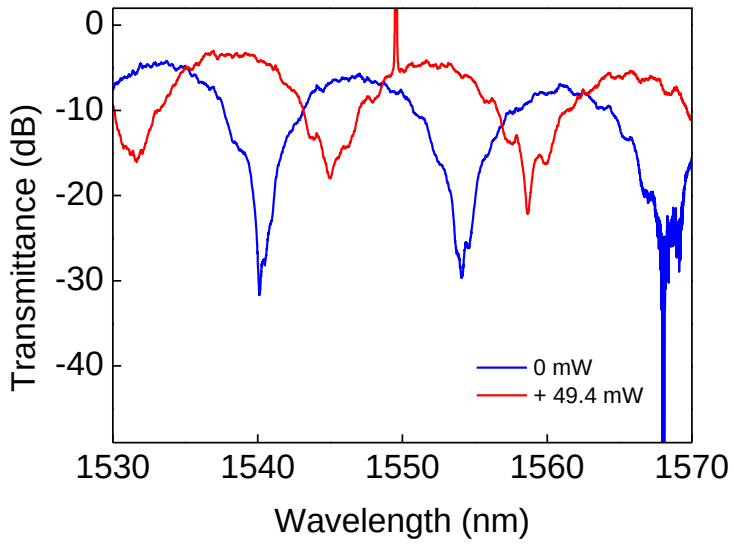

(b)

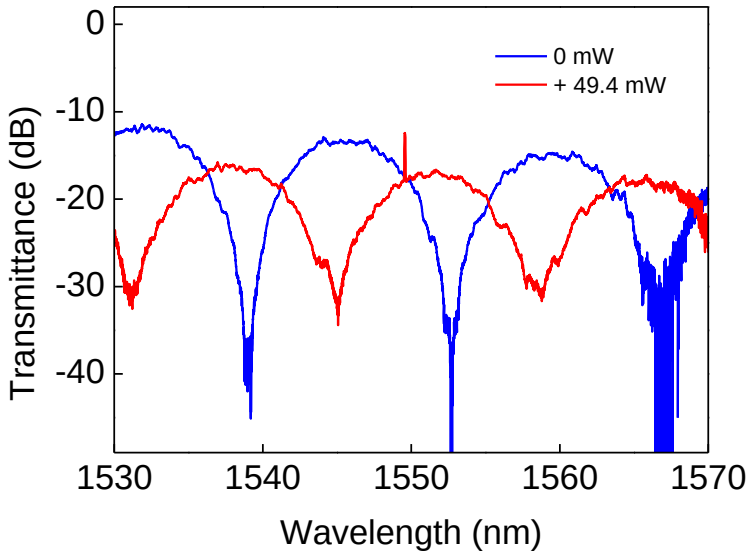

(c)

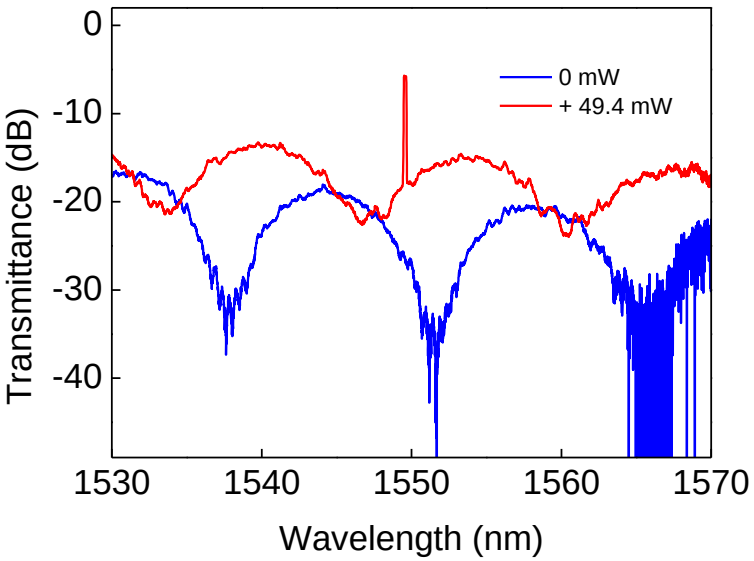

Fig. 4-11 (a) – (c) Transmission spectra of the fabricated asymmetric 1×2 MZI-based TO switch using type-A TO phase shifter with a deposited metal layer that had the length of (a) 5 μm, (b) 10 μm and (c) 15 μm, when applying a continuous pump control light.

4.3.1.3 Thermo-optic phase shifter (type-B)

Because of the unsatisfactory performance of the 1×2 MZI-based all-optical TO switch using type-A TO phase shifter, we considered to design two adjacent waveguides inside the TO phase shifter and one of the adjacent waveguides was applied the TM-mode-polarized pump control light. If the distance between two adjacent waveguides is close enough, it can be expected that the light-induced heat is adequate to cause a phase shift inside the TO phase shifter when a high-intensity pump light is injected into it. Figure 4-12(a) shows the structure of this re-designed TO phase shifter (we called it as type-B TO phase shifter hereafter). Ideally there is no light coupling supposed to occur in this type-B TO phase shifter. However, as the gap between two adjacent waveguides should be small enough for better heat conduction, losses of the pump light as well as signal light are not negligible. The gap was designed to be 200 nm due to the resolution of fabrication. The illustration of Fig. 4-12(b) shows the detailed design for type-B all-optical TO phase shifter, where the width of the waveguide for TM-polarized pump light was defined as $b\ nm$ while the width of the waveguide for TE-polarized signal light (probe) was defined as $a\ nm$.

(a)

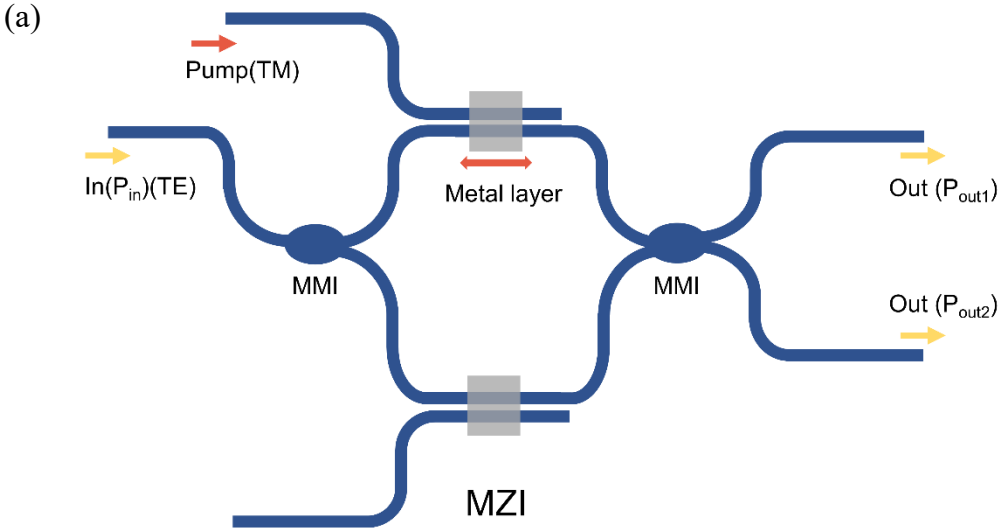

(b)

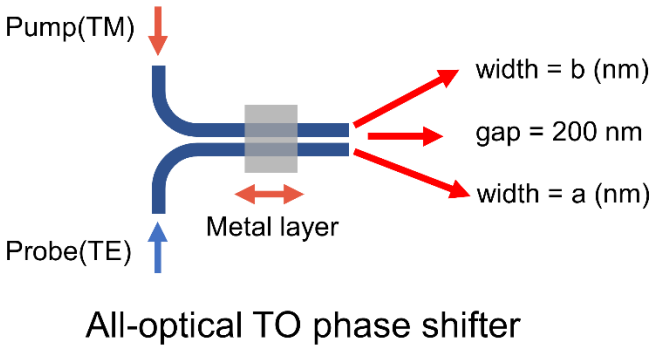

Fig. 4-12 (a) Schematic diagram of a 1×2 MZI-based all-optical TO switch using type-B TO phase shifter. (b) Detailed design for type-B all-optical TO phase shifter.

Firstly, since our proposed 1×2 MZI-based all-optical TO switch is for single-mode input light, we decided to assume the width of the waveguide for TE-polarized signal light as $a = 450\,nm$. Subsequently, the simulation of the TM-polarized light propagating in the waveguide for pump light (we called it the wide waveguide because this waveguide was basically wider than the 450-nm-wide waveguide) as well as the TE-polarized light propagating in the 450-nm-wide waveguide (we called it the narrow waveguide) was performed utilizing Lumerical MODE solutions under varying the width of the wide waveguide, as shown in Fig. 4-13(a). It reveals that the transmission rate of fundamental TM mode in the wide waveguide increased as this width increased. In order to have high transmission rates for both of TM and TE mode propagating in their own waveguides, we adopted the width of the wide waveguide as 800 nm, which was also the parameter of this structure in the following discussion. Under this condition, transmission rates for the TM and TE mode were approximately 87.5% and 99.4%, respectively. For the pump light, we designed the 10-μm-long tapered waveguide with the input width of 450 nm and output width of 800 nm for it to propagate through the 800-nm-wide straight waveguide adjacent to the one for TE mode input. The distance between silicon waveguides and metal layer should be considered as another crucial parameter. Assumed the thickness of Ti layer was 20 nm and the length of it was 15 μm, we can simulate light absorption rate of the TM mode in wide waveguide and loss of the

TE mode in narrow waveguide with different distance mentioned previously. Figure 4-13(a) shows that the light absorption rate and the loss increased when the distance was shortened, revealing a trade-off relationship between them because a high light absorption rate for the TM-mode-polarized pump light and low loss for the TE-mode-polarized input light was demanded for the device. We derived a high light absorption rate of 86.4% for TM mode and a loss of 2.1 dB for TE mode when the distance was around 230 nm. We adopted the distance as 230 nm which was a choice that can balance the trade-off relationship between light absorption rate for TM mode and loss for TE mode. Using the design of type-B TO phase shifter with the parameters mentioned above, we fabricated the device with a 15-μm-long Ti layer and measured the characterization of the fabricated device, as shown in Fig. 4-14, while a continuous-wave (CW) TM-polarized pump light with a power of 49.4 mW was induced to the fabricated device. As depicted in Fig. 4-14, the transmission spectra of the fabricated device had a nearly π phase shift when inducing that pump light and a relatively high extinction ratio of more than 20 dB can be observed. However, the insertion loss of this device was around 5 dB, which was far from our target insertion loss of 1 dB for the 1×2 MZI-based TO switch that can be applied in the remotely controllable TDM-PON system. Better design of the TO phase shifter should be considered.

(a)

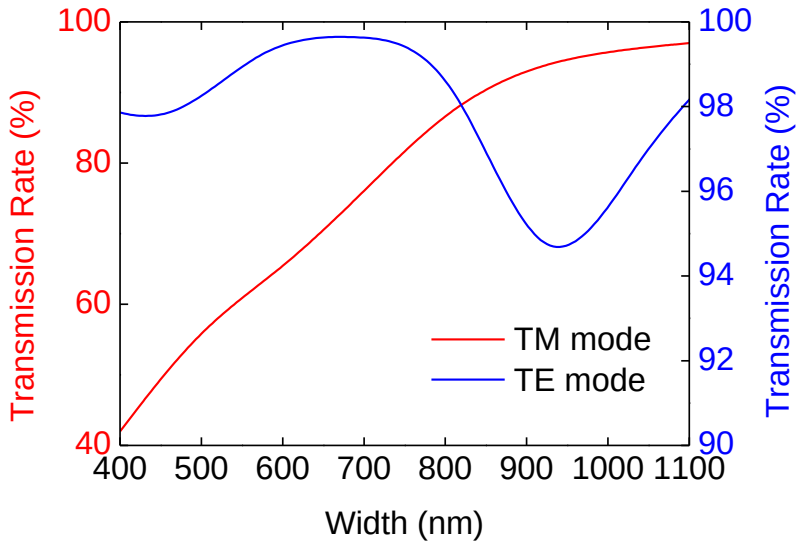

(b)

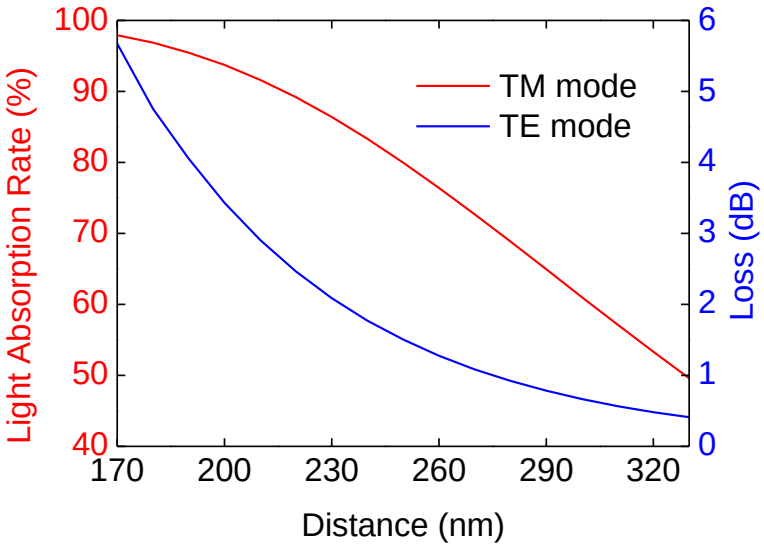

Fig. 4-13 (a) Transmission rate of TM mode in wide waveguide and of the TE mode in narrow waveguide as a function of the width of wide waveguide. (b) Light absorption rate of the TM mode in wide waveguide and loss of the TE mode in narrow waveguide as a function of the distance between the silicon waveguide and metal layer of the 15-μm-long TO phase shifter.

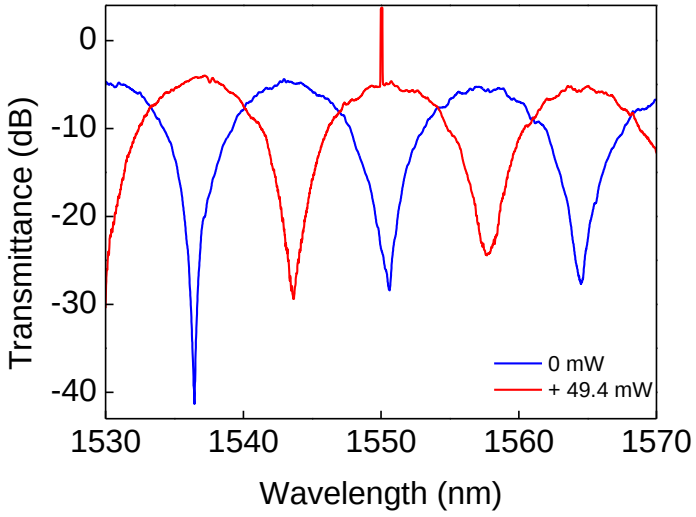

Fig. 4-14 Transmission spectra of the fabricated asymmetric 1×2 MZI-based TO switch using 450-nm-wide waveguide for TE mode and 800-nm-wide waveguide for

TM mode when applying a continuous pump control light.

To reduce the insertion loss of the device, we considered to design a wider waveguide for TE mode inside the all-optical TO phase shifter owing to a stronger confinement of TE mode. Meanwhile, since higher absorption of TM mode by the metal layer above occurs when the waveguide propagating TM mode becomes narrower, the width of the waveguide for pump light was determined to be 350 nm, which means $b = 350\,nm$ described in Fig. 4-12(b). Similar to the simulation described previously, by varying the width of a described in Fig. 4-12(b), the simulation of the TM-polarized light propagating in the 350-nm-wide waveguide (we called it the narrow waveguide) as well as the TE-polarized light propagating in the waveguide for signal light (we called it the wide waveguide because this waveguide was basically wider than the 350-nm-wide waveguide) was performed utilizing Lumerical MODE solutions, as shown in Fig. 4-15(a). The higher the transmission rate for the TM mode, the higher the power of the pump control light remaining in the narrow waveguide. The maximum transmission rate for the TM mode is 79.4% when the width of the wide waveguide is approximately 750 nm, whereas the corresponding transmission rate for the TE mode is 99.2%. Consequently, we adopted a wide waveguide width of 750 nm, which was also a parameter used in the following simulations. We assumed that the thickness of Ti layer was 20 nm and the length of it was 10 μm in the following simulation. Figure 4-15(b) shows the light absorption rate of TM-mode-polarized light in a narrow waveguide and loss of TE-mode-polarized light in the wide waveguide of the TO phase shifter when changing the distance between the silicon waveguide and metal layer. An increase in the light absorption rate was observed, while the loss also increased when the distance was shortened, revealing a trade-off relationship between them as well. We derived the highest contrast in the absorption loss of the metal layer between the TM mode in the narrow waveguide and TE mode in the wide waveguide of approximately 230 nm for the distance when the light absorption rate of the TM mode was over 80%. Therefore, the distance was determined to be 230 nm, to ensure that adequate pump light was absorbed by the metal layer and converted to heat. Under these conditions, the light-absorption

rate of the TM-polarized light in the narrow waveguide was 83.7%, whereas the loss of the TE-polarized input light in the wide waveguide was approximately 0.7 dB. The signal light was injected to this wide waveguide of the arm of the MZI through a 10-μm-long tapered waveguide with the input width of 450 nm and output width of 750 nm. For the pump control light, we also designed the 10-μm-long tapered waveguide with the input width of 450 nm and output width of 350 nm for it to propagate through the 350-nm-wide narrow waveguide inside the TO phase shifter. On the output side of the TO phase shifter, there is an inverse-tapered waveguide for input light propagating in a single mode. The loss in these tapered waveguides is negligible compared to the absorption loss caused by the metal. For the 1×2 MZI-based TO switch using the design of this type-B TO phase shifter excluding the metal layer, we performed a 2.5D variational FDTD (var-FDTD) simulation in Lumerical MODE solutions to analyze its insertion loss. An insertion loss of approximately 0.6 dB was simulated for a fundamental TE mode input.

On the other hand, from the simulation results stated in Section 2.3.2, we can estimate the theoretical tuning efficiency of this all-optical TO phase shifter. Actually, the structural parameters of the simulation model described in Section 2.3.2 were consistent with that of the TO phase shifter mentioned above. Therefore, utilizing COMSOL Multiphysics, when a TM-polarized pump control light with a power of 5 mW was injected to this 10-μm-long TO phase shifter, the phase shift $\Delta\varphi$ was calculated as 0.317 π. Considering the linear relationship between the temperature change and pump light power [2] along with the transmission rate and light absorption rate of the TM-polarized light propagating in the narrow waveguide, the theoretical tuning efficiency of the 10-μm-long TO phase shifter was calculated as 0.042 π/mW. Using the design of type-B TO phase shifter with the parameters mentioned above, we fabricated the device with a 20-μm-long Ti layer and measured the characterization of the fabricated device, as shown in Fig. 4-16, while a continuous-wave TM-polarized pump light with a power of 49.4 mW was induced to the fabricated device. A phase shift of the transmission spectra near π phase shift as well as a low insertion loss of less than 1 dB of the fabricated device can be observed, which was the best performance of above designed device. Further characterization of the device using the design of type-B TO phase shifter with the

parameters mentioned above will be discussed in the next section.

(a)

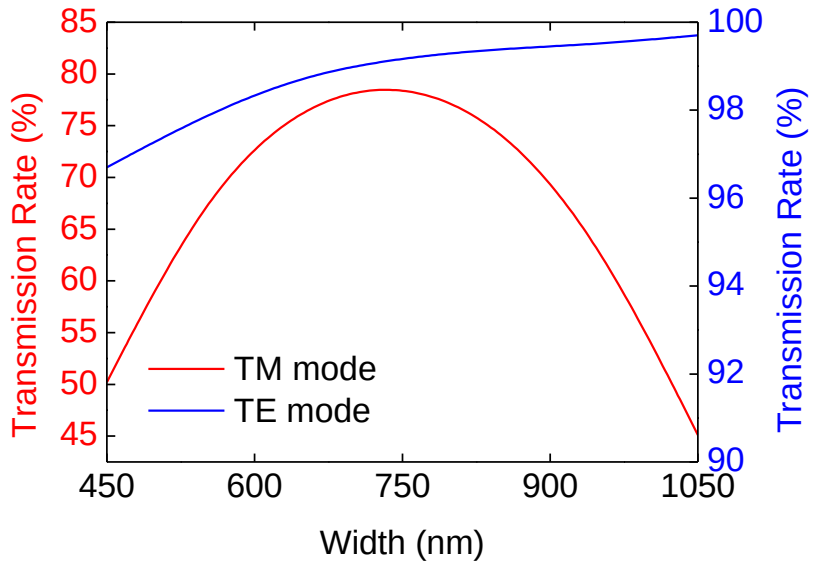

(b)

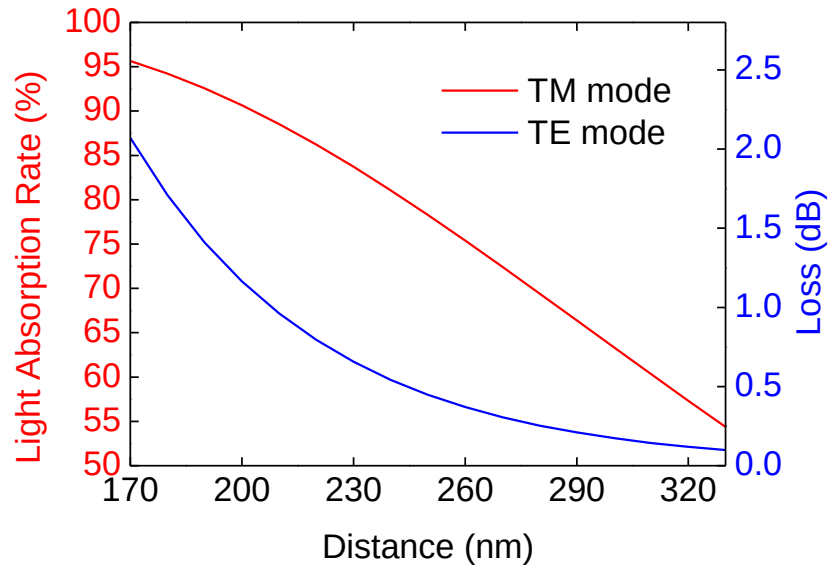

Fig. 4-15 (a) Transmission rate of TM mode in narrow waveguide and of the TE mode in wide waveguide as a function of the width of wide waveguide. (b) Light absorption rate of the TM mode in narrow waveguide and loss of the TE mode in the wide waveguide as a function of the distance between the silicon waveguide and metal

layer of the 10-μm-long TO phase shifter.

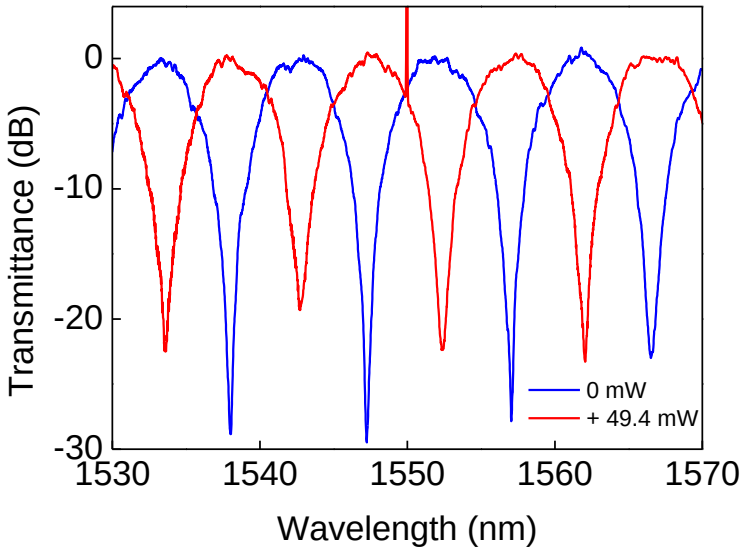

Fig. 4-16 Transmission spectra of the fabricated asymmetric 1×2 MZI-based TO switch using 750-nm-wide waveguide for TE mode and 350-nm-wide waveguide for TM mode when applying a continuous pump control light.

4.3.2 Design of the 1×8 Mach-Zehnder interferometer-based all-optical thermo-optic switch

The on-chip routing design of the waveguides for the 1×8 MZI-based all-optical TO switch should be considered in order to reduce the insertion loss of the device such as propagation loss and the loss of crossing-waveguides. Since the proposed 1×8 MZI-based all-optical TO switch is constructed by cascading the elementary units, 1×2 MZI-based all-optical TO switches, the structure should be designed strictly symmetric for each two output ports of a single 1×2 MZI to avoid loss unbalance between the arms of the 1×8 MZI-based all-optical TO switch. Moreover, the distance between adjacent output ports of the chip was designed to be the same distance, which was 127 μm for our proposed device, in order to couple the light propagating from the fiber array to our device under test correctly. The 3-D structure of the designed 1×8 MZI-based all-optical

TO switch can be seen in Fig. 4-3 in Section 4.2.3.

4.4 Experiments and device characterization

Based on the parameters of the all-optical TO phase shifter described in Section 4.3.2, we will fabricate the 1×2 MZI-based TO switch as well as the 1×8 MZI-based TO switch on SOI platforms. Subsequently, the performances of the fabricated 1×2 MZI-based and 1×8 MZI-based TO switches will be characterized through the measurements.

4.4.1 Fabrication and experimental setup

The proposed switches were fabricated on an SOI wafer comprised of a 220-nm-thick silicon top layer and a 3-μm-thick buried oxide layer (see Appendix A2 for detailed fabrication flows). Firstly, the silicon waveguide was patterned by electron beam lithography (EBL) and reactive ion etching. Subsequently, plasma-enhanced chemical vapor deposition (P-CVD) was used to deposit a 230-nm-thick silicon dioxide layer to determine the absorption of light by the metal layer. Then, photolithography was used to align the positions and generate the patterns of the metal layer, followed by 20-nm-thick Ti layer which was deposited by electron-beam physical vapor deposition. Finally, a 2-μm-thick silicon dioxide over-cladding layer was deposited via P-CVD. Microscopic image of the fabricated 1×2 MZI-based and 1×8 MZI-based TO switches are shown in Fig. 4-17(a) and (c), respectively. Figure 4-17(b) shows more details of the TO phase shifter where two pieces of 7.7-μm-long Ti layers were deposited so as to cover the arms of the MZI as well as the adjacent waveguide for the pump control light propagating. The difference between the length of deposited Ti layer and the designed length of it was due to fabrication error mainly by the photolithography process that generated the patterns of the metal with a relatively low resolution, which can be improved by using EBL in the future.

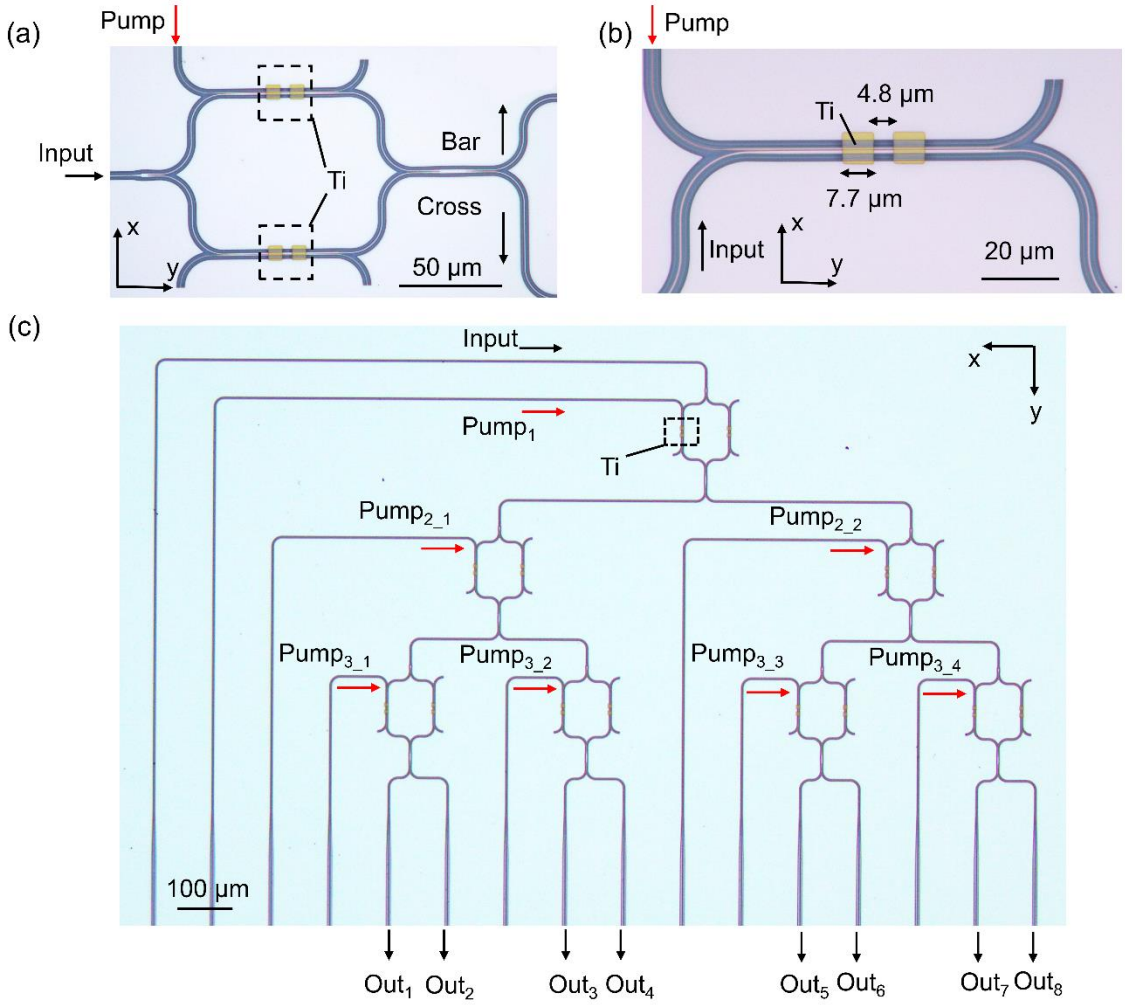

Fig. 4-17 (a) Microscopic image of the fabricated 1×2 MZI-based TO switch. (b) TO phase shifter with Ti layer. (c) Microscopic image of the fabricated 1×8 MZI-based TO switch.

The experimental setup is illustrated in Fig. 4-18. The device under test was measured using a fiber-array measurement system to couple light into multiple waveguides. For the characterization of the 1×2 MZI-based TO switch, an amplified spontaneous emission (ASE) light source (λ = 1530–1565 nm) was used to measure the transmission spectra for static operation. Light emitted from a tunable laser diode (TLD) was used to measure the dynamic characteristics of the device. Light coupled to the input port was polarized into the TE mode using an in-line polarizer or polarization controller (PC). A

continuous-wave (CW) pump control light emitted from the TLD was used for static operation, while it was modulated into a pulse signal by a pulse pattern generator and an electro-optic modulator to measure the dynamic characteristics. After amplification using an erbium-doped fiber amplifier (EDFA), the pump control light was polarized into the TM mode through the PC. During the measurement, we used 1550-nm pump control lights to measure the device because of the limited wavelength range of our tunable lasers and fiber amplifier. However, for future practical applications, the L-band wavelength range (λ = 1565–1625 nm) should be used for pump control lights. The light absorption rate for the L-band compared to 1550 nm is 2.5% higher (from 83.7% to 86.2%), which indicates that the difference of a tuning efficiency is less than 0.001 π/mW.

The input and pump control lights were injected into each input port of the device using a fiber array. The pump light power was monitored using a power meter. The output light from the device was characterized using a spectrum analyzer for static transmittance or a band-pass filter, photodetector, and oscilloscope for the temporal response. For the measurement of the 1×8 MZI-based TO switch, the TE-polarized ASE source was used as the input light, while three sets of different TLDs, EDFAs, and PCs were used to induce three pump control lights (all λ = 1550 nm) to control three stages of cascaded MZIs.

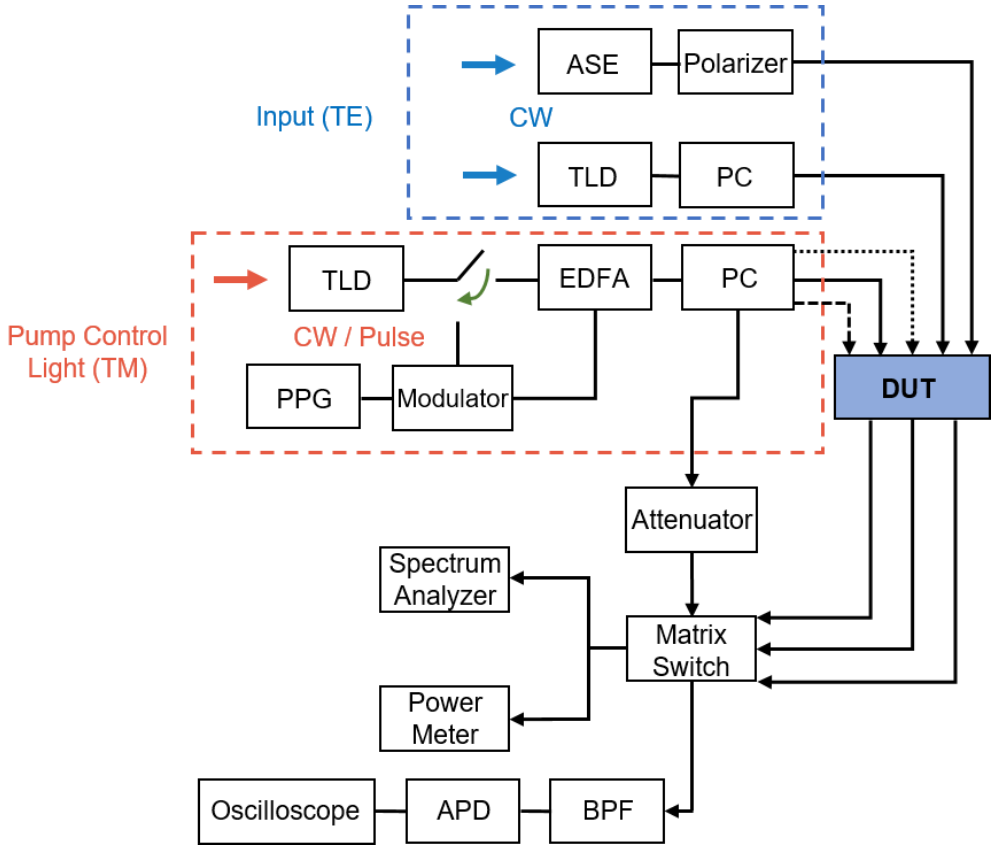

Fig. 4-18 Experimental setup for proposed MZI-based all-optical TO switches. (TLD: tunable laser diode, PPG: pulse pattern generator, EDFA: erbium doped fiber amplifier, PC: polarization controller, CW: continuous wave, DUT: device under test, BPF: band-pass filter, APD: avalanche photodiode)

4.4.2 Characterization of the 1×2 Mach-Zehnder interferometer-based all-optical thermo-optic switch

Figure 4-19(a) shows the transmission spectra of the fabricated symmetric 1×2 MZI-based TO switch. As described in Section 4.2.2, the phase difference between the two arms of the MZI was tuned by the pump control light, resulting in the light power of the output ports. Therefore, the output ports could be switched to on/off states by inducing a pump control light. However, random phase errors due to fabrication imperfection in the waveguides made the initial state not identical for each device (ideally 50:50). The bar port output was in the on state (high transmission) when a 97.4-mW CW pump control

light was induced and in the off state (low transmission) when a 53.6-mW CW pump light was induced. The cross port was switched to the on state with a power of 53.6 mW and off-state power of 97.4 mW. The lowest extinction ratio for the bar and cross ports were measured as 15.4 dB and 15.6 dB in the C-band wavelength range (λ = 1530–1565 nm), respectively. The measured insertion losses at both ports were less than 1 dB. The sharp peak at 1550 nm in the spectra was due to leakage of the high-intensity pump light. By varying applied input pump power, the changes of transmittance of bar/cross port at λ = 1560 nm are shown in Fig. 4-19 (b), indicating a π-phase-shift power P_π of 46.2 mW with an extinction ratio higher than 23.8 dB. P_π was comparable to that for an electrically-controlled silicon-based TO switch [3–5], which were ranging from 0.5 mW to 37.2 mW. Typically, the power consumption and switching speed of the TO switch depend on the thermal conductivity of the waveguide structure, and are tradeoffs.

The temporal response of the switch was characterized as shown in Figs. 4-20(a) and (b) by applying a pump pulse with a width of 4-μs. The maximum optical power intensity was normalized to clearly observe the 10%–90% switching time. As depicted in Figs. 4-20(a) and (b), the 10%–90% rising time and the 90%–10% falling time for the cross port were 1.7 μs and 4.4 μs, respectively, whereas the rising time and falling time for the bar port were 1.6 μs and 8.9 μs, respectively. The applied pulse of the pump control light had a peak power of 53.7 mW, frequency of 25 kHz, and duty cycle of 10%, as shown in Fig. 4-21.

(a)

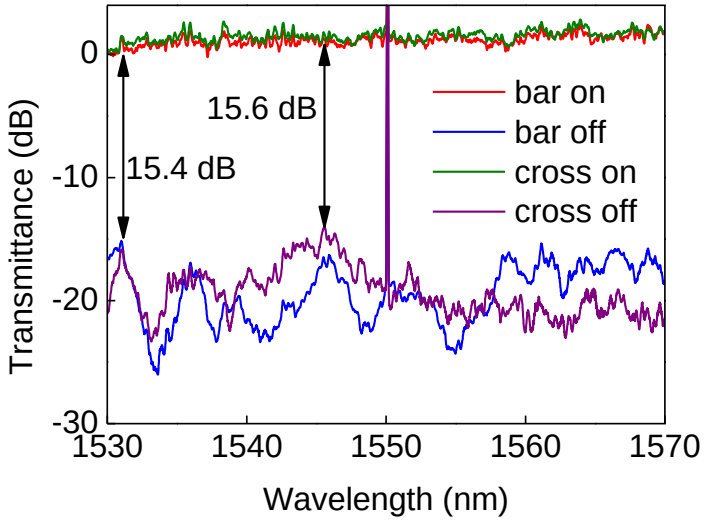

(b)

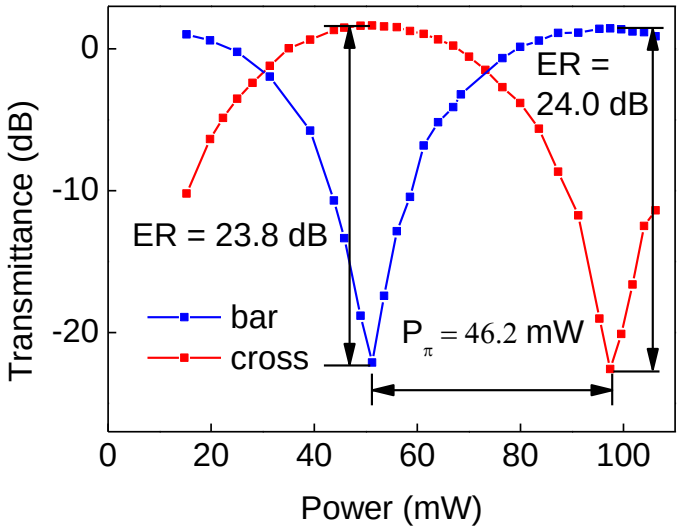

Fig. 4-19 (a) Transmission spectra at the bar/cross port of the fabricated 1×2 MZI-based TO switch applying continuous pump control light (λ = 1550 nm). (b) Transmittance of bar/cross port (λ = 1560 nm) under varying applied pump light power.

(a)

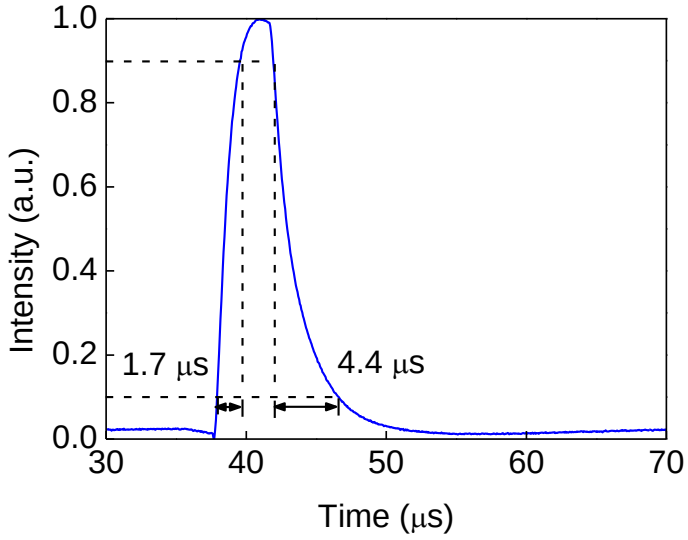

(b)

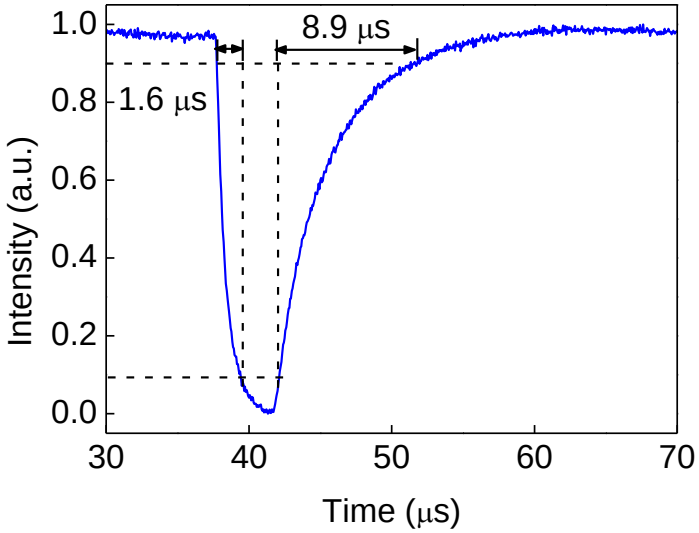

Fig. 4-20 Temporal response of (a) cross port (λ= 1557.9 nm) and (b) bar port (λ = 1561 nm) of the fabricated 1×2 MZI-based TO switch.

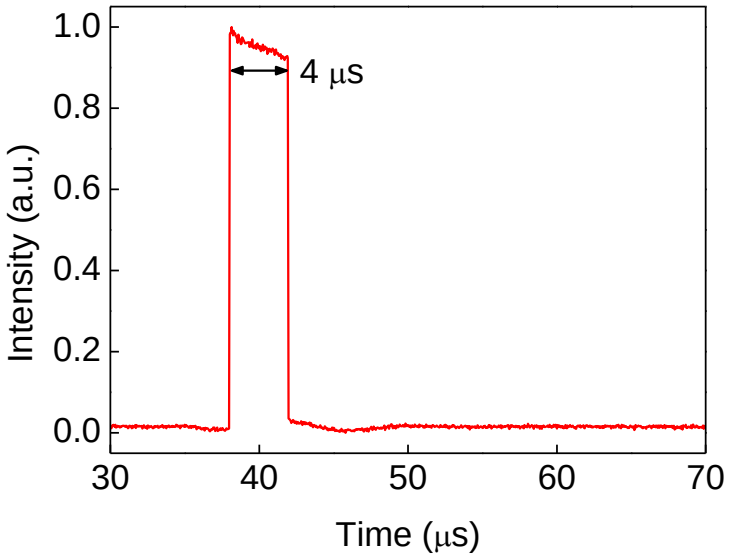

Fig. 4-21 Temporal response of pulse signal pump control light (λ = 1550 nm).

4.4.3 Characterization of the 1×8 Mach-Zehnder interferometer-based all-optical thermo-optic switch

Figure 4-22 shows the measured spectra of the 1×8 MZI-based TO switch for the eight output ports. Figures 4-22(a)–(h) show the on state of one $Out_{i\ (i=1–8)}$ port and off states of the other seven output ports. As described in Section 4.4.1, the input light was polarized into the TE mode, whereas three TM-polarized CW pump control lights with a wavelength of 1550 nm were induced into the three switches of each stage. Although there were 1550-nm peaks due to the leakage of pump light, broadband switching was realized among the C-band wavelength range exhibiting the lowest extinction ratio of 15.2 dB among all output ports and the best case of the lowest extinction ratio of 20.7 dB at Out_7. The minimum insertion loss of this device was measured as 5.0 dB. The insertion loss of each 1×2 MZI-based switch excluding the TO phase shifter with a metal layer above the waveguides was estimated as 0.6 dB, as described in Section 4.3.1.3, including the loss from MMI couplers, tapered waveguides, bending waveguides, etc. As the length of Ti of the fabricated device was 15.4 μm, as shown in Fig. 4-17(b), the absorption loss of the TE-polarized input signal by the metal layer for a 1×2 MZI-based

switch was calculated to be approximately 1.0 dB. The total insertion loss was estimated as 4.8 dB as a single input light propagated through three stages of cascaded 1×2 MZIs to the output ports, which is close to the measurement result. The reason that caused differences in extinction ratio and insertion loss between each output port can be attributed to device fabrication errors.

Table 4-1 lists the injected power of the pump control lights for switching the input light to each output port. The maximum power was 273.5 mW for Out_4 and the minimum power was 124.7 mW for Out_5. The power difference between on and off state of the single 1×2 MZI-based TO switch was calculated to be approximately 46.2 mW, which was the power P_π for the π phase shift. The total power consumption can be comparable with the electrically-controlled silicon-based 1×8 TO switch [6], which exhibited a power consumption of 149.7 mW and 54.7 mW for the switching of each output port as the maximum and minimum values, respectively.

Considering the unused arms of each 1×2 MZI switch, the total power consumption could be reduced when we induced the pump control lights into both arms of the MZI in a push-pull manner, whereas the number of required pump wavelengths was doubled. In a report of Si-based TO switch fabricated by a state-of-the-art technology, the power consumption to trim the initial phase error is approximately 7% of the π phase shift [7]. Therefore, the pump light of one arm was used to trim the initial phase error and compensate for the deviation of environmental temperature change dynamically, while that of the other arm was used to induce the π phase shift for switching. Thus, phase modulation can be implemented more flexibly, resulting in better control of the switching process with a lower optical power.

(a)

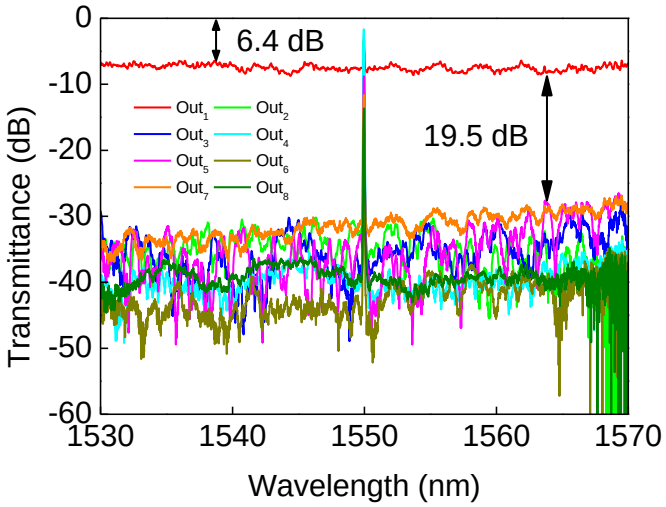
6.4 dB
19.5 dB
Out1 Out2
Out3 Out4
Out5 Out6
Out7 Out8
Transmittance (dB)
Wavelength (nm)
0
-10
-20
-30
-40
-50
-60
1530
1540
1550
1560
1570

(b)

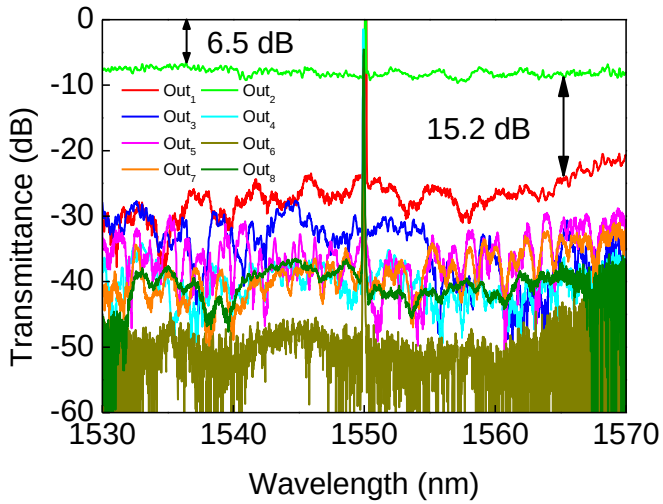
6.5 dB
15.2 dB
Out1 Out2
Out3 Out4
Out5 Out6
Out7 Out8
Transmittance (dB)
Wavelength (nm)
0
-10
-20
-30
-40
-50
-60
1530
1540
1550
1560
1570

(c)

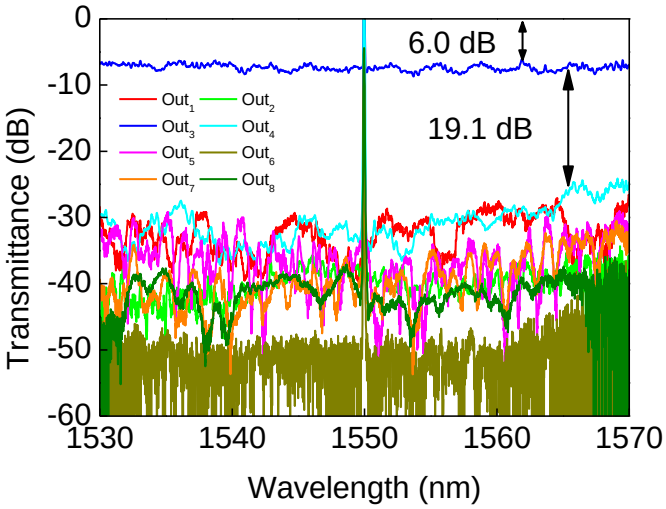
6.0 dB
19.1 dB
Out1 Out2
Out3 Out4
Out5 Out6
Out7 Out8
Transmittance (dB)
Wavelength (nm)
0
-10
-20
-30
-40
-50
-60
1530
1540
1550
1560
1570

(d)

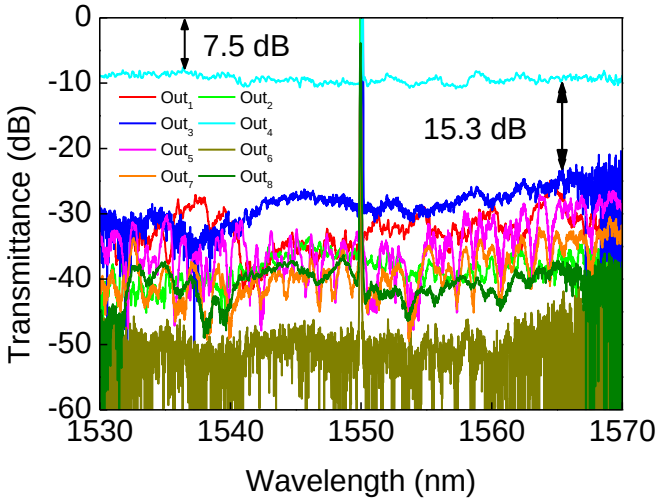
7.5 dB
15.3 dB
Out1 Out2
Out3 Out4
Out5 Out6
Out7 Out8
Transmittance (dB)
Wavelength (nm)
0
-10
-20
-30
-40
-50
-60
1530
1540
1550
1560
1570

(e)

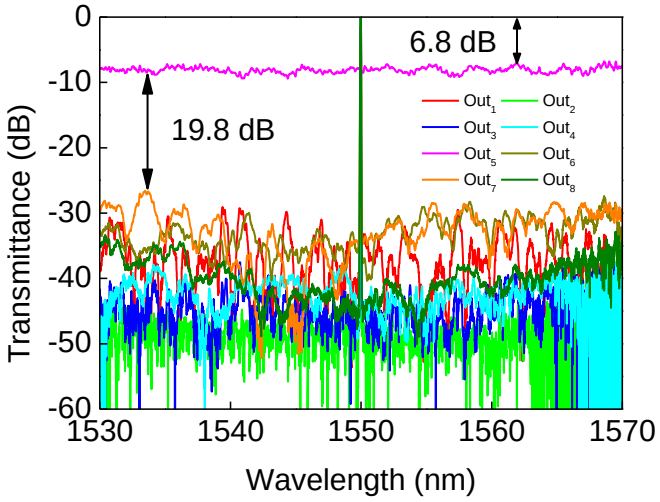
6.8 dB
19.8 dB
Out1 Out2
Out3 Out4
Out5 Out6
Out7 Out8
Transmittance (dB)
Wavelength (nm)
0
-10
-20
-30
-40
-50
-60
1530
1540
1550
1560
1570

(f)

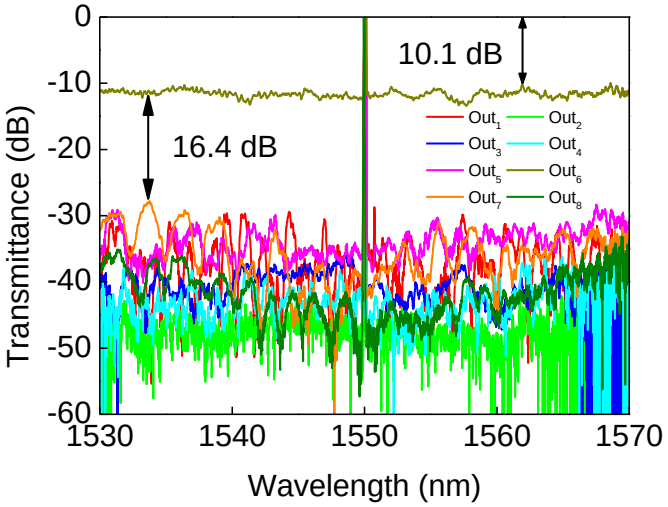
10.1 dB
16.4 dB
Out1 Out2
Out3 Out4
Out5 Out6
Out7 Out8
Transmittance (dB)
Wavelength (nm)
0
-10
-20
-30
-40
-50
-60
1530
1540
1550
1560
1570

(g)

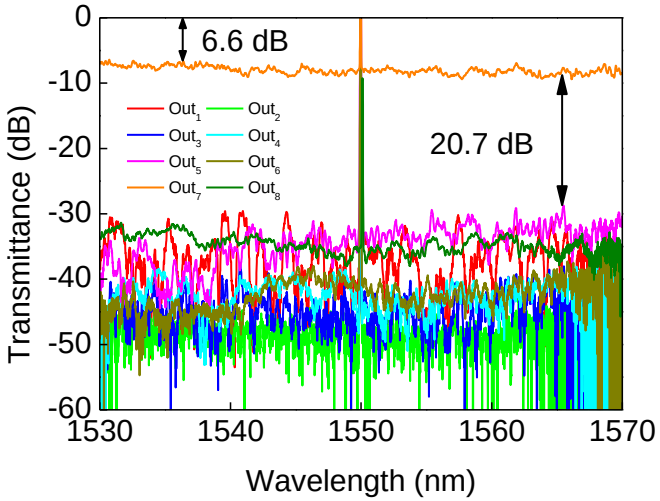

(h)

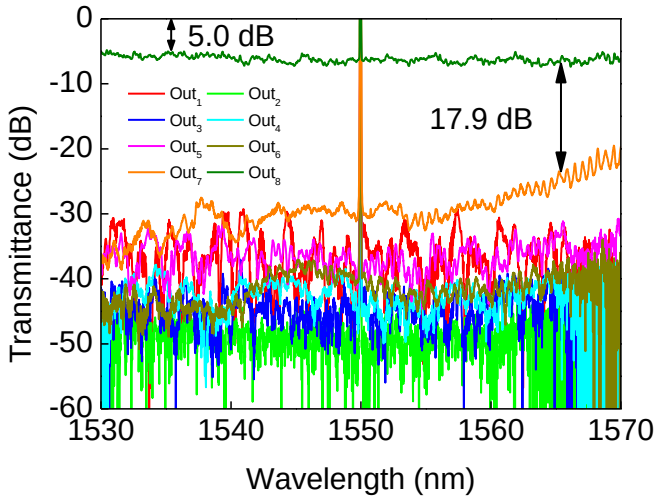

Fig. 4-22 (a) – (h) Transmission spectra of the fabricated 1×8 MZI-based TO switch with the on-state output port at (a) Out_1, (b) Out_2, (c) Out_3, (d) Out_4, (e) Out_5, (f) Out_6, (g) Out_7, (h) Out_8.

Table 4-1. Injected power (mW) for switching to each output port.

	$Pump_1$	$Pump_{2\_1}$	$Pump_{2\_2}$	$Pump_{3\_1}$	$Pump_{3\_2}$	$Pump_{3\_3}$	$Pump_{3\_4}$	Total
Out_1	106.2	31.3	0	25.1	0	0	0	162.6
Out_2	106.2	31.3	0	76.5	0	0	0	214
Out_3	106.2	80.0	0	0	39.2	0	0	225.4
Out_4	106.2	80.0	0	0	87.3	0	0	273.5

Out_5	58.6	0	43.8	0	0	22.3	0	124.7
Out_6	58.6	0	43.8	0	0	76.5	0	178.9
Out_7	58.6	0	91.3	0	0	0	49.4	199.3
Out_8	58.6	0	91.3	0	0	0	97.4	247.3

4.5 Discussion

For the insertion loss of our proposed device, as described in Section 4.3.1, it is mainly due to the insertion loss of the MZI structure as well as the absorption loss by the metal layer. From the fabricated device, the absorption loss by the metal layer of a single 1×2 MZI-based TO switch was calculated to be approximately 1.0 dB while the insertion loss of the MZI structure in a single 1×2 MZI-based TO switch can be estimated to be approximately 0.6 dB through simulation utilizing Lumerical MODE solutions. As analyzed in Section 4.3.1.3, there is a trade-off relationship between the absorption loss by the metal layer and the power consumption of the device, which is mainly caused by the parameter of distance between silicon waveguides and metal layer. We can estimate the π-phase-shift power P_π of a 1×2 MZI-based TO switch when changing this distance based on simulation and experiment results, as shown in Fig. 4-23. The experimental result for P_π of the proposed device was 46.2 mW and it reveals that the estimated P_π is 56.0 mW at a distance around 260 nm, corresponding to an estimated absorption loss of 0.55 dB by the metal layer. It is acceptable for the increase of the power consumption while the absorption loss reduces to 0.55 dB. For the insertion loss of the MZI structure, it can be further optimized to be 0.25 dB with better design of the couplers [8]. Therefore, with this discussion, insertion loss of a 1×2 MZI-based TO switch can be expected to be improved to be 0.8 dB which is the target insertion loss for a 1×2 switch described in Section 1.3.4.

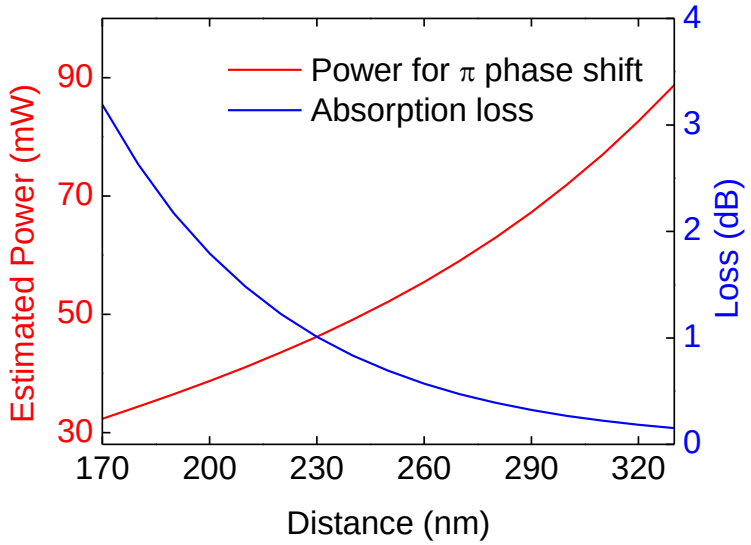

Fig. 4-23 Estimated π-phase-shift power consumption and absorption loss of TE mode signal light by the metal layer as a function of the distance between silicon waveguide and metal layer.

For the switching time of our proposed device, it was measured to be 1.7 μs for 10%–90% rising time and 4.4 μs for 90%–10% falling time, owing to the better design of the pattern of metal layer, as discussed in Section 2.4.3. This switching time satisfied the demand for prospective performance of less than 10 μs using in the next generation passive optical network 2 (NG-PON2) as well as the remotely controllable TDM-PON discussed in this study.

For the extinction ratio of our proposed device, the proposed 1×8 MZI-based all-optical TO switch exhibited a worst extinction ratio of 15.2 dB among all output ports (channels), which is much higher than the reported extinction ratio of 10 dB used in 10G Ethernet PON system [9]. Therefore, we can further design the device with lower insertion loss or lower power consumption to achieve a target extinction ratio of larger than 10 dB. In addition, power consumption can be reduced by sacrificing response speed using thermally isolation structure. Note that, as the worst extinction ratio of two nearest output ports was 15.2 dB, for instance, by cascading two stages of 1×2 MZIs (output ports = 4), the theoretical extinction ratio of two farthest output ports can be calculated

to be 30.4 dB, etc.

4.6 Summary

In this chapter, we proposed and experimentally demonstrated a remotely controllable 1×8 MZI-based all-optical TO switch on the silicon platform, exhibiting a lowest extinction ratio of 15.2 dB across the C-band wavelength region for all output ports, while the measured minimum insertion loss was 5.0 dB. The elementary unit of this device, a 1×2 MZI-based all-optical TO switch, yielded a π-phase-shift power P_π of 46.2 mW with switching times of 1.7 μs and 4.4 μs for 10%–90% rising time and 90%–10% falling time, respectively. By comparing our proposed device to conventional electrically controlled TO switches, the increase of the power consumption of several tens of mW is acceptable for applying in fiber-optic communication network systems. The proposed device will contribute to the establishment of all-optical remote control of signal processing in remotely controllable time division multiplexing passive optical network systems in the future.

References

1. B. Chen et al., “Hitless Wavelength-Selective Switch Using a Single Microring Resonator Assisted With a Symmetric MZI,” in IEEE Photonics Technology Letters 32(7), 402-405 (2020).
2. X. Qiang, X. Zhou, J. Wang, et al., “Large-scale silicon quantum photonics implementing arbitrary two-qubit processing,” Nature Photon 12, 534–539 (2018).
3. D. Celo, D.J. Goodwill, J. Jiang, P. Dumais, M. Li, E. Bernier, “Thermo-optic silicon photonics with low power and extreme resilience to over-drive,” in 2016 IEEE Optical Interconnects Conference (OI). IEEE (2016).
4. M. Jacques, A. Samani, E. El-Fiky, D. Patel, Z. Xing, and D. V. Plant, “Optimization of thermo-optic phase-shifter design and mitigation of thermal crosstalk on the SOI platform,” Opt. Express 27, 10456-10471 (2019).
5. S. -H. Kim et al., “High-Performance Silicon MMI Switch Based on Thermo-Optic Control of Interference Modes,” in IEEE Photonics Technology Letters, vol. 30 (16), 1427-1430 (2018).
6. J. X. B. Sia et al., “1 × N (N = 2, 8) Silicon Selector Switch for Prospective Technologies at the 2 μm Waveband,” in IEEE Photonics Technology Letters 32(18), pp. 1127-1130 (2020).
7. K. Suzuki, R. Konoike, J. Hasegawa, et al., “Low-Insertion-Loss and Power-Efficient 32 × 32 Silicon Photonics Switch With Extremely High-Δ Silica PLC Connector,” J. Lightwave Technol. 37, 116-122 (2019).
8. L. Chen and Y.-K. Chen, “Compact, low-loss and low-power 8×8 broadband silicon optical switch,” Opt. Express 20, 18977-18985 (2012).
9. F. Daido, T. Inoue, Y. Kawanishi, K. Yamazaki, A. Yoshimura, S. Shiba, S. Kouyama, “Development of asymmetric 10G-EPON system,” SEI Technical Review 69 (2009).

Chapter 5

Conclusion

5.1 Conclusion

Optical switches have great potential in telecommunications networks, data center networks, and interconnect applications for multi-process high-performance computing. [1–3] Our idea of a novel remotely controllable time division multiplexing passive optical network (TDM-PON) system utilizing our proposed all-optical thermo-optic (TO) switch is a prospective candidate for future fiber-optic communication network systems. In this remotely controllable TDM-PON system, efficient dynamic burst switching process can be realized by remote control from the base-station without any power supply or digital-to-analog converters in the fields that conventional electrically controlled TO switches needed. Furthermore, bit rate in this proposed system can be expected to increase over tenfold compared to conventional TDM-PON system.

In Chapter 1, we introduced the appearance and development of photonics integrated circuits (PICs) at the beginning and analyzed the advantages of silicon photonics. After the discussion about motivations of all-optical TO switch, we then described the idea and prospective performance of a remotely controllable TDM-PON system for its application as mentioned above. The objective of this research was determined to propose and demonstrate a high-performance remotely controllable all-optical TO switch that can be applied in the proposed remotely controllable TDM-PON system.

In Chapter 2, staring from introducing the basic theory of TO effect on a silicon-on-insulator (SOI) platform by calculating the properties of a conventional TO phase shifter, we discussed in detail the principle of TO effect induced by the metal heater and inferred

that TO effect dominated the change of refractive index of silicon waveguide rather than non-linear effects when a high-intensity pump light was induced. We then simulated the thermal responses of all-optical TO phase shifters with a Ti layer above the structures of a single silicon waveguide as well as two adjacent silicon waveguides. Preparing for the design of our proposed all-optical TO switch, we also analyzed the parameters about the metal layer.

In Chapter 3, optimization of extinction ratio (ER) for the MRR-based all-optical switch compared to previous research [4] was made by designing the microring resonator (MRR) for TE-mode-polarized signal light while the induced pump light was in TM-mode polarization. The proposed device performed at 10–90 % switching times of 0.71 μs for the rising time and 2.66 μs for the falling time in the temporal response measurement. Moreover, it performed an on/off switching ratio of 7.3 dB at the through port and 7.2 dB at the drop port, with a peak pump power of 16.8 mW in the burst switching measurement. Therefore, the effective all-optical switching process has been confirmed utilizing a TM-mode-polarized pump light to control the TE-mode-polarized signal light.

In Chapter 4, our next step was to design and demonstrate the Mach-Zehnder interferometer (MZI)-based all-optical TO switch for broadband switching that could be applied in the remotely controllable TDM-PON system. By comparing different types of design for all-optical TO phase shifter in the MZI structure, the parameters of the design were determined which were used for fabricating all-optical TO switches on SOI wafers. Consequently, as the results of experimentally characterization of the fabricated device by measurement, we proposed and demonstrated the remotely controllable 1×8 MZI-based all-optical TO switch on a silicon platform, exhibiting a lowest extinction ratio of 15.2 dB among the C-band wavelength range (λ = 1530–1565 nm) for all output ports, while the measured minimum insertion loss was 5.0 dB. The elementary unit of this device, a 1×2 MZI-based all-optical TO switch, yielded a π-phase-shift power P_π of 46.2 mW with switching times of 1.7 μs and 4.4 μs for 10%–90% rising time and 90%–10% falling time, respectively. Discussion has been made of the performance comparison between our proposed device and the prospective performance of the remotely

controllable TDM-PON system.

For the performances of proposed device in this dissertation, we summarized them in a table in the following, as shown in Table 5-1. It should be noted that though port count of the MRR-based all-optical TO switch was 1×1 as shown in this table, we can use both of through and drop port for the device based on add-drop MRR, and if we want to expand this port count, multiple microrings with the waveguides for drop ports should be coupled to a same bus waveguide for through port. The fact that MRR-based all-optical TO switch exhibited a better tuning efficiency than MZI-based all-optical TO switches correspond to the simulation results described in Section 2.3 that all-optical TO phase shifter with a single waveguide performed a better simulated tuning efficiency than the TO phase shifter with two adjacent waveguides. Tuning efficiency of 1×8 MZI-based TO switch was close to the one of 1×2 MZI-based TO switch through measurements while switching time of 1×8 MZI-based TO switch can be inferred from the one of 1×2 MZI-based TO switch. Burst switching process utilizing the 1×8 switch should take the delay due to switching time into consideration while adjusting the pump control lights. ER as shown in the table for MRR structure referred to the worst ER of the MRR-based switch during burst-switching measurement, on the other hand, ERs referred to the worst extinction ratio of the broadband switching characterization of 1×2/1×8 MZI-based TO switches among C-band wavelength range for MZI structures. Insertion loss shown in the table can be reduced by optimizing the design of the switches.

Table 5-1. Summary of the device performances.

Structure	**Port count**	**Tuning efficiency**	**Switching time (rise/fall)**	**Extinction ratio**	**Insertion loss**
MRR	1×1	0.0276 $\pi \cdot mW^{-1}$	0.71/2.66 μs	7.2 dB	~2.5 dB
MZI	1×2	0.0216 $\pi \cdot mW^{-1}$	1.7/4.4 μs	15.4 dB	~1 dB
MZI	1×8	~0.0216 $\pi \cdot mW^{-1}$	~1.7/4.4 μs	15.2 dB	5.0 dB

5.2 Perspective

For future development of our proposed device, we will discuss our perspectives towards the design of the all-optical TO phase shifter as well as future works inspired by the proposed all-optical TO switches in the following.

There is a crucial difference between conventional electrically controlled TO switches and our proposed all-optical TO switches, which is that the absorption loss of the input signal by the heater (which is metal in our proposed device) is not negligible for our proposed device while this loss can be negligible for conventional device. Therefore, it is hard to use the structures such as folded and multi-pass waveguides [5, 6] to reduce the power consumption. As discussed in Section 4.3, a trade-off relationship between power consumption and insertion loss of the all-optical TO switch reveals a limitation of using the Ti metal heater for the design of type-B all-optical phase shifter. Based on the high optical absorption and effective thermal resistance of Ti [7], we have investigated the metal heater composed of a Ti layer and an Au thin film, as shown in Fig. 5-1(a), and simulated light absorption rate of TM mode in a 350-nm-wide waveguide and the absorption loss of TE mode in an adjacent waveguide with a width of 750 nm. The gap between the adjacent waveguides was assumed to be 200 nm, which was also the parameters designed for all-optical TO phase shifter described in Section 4.3.1.3. The length of the metal heater was assumed to be 10 μm which the distance between silicon waveguide and the metal heater was set to be 330 nm. Simulation of the light absorption rate of TM mode light and absorption loss of TE mode light was performed by varying the thickness of Au thin film which was supposed to be deposited onto the 20-nm-thick Ti layer, as shown in Fig. 5-1(b), from which we can observe a strong absorption of TM mode in the 350-nm-wide waveguide when the thickness of Au thin film was around 10 nm while the absorption loss of TE mode in the 750-nm-wide waveguide was extremely low compared to the loss of our proposed device. However, as we fabricated the device with this metal heater composed of a 20-nm-thick Ti layer and a 10-nm-thick Au thin film that was deposited above silicon waveguide with a distance of 330 nm between them, the fabricated device exhibited a low insertion loss which was close to simulation result but suffered from a high power consumption (P_π around 71 mW) compared to our proposed device, which can be inferred that either the light-induced heat could not be

conducted to silicon waveguide efficiently or our simulation method did not calculate the light absorption rate of TM mode for this metal heater with a mesh setting of 0.002 μm correctly. Further investigation can be made for the metal heater with this structure in the future.

(a)

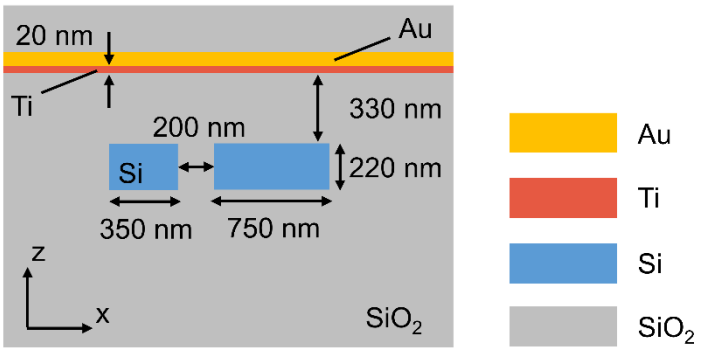

(b)

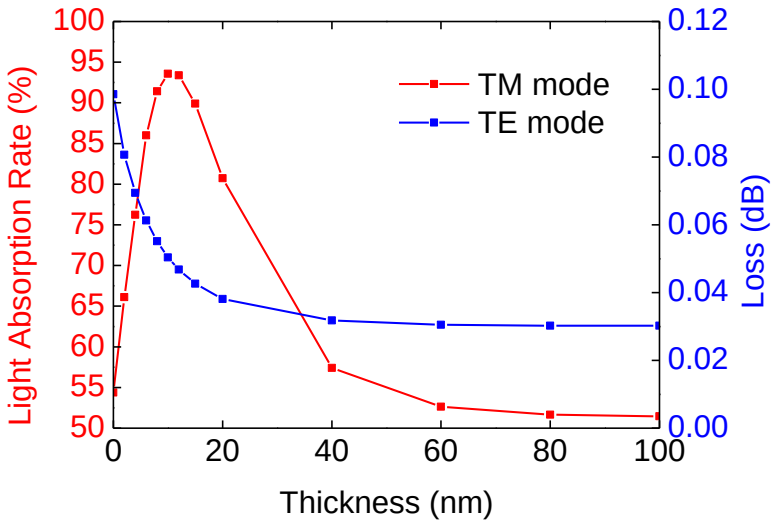

Fig. 5-1 (a) Cross section of all-optical TO phase shifter with a metal heater composed of a 20-nm-thick Ti layer and an Au thin film (b) Light absorption rate of the TM mode in 350-nm-wide waveguide and loss of the TE mode in 750-nm-wide waveguide as a function of the thickness of an Au thin film deposited onto a 20-nm-thick Ti layer.

For the proposed MRR-based all-optical TO switch, it can be used for all-optical signal processing with a relatively low power consumption compared to MZI-based TO switch. However, it is necessary to expand the port count of such device by designing multiple microrings coupled to a same bus waveguide with particular resonant wavelengths according to the demands of the optical communication system so that outputs from drop ports of the MRRs can be used to realize 1×N (N = 2, 3, 4…) switching process.

For the proposed MZI-based all-optical TO switch, its port count also needs to be scaled up to be applied in the remotely controllable TDM-PON system. As discussed in Section 4.5, by optimizing the MZI structure and reducing the absorption loss by the metal layer, an optimized 1×2 MZI-based all-optical TO switch can be expected to exhibit an insertion loss of approximately 0.75 dB. By cascading the 1×2 MZI-based TO switches with this insertion loss, a 1×32 MZI-based all-optical TO switch with a total insertion loss of approximately 3.75 dB can be expected, which can enhance the bit rate of the optical communication to more than tenfold. However, it should be noted that the π phase shift power P_π for an optimized 1×2 MZI-based switch is estimated to be 59.0 mW. On the other hand, utilizing the tuning schematic by pump control lights of two arms of an MZI structure, as shown in Fig. 5-2, it not only shows the advantage in remote trimming of the initial random phase error of the device due to fabrication error [8], but also can be applied to multiply-add data processing for high-performance computing [9, 10].

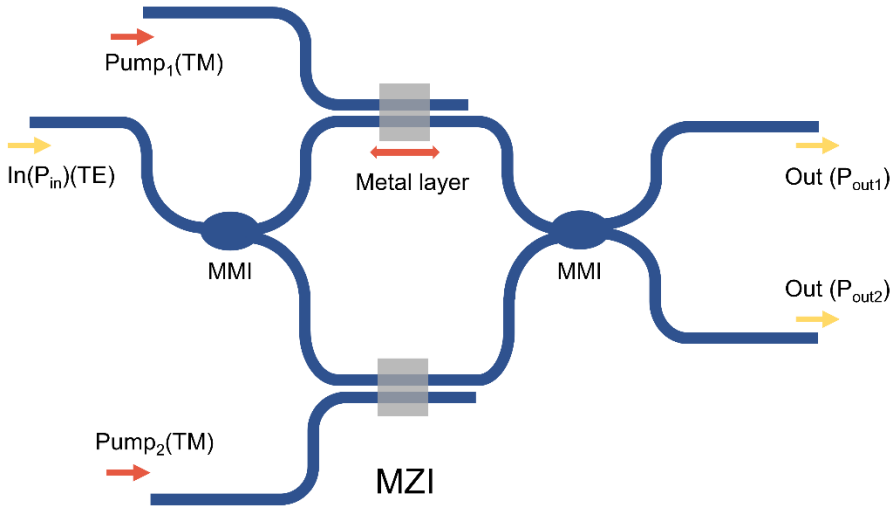

Fig. 5-2 Schematic diagram of a 1×2 MZI-based all-optical TO switch utilizing two arms for pump control lights input.

References

1. E. B. Basch, R. Egorov, S. Gringeri, S. Elby, “Architectural tradeoffs for reconfigurable dense wavelength-division multiplexing systems,” IEEE J. Sel. Top. Quantum Electron. 12, 615–626 (2006).
2. R. Jensen, A. Lord, N. Parsons, “Colourless, directionless, contentionless ROADM architecture using low-loss optical matrix switches,” Proceedings of the 2010 European Conference on Optical Communication in Turino, Italy. 19–23 (2010).
3. P.D. Colbourne, B. Collings, “ROADM Switching Technologies,” Proceedings of the 2011 Optical Fiber Communications Conference in Los Angeles, CA, USA. 6–10 (2011).
4. Y. Kondo, T. Murai, Y. Shoji, et al., “All-Optical Switch by Light-to-Heat Conversion in Metal Deposited Si Ring Resonator,” IEEE Photonics Technology Letters 32(13), 807-810 (2020).
5. H. Qiu, Y. Liu, C. Luan, D. Kong, X. Guan, Y. Ding, and H. Hu, “Energy-efficient thermo-optic silicon phase shifter with well-balanced overall performance,” Opt. Lett. 45, 4806-4809 (2020).
6. S. A. Miller, Y.-C. Chang, et al., “Large-scale optical phased array using a low-power multi-pass silicon photonic platform,” Optica 7, 3-6 (2020).
7. J. Shim et al., “TiOx/Ti/TiOx Tri-Layer Film-Based Waveguide Bolometric Detector for On-Chip Si Photonic Sensor,” in IEEE Transactions on Electron Devices 69 (4), 2151-2158 (2022).
8. K. Suzuki, R. Konoike, J. Hasegawa, et al., “Low-Insertion-Loss and Power-Efficient 32 × 32 Silicon Photonics Switch With Extremely High-Δ Silica PLC Connector,” J. Lightwave Technol. 37, 116-122 (2019).
9. M. Miscuglio, A. Mehrabian, Z. Hu, S. I. Azzam, J. George, A. V. Kildishev, M. Pelton, and V. J. Sorger, “All-optical nonlinear activation function for photonic neural networks [Invited],” Opt. Mater. Express 8, 3851-3863 (2018).
10. F. Shokraneh, S. Geoffroy-Gagnon, M. S. Nezami and O. Liboiron-Ladouceur, “A Single Layer Neural Network Implemented by a 4×4 MZI-Based Optical Processor,” in IEEE Photonics Journal 11 (6), 1-12 (2019).

Appendix

A.1 Important parameters in optical communication systems

(1) Important parameters in optical communication systems

Optical communication systems have been developing since 1990s, there are lots of parameters related to them. Here, we introduce several important parameters usually used for different modulation formats in optical communication systems, as summarized in the following Table A1-1.

Table A1-1. Important parameters in optical communication systems.

Parameter	Unit	Symbol
Average energy per symbol	J	E_s
Average energy per bit	J	E_b
Symbol rate	symbol/s or Baud	R_s
Bit rate	bps or b/s	R_b
Symbol duration time	sec	T_s
Bit duration time	sec	T_b
Noise spectral density	W/Hz	N_0
Signal average power per symbol	W or dBm	P_s
Noise average power per symbol	W or dBm	N_s
Signal average power per bit	W or dBm	P_b
Noise average power per bit	W or dBm	N_b
Signal-to-noise ratio per symbol	- or dB	SNR_s
Signal-to-noise ratio per bit	- or dB	SNR_b or SNR
Bit rate error	-	BER

For an M-order modulation signal, the relation among symbol or bit rate and duration time can be written as

$$R_s = \frac{1}{T_s}, \tag{A1.1}$$

and

$$R_b = KR_s = \frac{1}{T_b}, \tag{A1.2}$$

where $K = log_2 M$ is the number of bits per symbol, e.g., in an on-off keying modulation or in a binary phase shift keying (BPSK) modulation, we have $M = 2$ and $K = 1$.

For the on-off keying modulation, which is also called the amplitude shift keying modulation, average energy per bit can be expressed as

$$E_b = P_b \cdot T_b = \frac{P_b}{R_b}. \tag{A1.3}$$

Therefore, we can derive that

$$P_b = E_b \cdot R_b . \tag{A1.4}$$

Signal to noise ratio (SNR) means the ratio between the power of signal to the power of noise signal in a wave. The SNR for a symbol or a bit can be written as

$$SNR_s = \frac{P_s}{N_s} = \frac{E_s \cdot R_s}{N_0 \cdot R_s} = \frac{E_s}{N_0}, \tag{A1.5}$$

and

$$SNR = SNR_b = \frac{E_b}{N_0}. \tag{A1.6}$$

SNR is often expressed in logarithmic scale (dB) for optical communication systems.

(2) Calculation of bit error rate for on-off keying modulation

The bit error rate (BER) is the number of bit errors per unit time. The BER for on-off keying modulation and direct detection in optical communication systems can be calculated utilizing additive white Gaussian noise (AWGN) channel model that follows the Gaussian probability distribution function

$$f(x) = \frac{1}{\sqrt{2\pi}\sigma} e^{-\frac{(x-\mu)^2}{2\sigma^2}}, \tag{A1.7}$$

which can be also expressed as $X \sim N(\mu, \sigma^2)$.

Assuming that there are two transmitted waveforms corrupted by noise representing

amplitude of binary digits 0 and 1 following $N(s_0, \sigma_0^2)$ and $N(s_1, \sigma_1^2)$, respectively, as shown in Fig. A1-1, the bit error probability can be expressed as

$$BER = p(s_0)P(s > s_{th}|s_0) + p(s_1)P(s < s_{th}|s_1)\,, \tag{A1.8}$$

where $p(s_0)$ and $p(s_1)$ refer to the probabilities of s_0 and s_1, respectively. Also $P(s > s_{th}|s_0)$ refers to the likelihood of a bit misinterpretation for s_1 to be s_0 under the optical threshold of decision s_{th} and $P(s < s_{th}|s_1)$ refers to the likelihood of a bit misinterpretation for s_0 to be s_1 under the optical threshold of decision s_{th}. Assuming that s_0 and s_1 are equally probable, i.e., $p(s_0) = p(s_1) = \frac{1}{2}$, Eq. (A1.8) can be written as

$$BER = \frac{1}{2}\int_{s_{th}}^{\infty} \frac{1}{\sqrt{2\pi}\sigma_0} e^{-\frac{(s-s_0)^2}{2\sigma_0^2}} ds + \frac{1}{2}\int_{-\infty}^{s_{th}} \frac{1}{\sqrt{2\pi}\sigma_1} e^{-\frac{(s-s_1)^2}{2\sigma_1^2}} ds\,, \tag{A1.9}$$

which can be simplified to

$$BER = \frac{1}{2\sqrt{2\pi}}\left(\int_{\frac{s_{th}-s_0}{\sigma_0}}^{\infty} e^{-\frac{z^2}{2}} dz + \int_{\frac{s_1-s_{th}}{\sigma_1}}^{\infty} e^{-\frac{z^2}{2}} dz\right). \tag{A1.10}$$

Assuming $Q = \frac{s_{th}-s_0}{\sigma_0} = \frac{s_1-s_{th}}{\sigma_1}$, which indicates that BER reaches the minimum point when the optical threshold of decision s_{th} is at the cross position of two transmitted waveforms, Q can be also expressed as

$$Q = \frac{s_1 - s_0}{\sigma_0 + \sigma_1}. \tag{A1.11}$$

Using Eqs. (A1.10) and (A1.11), we have

$$BER = \frac{1}{\sqrt{2\pi}}\int_{Q}^{\infty} e^{-\frac{z^2}{2}} dz = \frac{1}{2} erfc\left(\frac{Q}{\sqrt{2}}\right), \tag{A1.12}$$

where

$$erfc(x) = \frac{2}{\sqrt{\pi}}\int_{x}^{\infty} e^{-t^2}\, dt\,, (x \geq 0)\,, \tag{A1.13}$$

represents the complementary error function.

Knowing that the noise has a bilateral spectral density $\frac{N_0}{2}$, $N(s_0, \sigma_0^2)$ satisfies $N\left(0, \frac{N_0}{2T_b}\right)$ and $N(s_1, \sigma_1^2)$ satisfies $N\left(\sqrt{\frac{2E_b}{T_b}}, \frac{N_0}{2T_b}\right)$. Here, the relation $E_b = \frac{1}{2}A^2T_b$ is used where A refers to the waveform amplitude for on-off keying modulation. Taking the

relations mentioned above into consideration, Eq. (A1.12) can be rewritten as

$$BER = \frac{1}{2}\, erfc\left(\sqrt{\frac{E_b}{2N_0}}\right). \tag{A1.14}$$

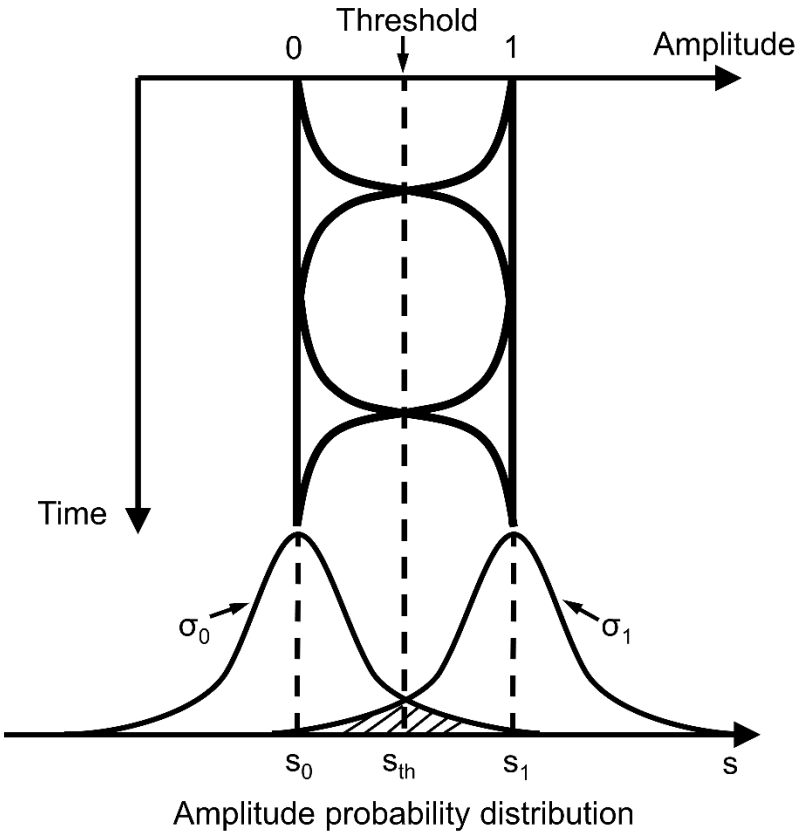

Fig. A1-1 Amplitude probability distribution for intensity modulation/direct detection in optical communication systems.

Therefore, from Eqs. (A1.6) and (A1.14) we can derive the relationship between BER and SNR for on-off keying modulation, which can be expressed as

$$BER = \frac{1}{2}\, erfc\left(\sqrt{\frac{SNR}{2}}\right). \tag{A1.15}$$

A.2 Device fabrication process

(1) SOI substrate preparation

An SOI wafer (Si 220 nm, SiO_2 3 μm thickness) is prepared and diced into $1.5cm \times 1.5cm$ substrates by blade dicing saw, which then need organic cleaning using the conditions below:

Table A2-1.1. Chip clean

	Parameter	Value
Acetone	80 ℃	5 min
Ultrasonic Cleaning	100 kHz	5 min
Acetone	80 ℃	5 min
Ultrasonic Cleaning	100 kHz	5 min
2-Propanol	Room temperature	1 min

After the cleaning, the protective silica mask is removed by the steps as follows:

Table A2-1.2. Wet etching

	Parameter	Value
HF	1:19	~2 min (until the acid fades away)
Rinse	Distilled water	~15 sec × 2

(2) SiO_2 mask deposition

An SiO_2 mask layer of the thickness 200 nm used for etching is deposited on top of the substrate by plasma enhanced chemical vapor deposition (PE-CVD), whose deposition rate may differ each time and it is recommended to measure the rate every time before using PE-CVD, under the conditions:

Table A2-2. SiO_2 mask deposition

Parameter	Value
TEOS	3 $sccm$
O_2	233 $sccm$
Temperature	280 ℃
Pressure	30 pa
RF-power	70 W
Time	~ 4 min

(3) Cleaning

Then the substrate is cleaned with the conditions:

Table A2-3. Chip clean

	Parameter	Value
Acetone	80 ℃	5 min
Ultrasonic Cleaning	100 kHz	5 min
Acetone	80 ℃	5 min
Ultrasonic Cleaning	100 kHz	5 min
2-Propanol	Room temperature	1 min

(4) Photoresist coating

Before using the electron-beam lithography, the photoresist (ZEP-520A) is required to coated on the substrate under the conditions:

Table A2-4. Photoresist coating

	Parameter	Value
Spin-coating	300 rpm	3 sec
	6000 rpm	120 sec
	Slope	3 sec
Pre-baking	180 ℃	15 min

(5) Electron-beam lithography (EBL) and development

Electron-beam lithography is done to generate the waveguide pattern using JEOL JBX-6300UA, following with the development using ZED-N50 as below:

Table A2-5. EBL & development condition

	Parameter	Value
EBL	Acceleration voltage	50 kV
	Current	100 pA
	Exposure amount	130 $\mu C/cm^2$
Development	ZED-N50	Strictly 1 min
	2-Propanol	30 sec

(6) Reactive-ion etching (RIE)

Next procedure dry etching is performed by RIE (Anelva DEM-201). Firstly, SiO_2

layer is etched with CF_4 ion etching as the following conditions:

Table A2-6.1. SiO_2 etching

Parameter	Value
Gas	CF_4
Flow rate	20 $sccm$
RF power	10 W
Pressure	~ 3.5×10^{-3} $Torr$ (Full open)
Time	24 min

Then, that resist on the surface is removed by O_2 cleaning.

Table A2-6.2. O_2 cleaning

Parameter	Value
Gas	O_2
Flow rate	20 $sccm$
RF power	20 W
Pressure	5×10^{-2} $Torr$
Time	3 min

And finally, the Si layer is etched by SF_6 using the pattern that SiO_2 has been etched.

Table A2-6.3. Si etching

Parameter	Value
Gas	SF_6
Flow rate	3.5 $sccm$
RF power	20 W
Pressure	2×10^{-3} $Torr$
Time	5 min

(7) Wet etching

Wet etching is performed to remove the remaining resist and SiO_2 layer using the following conditions:

Table A2-7. Chip clean & wet etching

	Parameter	Value
N,N-Dimethylacetamide	80 ℃	5 min

Acetone	80 ℃	5 min
2-Propanol	Room temperature	30 sec
HF	1:19	~2 min (until the acid fades away)
Rinse	Distilled water	~15 sec × 2

(8) Deposition of SiO_2 using PE-CVD

Next is to deposit the silica cladding between Si waveguide and the metal layer, which uses the following conditions that need to measure the deposition rate every time:

Table A2-8. SiO_2 cladding deposition

Parameter	Value
TEOS	3 $sccm$
O_2	233 $sccm$
Temperature	280 ℃
Pressure	30 pa
RF-power	70 W
Thickness	170 nm (~3.5 min) / 230 nm (~5 min)

(9) Photoresist coating

Before using the electron-beam lithography, the photoresist (AZ-5218) is required to coated on the substrate under the conditions:

Table A2-9. Photoresist Coating

	Parameter	Value
Dehydration bake	200 ℃	90 sec
HMDS prime	1000 rpm	3 sec
	5000 rpm	30 sec
	Slope	3 sec
AZ-5218 spin-coating	1000 rpm	3 sec
	5000 rpm	60 sec
	Slope	3 sec
Pre-baking	100 ℃	90 sec

(10) Maskless lithography and development

The procedure of maskless lithography is done by the equipment MX-1204, following

with the development using AZ-300MIF as below:

Table A2-10. Lithography & development condition

	Parameter	Value
Maskless	Exposure	15 mJ/cm^2
Post exposure baking	120 ℃	120 sec
Maskless aligner	Flood exposure	250 mJ/cm^2
Development	AZ-300MIF	80 sec
Rinse	Distilled water	10 sec

(11) Electron-beam physical vapor deposition

E-gun is used to do the electron-beam physical vapor deposition, during which the Ti metal layer is deposited under the conditions:

Table A2-11. Electron-beam physical vapor deposition

Material	Parameter	Value
Titanium	Gas pressure	$\sim 10^{-4}\ pa$
	Deposit rate	$\sim 1.4\ Å/sec$
	Thickness	20 nm

(12) Lift-off

The metal deposited on the resist is removed by the following steps given below:

Table A2-12. Lift-off

	Parameter	Value
N,N-Dimethylacetamide	80 ℃	5 min (until resist totally lifts-off)
Acetone	80 ℃	5 min
2-Propanol	Room temperature	20 sec

(13) Deposition of SiO_2 over cladding

An SiO_2 over cladding is deposited under the conditions:

Table A2-13. SiO_2 overcladding deposition

Parameter	Value
TEOS	3 $sccm$
O_2	300 $sccm$

Temperature	280 ℃
Pressure	30 pa
RF-power	70 W
Thickness	2 μm (~ 40 min)

Finally, the substrate is diced using the blade dicing saw appropriately prior to measurement.

Acknowledgement

First and foremost, I would like to extend my deepest gratitude to Prof. Yuya Shoji for his thoughtful advice and support to my research and campus's life in these five years' study in Japan from master's course to doctoral course. His serious scientific attitude, rigorous academic spirit, and work style of striving for excellence have deeply infected and inspired me.

Next, I'm also grateful to all the teachers and professors I met throughout the study in Tokyo Institute of Technology and especially thank Prof. Nobuhiko Nishiyama, Prof. Hiroyuki Uenohara, Prof. Shigeru Nakagawa and Prof. Tomohiro Amemiya from Tokyo Tech and Prof. Tomohiro Kita from Waseda University for their precious time to review and evaluate my doctoral dissertation. I would also like to thank Prof. Tetsuya Mizumoto and Prof. Kensuke Ogawa from Mizumoto & Shoji laboratory.

I would like to especially appreciate for the help from Mr. Yuichiro Kondo, Mr. Ranepura Hewage Neranjith, Mr. Shuyuan Liu and Mr. Yisheng Ni who supported me throughout my research and shared their knowledge of simulations and experiments.

Then, I would like to take the opportunity to sincerely thank all my present and past colleagues of Mizumoto & Shoji laboratory as well as Shoji laboratory, Mr. Yuichiro Kondo, Mr. Ranepura Hewage Neranjith, Mr. Serrano Nunez Mario Alberto, Mr. Toshiya Murai, Mr. Yukinobu Nakajima, Mr. Shuyuan Liu, Mr. Daiki Minemura, Mr. Ryota Yokoi, Mr. Kosuke Itagaki, Mr. Daiki Kano, Mr. Satoshi Tanimoto, Ms. Yui Hattori, Mr. Keita Miura, Mr. Keisuke Miura, Mr. Satoshi Morishita, Ms. Wen-Hsien Su, Mr. Shunya Takematsu, Mr. Yuki Hara, Mr. Shun Yajima, Mr. Yuto Tange, Mr. Yisheng Ni, Mr. Shohei Taniguchi, Mr. Huan Tong, Mr. Hiroki Arai, Mr. Kotaro Sato, Mr. Nguyen Thanh Binh, Mr. Wataru Yoshida, Mr. Naoaki Tsuchiya, Mr. Keita Chihara, Mr. Yuki Shimotsu, Ms. Fujita, Mr. Kosuke Murakami, Mr. Yusuke Hara, Mr. Genkei Tei, Mr. Kento Hiura,

Mr. Yasuhiro Tsuda, Mr. Shinya Tagawa, Mr. Kosuke Nakanishi, Mr. Gaku Takagi, Mr. Yuto Shinbo and Mr. Jianping Wang for their support during my research.

I would like to acknowledge Institute of Innovative Research (IIR), Tokyo Institute of Technology for their support during my doctoral course.

Lastly, I can’t help expressing my gratitude to my parents, my family and my friends who support my lives and provide the encouragement during my five years’ study.

Thank you very much for reading.

List of publication

Journal Papers

1. **Z. Liang**, S. Liu and Y. Shoji, "Improvement of extinction in optically-controlled silicon thermo-optic switch based on micro-ring resonator with distinct probe signal," *Jpn. J. Appl. Phys.* 62, 032001 (2023).
2. **Z. Liang** and Y. Shoji, "All-optical remotely controllable 1×8 silicon thermo-optic switch based on Mach-Zehnder interferometers," (accepted).

Oral Presentation

1. **Z. Liang** and Y. Shoji, "Remotely Controllable All-Optical MZI-based Thermo-Optic Switch," *2023 IEEE Photonics Conference (IPC). IEEE,* (2023).

Poster Presentations

1. **Z. Liang** and Y. Shoji, "Silicon based all-optical micro-ring resonator thermo-optic switch," *International Symposium on Photonics and Electronics Convergence (ISPEC),* (2022.12).
2. **Z. Liang** and Y. Shoji, "Silicon-Based All-Optical Mach-Zehnder Interferometer Thermo-Optic Switch," *International Symposium on Photonics and Electronics Convergence (ISPEC),* (2023.11).